Microstructural evolution of AISI304 stainless steel in the Steckel Mill rolling process

A thesis submitted to the faculty of engineering and the Built Environment, University of Cape Town, in fulfilment of the requirements for the degree Master of Science in Engineering

By
Sa-aadat Parker
Centre for Materials Engineering
2004

Abstract

The microstructural evolution of AISI304 stainless steel in the Steckel mill rolling process is investigated. This study includes the analysis of mill logs, microstructural examination of the mill product, deformation simulations and post deformation heat treatments.

The mill logs from industry contains information about various process variables such as temperature, roll speed, dimensions of the mill strip and forces applied to it during the hot mill rolling process. The strain, strain rates and stresses on the mill strip can be calculated from the mill logs. An understanding of the metallurgical changes during rolling process can be gained by analysing the mean flow stress trends that evolve during rolling.

Microstructural examination of the strip in different regions allows us to evaluate the property variations in the strip. This was done with microhardness testing, conventional optical microscopy and electron backscatter diffraction. The middle section of the strip demonstrated full recrystallization whereas the head and tail sections demonstrated no signs of recrystallization. The property differences through thickness proved to be negligible.

Laboratory simulation was done in uniaxial compression testing on a Cam Plastometer. It was found that the temperature has a profound influence on the flow stress and the microstructure. The strain rates experienced in hot rolling does not have a significant effect on the flow stress and no measurable effect on the hardness.

Heat treatments were done on the deformed uniaxial compression samples. The results of these heat treatments were analysed by two different methods: to deform the sample again after the heat treatment and to compare the yield stress from the first and second deformation and to measure the changes in room temperature hardness with the heat treatment time. The latter led to the development of a time to 50% recrystallization equation that allows the prediction of a direct annealing time for complete softening at the conclusion of the hot rolling process.

Acknowledgements

My first thanks goes to my supervisor, Professor Rob Knutsen for his patience and guidance.

Then my second set of acknowledgements goes to the friendly people at Metals Technology lab at CANMET especially Dr Elhachmi Essadiqi for his hospitality and warmth and for making the testing possible. The rest who must be thanked are Dr Don Barager for discussion on the materials testing; Dave Dolan for the testing of the materials; Claude Marchand for his insight on metallography.

I would also like to thank Columbus Stainless, Sean du Toit for providing the testing material, all the mill log data and various other pieces of information.

Various other acknowledgements are to be made:

Miranda Waldron at the Electron Microscopy unit for help with the scanning electron microscope.

Wayne Sheldon at Bohler Steel for the use of the salt baths to do the annealing treatments.

Norma Africa at the Centre for Materials Engineering for her administrative excellence.

Penny Park-Ross also of the Centre for Materials Engineering for good cheer and help around the lab.

Glen Newins at the Mechanical Engineering workshop for the excellent machining of the specimens.

Lastly but certainly not least I would like to thank my parents for their support and understanding.

Table of Contents

CHAPTER 1: INTRODUCTION

The hot rolling of metals and alloys is the most common form of deformation used in industry. Various process parameters govern the material properties, namely temperature, strain and strain rate. Other important considerations are related to the material state and composition.

AISI304 stainless steel is one the most commonly produced grades of stainless steel. Its commercial importance makes it an object of intense study and a large body of literature exists on its properties under hot deformation conditions. Often different studies will have numerically dissimilar outputs for nominally the same composition alloy. These inconsistencies are due to a range of factors including small changes in the chemical composition and the types of deformation simulations that are used in these studies.

As the properties of the material are evolve through the hot rolling process, various microstructural phenomena affect the mechanical properties of the metal. These include recrystallization (RX), recovery and strain hardening. These phenomena provide the link between the process parameters and the end properties. Particularly important is the process of recrystallization. In AISI304 stainless steel, it is the principal softening mechanism.

The objectives of this project are to map out the microstructural evolution during the hot mill rolling process and its relation to process parameters: the mechanisms that are occurring and to what extent. Specific objectives are to:

1. Analyse property variations in the metal strip through thickness and in the head and tail sections in relation to the middle section.

2. Recommend a practice for direct annealing of the material, which requires complete softening at the end of the hot rolling schedule.

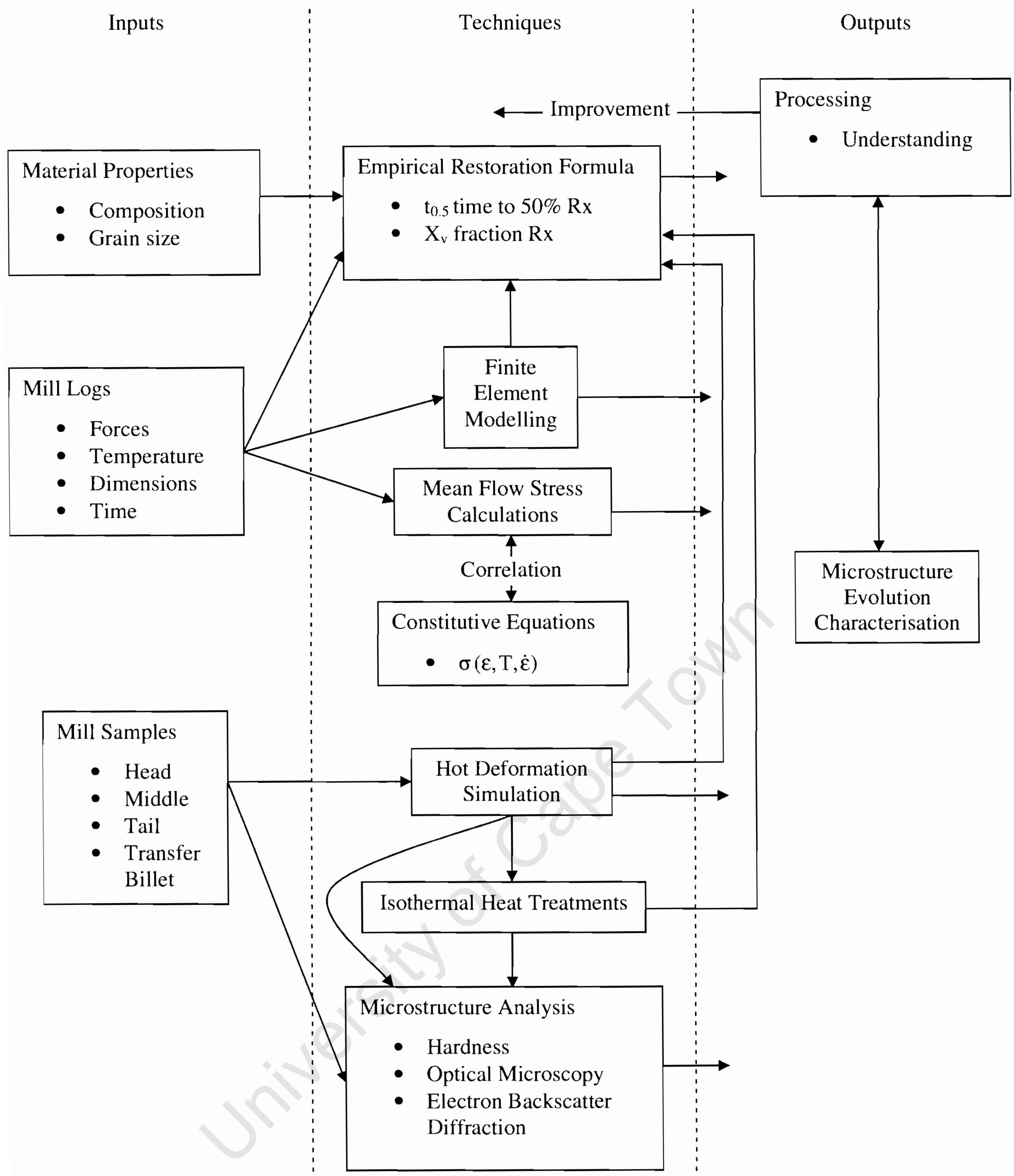

Figure 1-1: Diagrammatic representation of characterising the microstructural evolution.

The experimental procedure in trying to fulfil these objectives is presented in Figure 1-1.

The inputs are data and physical samples that were received from the mill process. These are the material properties refer to the composition and grain size and the information from the mill logs and are the process conditions under which the material was deformed.

The techniques shown are the experimental methods used to analyse the inputs. Hot deformation testing was done on the transfer billet. The testing parameters are based on the mill log information. Isothermal heat treatments were performed on selected deformed specimens. These were used to determine empirical restoration formulas. The empirical restoration formulas used were: time to 50% recrystallization ($t_{0.5}$) and the fraction recrystallized (X_{srx}). A finite element model of the strip was used to determine if the variations through thickness were significant. The mean flow stress calculations were performed on the mill log data to establish the microstructural evolution in the mill strip. These were compared to constitutive equations from literature that related steady state flow stress to the process parameters strain (ε), temperature (T) and strain rate ($\dot{\varepsilon}$). Microstructural analysis involves doing microhardness, optical microscopy and electron backscatter diffraction. This analysis was done on the deformed samples from the hot deformation studies, on the products of the isothermal heat treatments and on the mill samples.

CHAPTER 2: LITERATURE REVIEW

2.1 Material

Stainless steels are corrosion resistant iron-based alloys containing a minimum of 11 Wt% chromium and a maximum of 1.2 Wt% carbon. This amount of chromium is the minimum required to form a passivation layer, which prevents the formation of rust, hence the designation 'stainless'.

2.1.1 Properties and Applications

The main commercial advantage of stainless steels is their corrosion resistance given that their mechanical properties may be equalled or surpassed by other steels at a lower initial cost. The mechanical properties of stainless steels can be tailored to meet the end user requirements through small changes in their composition and appropriate thermomechanical processing.

The forming properties of stainless steel are important with the different types of manufacturers requiring different properties. The producers of household sinks require good stretch forming properties whereas saucepan manufacturers need a material that can be deep drawn.

Many types of stainless steels have excellent welding properties; they can be easily welded without significant changes in their corrosion resistance and mechanical properties. Stainless steels also find uses at extreme temperatures where they have excellent high temperature creep resistance and certain grades have excellent toughness properties at cryogenic temperatures[1, 2].

2.1.2 Corrosion Resistance of Stainless Steel

The most commercially important feature of stainless steels is their corrosion resistance. The reason for stainless steel's resistance to corrosion is the chemically inert Cr_2O_3 layer that protects the underlying material. This layer is adherent and forms rapidly in the presence of oxygen. Any substance that damages or reduces this layer will therefore lower the chemical resistance of the steel.

2.1.3 Structure

Stainless steels are classified according to their microstructure which is based on their chemical composition. The major classifications of stainless steel are given in Table 2-1.

Table 2-1: Stainless steel types and common designations[3].

Stainless Steel Type	Crystallographic Structure	Abbreviation	Major Phases
Austenitic	face centred cubic	FCC	γ
Ferritic	body centred cubic	BCC	δ, α
Martensitic	body centre tetragonal	BCT	α'

A major group of stainless steels not mentioned in Table 2-1 is the duplex stainless steels which are a combination of ferritic and austenitic stainless steel. The various alloying elements have an effect on the relative amounts of ferrite, austenite and martensite in the structure and this can be seen in Equation 2-1[3].

$$\%\text{Ferrite} = 3(\text{Cr} + 1.5\text{Si} + \text{Mo}) - 2.8(\text{Ni} + 0.5\text{Mn}) - 84(\text{C} + \text{N}) - 19.8\%$$

Equation 2-1

Equation 2-1 is an empirical equation and is based on the stainless steel at ambient conditions after normal processing. The alloying additions are in weight percent. From this equation, chromium can be seen to be a very strong ferrite-forming element whereas nickel, carbon and nitrogen have the opposite effect and are strong austenite-forming elements. The fraction of ferrite will differ with processing conditions. Its formation is promoted at higher temperatures and strain rates[4].

2.1.4 Austenitic Stainless Steel

Austenitic stainless steels are the most popular class of stainless steel. They contain 18 – 25% Cr and 8 – 20% Ni[5]. The large amounts of Nickel stabilise the γ phase in the material. These stainless steels cannot be hardened by quenching to room temperature, though, but can only be hardened by cold working. A property shared by austenitic and ferritic stainless steels is that they do not undergo major precipitation hardening. Austenitic stainless steels are non-magnetic, unlike their ferritic counterparts, but can become slightly magnetic when deformed. This magnetism can be attributed to the formation of martensite.

2.1.4.1 Transformation to Martensite

For a given composition, transformation to martensite can occur if one of the following two conditions are met: The material is cooled from a high temperature to below the martensite start temperature (M_s) or it is worked at low temperatures. This process is a diffusionless shear transformation process. The empirical equation below shows the effects of various alloying elements on the M_s (°C)[6].

$$M_s = 1302 - 42(Cr\%) - 61(Ni\%) - 33(Mn\%) - 28(Si\%) - 1667(C\% + N\%)$$

Equation 2-2

Even above low M_s (for example -180°C for AISI304 stainless steel), stainless steel may undergo a martensite transformation. This transformation can occur by deformation. The temperature above which no transformation is possible despite any amount of cold work is the M_d temperature. Another equation relating composition and transformation to martensite is given below[3, 7]:

$$M_{d30} = 413 - 13.7(Cr\%) - 9.5(Ni\%) - 8.1(Mn\%) - 9.2(Si\%) - 462(C\% + N\%) - 18.5(Mo\%)$$

Equation 2-3

Where M_{d30} is the temperature at which 50% martensite may be formed by deforming the material by 0.3 strain in tension. This method of deformation shall affects the M_{d30}, with the temperature being different for tension and compression.

The strain induced martensite phase is much harder than the parent austenite phase and it influences the work hardening rate. The chemical composition can therefore be changed to achieve an optimum work hardening rate.

2.1.4.2 Carbide Precipitation

Austenitic stainless steels may contain up to 0.15% C. This carbon can combine with predominantly chromium but also other metals such as iron or molybdenum to produce carbide precipitates of the form $M_{23}C_6$. The carbon first precipitates at high energy sites like grain boundaries followed by twins and then within austenite grains as can be seen in Figure 2-1. The formation of these carbides is undesirable as they deplete the chromium levels in the surrounding area and lead to a phenomenon called sensitisation. The lowering of chromium inhibits the steel's ability to form a passive layer and severely reduces the steel's corrosion resistance. The carbide precipitation may also lead to a slight increase in the strength of the stainless steel.

The reduction of carbon and to a lesser extent the chromium in the sensitised region will elevate the M_s as can be seen in Equation 2-2. The formation of martensite is then promoted in the sensitised region[8].

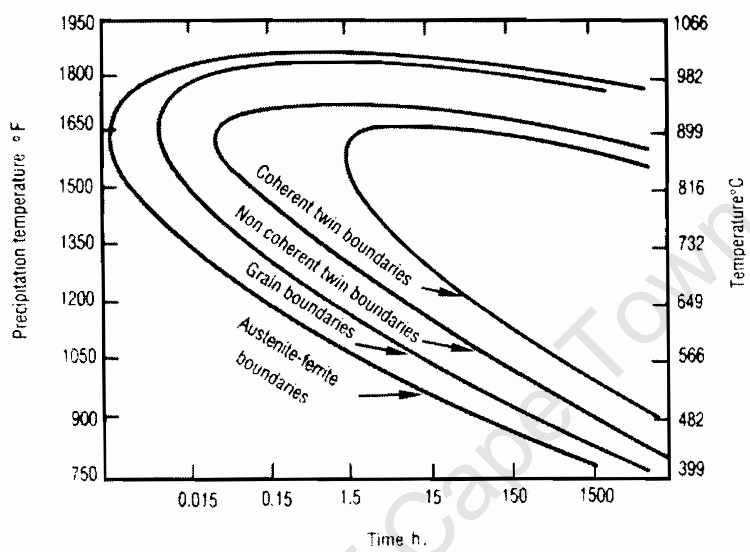

Figure 2-1: A temperature time transformation (TTT) curve of AISI 304 stainless steel showing carbide precipitation kinetics[6].

The TTT curve in Figure 2-1 indicates the effects of temperature and time on the carbide precipitation. Holding the metal for extended periods at high temperatures can induce carbide precipitation. At higher temperatures, the carbides may be dissolved and if the steel is cooled at a sufficiently rapid rate, the carbon may be locked in solution.

2.1.5 Processing

Various different processing routes exist for stainless steel in industry; a summary is given of the common features of these processing routes with particular emphasis on the processing of stainless steel flat product.

The first stage of processing stainless steel is melting of the recycled scrap and virgin material in an electric arc furnace. In the next stage, molten metal is decarburised in an oxidation process. The main method used in industry is the Argon-Oxygen Decarburisation (AOD) method. Oxygen is blown through the molten metal to react with the carbon to form carbon dioxide and carbon monoxide. Argon is also introduced in this operation to reduce the partial pressures of the oxygen and carbon dioxide and causes oxidation of the carbon in preference to the alloying elements of the molten metal. In this fashion, the molten stainless steel is refined and the carbon percentage is reduced from 1.5% to 0.05 %[6].

The refined molten metal is poured into a continuous caster and cooled to form a slab. In producing stainless steel flat product, hot rolling is by far the most popular next stage of processing. The slab from the continuous caster would be typically 200mm thick and heated before the first stage of hot rolling. The hot rolling may be divided into two stages: the roughing stage and the finishing stage. In the roughing stage, the thickness is systematically reduced and the length is increased. The finishing stage involves more reductions in thickness and the surface finish from this stage is very important. Apart from mechanical properties, two important issues which determine the quality of the final product are the thickness gauge tolerance and the surface quality

The finish stage rolling can be done on a hot strip mill with high lot numbers. These consist of a series of tandem mills. Another method, which is the one examined in the present study, is done on a reversing mill. A specialised reversing mill is the Steckel mill which will be described in the following section.

2.1.5.1 Steckel Mill

The feature of the Steckel Mill that distinguishes it from other hot strip reversing mills are the two coiling furnaces on either side of the work rolls and this setup is illustrated in Figure 2-2. The temperature in these hot coil furnaces is usually 1000°C[9].

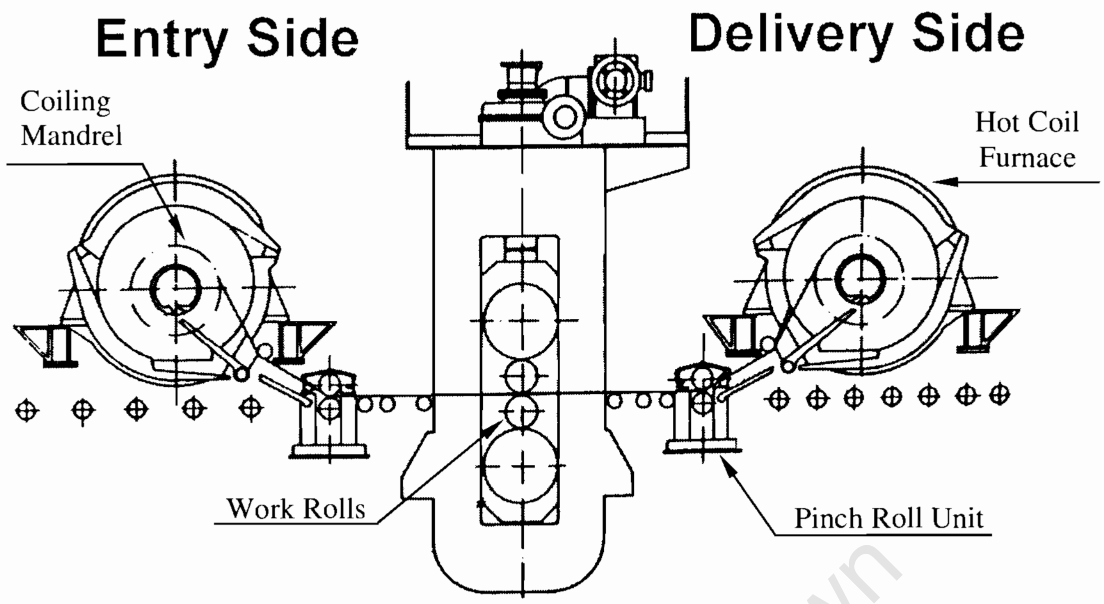

Figure 2-2: Schematic of hot coil furnace[10].

The head section is the end that enters the mill first and the tail section is the end that last enters the mill. The head section of the transfer bar from the roughing mill is cropped. It then passes under the entry side of the coiling furnace and is then threaded into the roll gap between the work rolls by pinch roll unit. This initiates the first pass. After passing through the work rolls the strip[a] is threaded by the pinch roll unit into the hot coil furnace on the delivery side. This is done at approximately 2m.s^{-1} to 2.5m.s^{-1}. The mandrel and the strip then accelerate to the rolling speed. Tension is then established in the strip. The strip then decelerates to stop between the roll gap and the delivery side pinch roll unit. Note that the whole strip does not go into the hot coil furnace. In this position, the roll gap is preset for the next pass. The preset time takes approximately 5 to 7 seconds for 1300mm wide AISI304 stainless steel. This time is as short as possible to conserve heat in the ends. In the next pass the strip is

[a] When the transfer bar enters the Steckel Mill, its name changes and it is called the strip[10, 11].

threaded by the entry side pinch roll unit into the hot coil furnace. The strip goes through this process an odd number of times usually 5, 7 or 9 times. If an even number of passes was done it would pass back the way it came. On the last pass the strip passes through the delivery side pinch roll unit and passes under the delivery side hot coil furnace to the laminar coolers.

2.1.5.2 Steckel Mill Advantages

The Steckel mill is generally used in developing countries and is often referred to as the "Poor man's rolling mill"[6]. This is due to its versatility and comparatively low capital cost. Lot numbers are also usually quite small from a Steckel mill.

Capital costs are lower, since the single stand Steckel mill can perform the task of double stand mill. Furthermore, long runoff tables are not required due to the coil box. Therefore, the Steckel mill provides a short compact construction.

Since the Steckel mill has two hot coil furnaces, the temperature is kept high and the reversing passes can continue indefinitely. A wider range of gauges and widths can be achieved, especially thinner gauges since the material is kept hot. A better surface quality is also achieved than traditional reversing mills[12].

2.2 Deformed State

An understanding of the deformed state is important in understanding the hot rolling process. It also furthers the understanding of recrystallization and related annealing phenomena. The deformation process involves an accumulation of dislocations whereas restoration is a process where dislocations are annihilated. These dislocations provide the driving force for restoration.

2.2.1 Stacking Fault Energy

The stacking fault energy (γ_{SFE}) is important in determining the deformation mode and therefore the end microstructure.

In austenitic stainless steels, the value is related to the thermodynamic stability of the austenite γ_{SFE}. In austenitic stainless steels the γ_{SFE} will vary with the composition and the temperature[13].

In FCC metals with low γ_{SFE} (e.g. austenitic stainless steels), less than $25 \mathrm{mJ.m^{-2}}$, the preferred deformation mode is twinning. Twins are straight sided bands that run across grains. The twins are wider with higher deformation temperatures and lower γ_{SFE}. The twin density also increases with a decrease in γ_{SFE}. Lower stacking fault energy also results in an increase in the work hardening rate[14].

In metals with higher γ_{SFE}, the deformation mechanisms of cross slip and climb are favoured.

2.2.2 Grain Boundaries

Grain boundaries are boundaries that separate areas of different crystallographic orientation. As a distinction that depends on the context, High Angle Grain Boundaries (HAGB) have misorientation angles greater than 10° to 15° and any other boundaries with angles greater than 1° to 1.5° are called Low Angle Grain Boundaries (LAGB)[15].

The concept of a Coincident Site Lattice (CSL) is an important way of describing grain boundaries. When two lattices of adjacent grains interpenetrate then some of the lattice sites will coincide. The reciprocal of ratio of the lattice sites to the coincident lattice sites is denoted Σ. This value of Σ would indicate orientation relationships between adjacent grains. Boundaries with special values of Σ are often referred to as CSL boundaries. A coherent twin boundary is a subset of CSL boundaries with Σ = 3. LAGB have low values of Σ close to 1.

2.2.3 Microstructural Change

During deformation, the microstructure of a metal changes in a number of ways. The grain changes shape and the grain boundary area increases. The grain boundary area increases due to the incorporation of dislocations that are accumulated during deformation. In hot rolling, the grains become lath shaped. In polycrystalline materials, the individual grains change orientation relative to the directions of the applied stresses. The grains then acquire a preferred orientation or texture that becomes stronger as deformation proceeds[16].

Various microstructural features form within grains during deformation.

2.2.4 Substructures

Substructures such as subgrains and cells may form within grains from dislocation rearrangement during deformation. These features form mainly in microstructures that deform by slip. They can be distinguished by the dislocations in their boundaries. Subgrains have sharp well ordered dislocations and cells have a diffuse tangled array of dislocations[15]. In metals with low values of γ_{SFE} (for example AISI 304 stainless steel) a dislocation cell structure does not arise and the dislocations break down to form arrays of stacking faults on twin planes.

2.2.5 Other Misorientation Features

A source of misorientation or orientation gradient can occur near large second phase particles (> $1\mu m$).

Deformation bands are regions of homogenous orientation inside the grains which have different orientations to the rest of the grain.

Transition bands are also sources of in-grain misorientation. They are interfaces that form when grains break up during deformation. They occur after both room temperature and high temperature deformation.

Low γ_{SFE} promotes strong strain hardening which facilitates the formation of shear bands. Shear bands are areas of localised strain and both they and shear bands are sources of high angle misorientation[15].

2.2.6 Stored Energy

The stored energy provides the driving force for restoration. The stored energy originates when working the material; approximately 1% goes into deformation and the remaining 99% of the work is given off as heat. Most of the stored energy is contributed by dislocations. Point defects store very little energy since they have very high mobility. The energy contributed by the dislocations is determined firstly by their density and then by their arrangement and distribution. The surroundings of the dislocations also influence how much energy they store. The energy is highest in a pileup such as a grain boundary and lowest in cell walls and subgrain boundaries.

The amount of stored energy depends on several factors. It is influenced by the deformation type (compression, tensile...), extent of the deformation and the deformation temperature. Further factors include the composition and the grain size of the material.

2.3 Flow Stress

Flow stress is the instantaneous true stress of a material. It is a function of material related parameters (composition, microstructure, strain history and structure) and processing conditions (extent of deformation, deformation temperature, strain rate). A material starts deforming plastically when the applied stress reaches the flow stress. In a compression test, it would be the magnitude of the stress to produce plastic compression under given test conditions.

Flow stress is an important issue in metal working as it determines the working loads. Various metallurgical phenomena can be ascertained by the shape of the flow stress curve. These metallurgical phenomena will be discussed in the following sections.

2.3.1 Zener-Hollomon Parameter

Temperature and strain rate are fundamentally linked processes in the hot working process. Their effects may be explained by considering the softening and strain hardening mechanisms. Any increase in temperature would increase the rate of softening whereas any increase in strain rate would increase the rate of strain hardening. Therefore, any increase in temperature may be compensated for by a decrease in strain rate. Zener-Hollomon parameter (Z) embraces the control variables $\dot{\varepsilon}$ and T in the hot working process[17]:

$$Z = \dot{\varepsilon} \exp\left(\frac{Q_{def}}{R\,T_{def}}\right)$$

Equation 2-4

Where: $\dot{\varepsilon}$ = strain rate (s^{-1})

T_{def} = temperature of deformation (K)

R = gas constant (8.31 $J.mol^{-1}.K^{-1}$)

Q_{def} = activation energy for deformation ($J.mol^{-1}$)

For AISI304 stainless steel the following formula is a rough empirical guide to calculating the activation energy[18]:

$$Q_{def} = 13.5\ (S)\ (\pm 25)\ kJ.mol^{-1}$$

Equation 2-5

Where: S = weight percent of the alloying metal solute

The universal hot working equation is an Arrhenius equation for steady state flow stress and incorporates the Z parameter and is given in Equation 2-6 [19 - 22]:

$$\dot{\varepsilon} \exp\left(\frac{Q_{def}}{R\,T_{def}}\right) = A(\sinh \alpha\sigma)^n$$

Equation 2-6

Where: α = stress multiplier (kPa^{-1})

A = constant (s^{-1})

n = stress exponent

Table 2-2: Constants for AISI 304 stainless as found in published works.

A (s^{-1})	n	α (kPa^{-1})	Q_{def} (kJ/mol)	Ref
5.65×10^{14}	4.6	0.012	393	18
2.8×10^{14}	5.3	0.08	380	23
5×10^{15}	4.7	0.012	434	24
-	4.29	0.012	407	25

From Equation 2-6, the effects of an increase in temperature or a decrease in strain rate can be associated with a decrease in flow stress.

This equation assumes that flow stress is only dependant on the instantaneous values of temperature, strain and strain rate. It is an equation of state and does not depend on history. This equation would not accommodate any prior strain history.

2.4 Recovery

Recovery is the term used to describe all annealing processes in deformed materials where no migration of high angle grain boundaries occurs[26]. It is not a single process but a succession of micromechanical processes including: point defect annihilation; dislocation annihilation and rearrangement; subgrain formation and growth[27, 28]. These processes are thermally activated.

Complete recovery is unlikely to occur in most materials due to the occurrence of recrystallization. Recovery usually involves partial restoration of properties since the dislocation structure is not completely removed.

2.4.1 Recovery Parameters

The occurrence of recovery depends on many parameters namely the material, strain, annealing temperature and deformation temperature.

The stacking fault energy is one of the most important material parameters in recovery. High γ_{SFE} promotes dislocation glide, climb and cross-slip – processes which control the rate of recovery.

An increase in strain and annealing temperature tends to increase the extent of recovery until the onset of recrystallization which then becomes the dominant restoration mechanism.

2.4.2 Dynamic Recovery

Recovery that occurs during deformation at high temperatures is called Dynamic Recovery (DRV) to distinguish it from the static process that occurs after deformation. It occurs at all strains at a large range of temperatures above approximately $0.4T_M$ (Melting temperature in Kelvin)[29].

2.4.3 Nucleation of Recrystallization

If a large orientation gradient exists in a crystal then as subgrains grow during recovery the local misorientation increases. This local instability of the microstructure results in highly misorientated subgrains and grains which are the nuclei for recrystallization.

2.5 Recrystallization

Recrystallization is the formation of a new dislocation free grain structure by the movement and creation of HAGB[30]. It is favoured in materials with low to medium γ_{SFE}[31]. The stacking faults are usually present in planar arrays of high energy which provide a large driving force for recrystallization. Climb, a process that aids recovery is also difficult in materials with low γ_{SFE}.

During processing, complete recrystallization results in complete softening of the metal by replacing deformed grains with strain free grains and prevents the accumulation of stored energy during successive deformations. Hence, working loads are kept to same level.

2.5.1 Nucleation and Growth

The nucleus in the recrystallization may be thought of as a crystallite of low energy which is separate from the deformed matrix into which it is growing by high angle grain boundaries. This nucleus is not a nucleus in the strict thermodynamic sense (such as in phase transformations or precipitation reactions) but tiny regions which pre-exist in the deformed material. For this recrystallization nucleus to arise a critical dislocation density difference has to exist at the interface between the nucleus and the surrounding material. Only a region with a high misorientation angle between itself and the surrounding material has the necessary mobility to evolve into a fully recrystallized grain. Experimental observation reveals that grain boundaries are preferred nucleation sites. In coarse-grained materials transition bands, shear bands and twin boundaries can be sites for nucleation[16]. These regions have high local misorientation, see section 2.2.5.

2.5.2 Kinetics of Recrystallization

The kinetics of recrystallization always shows a sigmoidal shape as can be seen in Figure 2-3. This may be described in terms of the nucleation and growth mechanisms and can be approximated by the JMAK model which is attributed to Kolmogorov, Johnson, Mehl and Avrami. The general form of the Avrami type equation is given in Equation 2-7 [32 - 34].

$$X_{SRX} = 1 - exp\left[-Bt^{k}\right]$$

Equation 2-7

Where: X_{SRX} = volume fraction of statically recrystallized grains

B = constant

t = time (s)

k = Avrami or JMAK exponent

Some of the basic assumptions made in this model are that the nucleation and growth rates are constant with time, the nucleation sites are random throughout the material and the grains grow in an isotropic fashion in three dimensions. There are various problems associated with these assumptions. The growth rate is not constant and is shown to decrease with time. Nucleation sites are situated at grain boundaries, shear bands and transition bands. Sample geometry or some other microstructural constraint may force the grains to grow in one or two dimensions. All these factors would decrease the JMAK exponent which would neither be constant nor an integer.

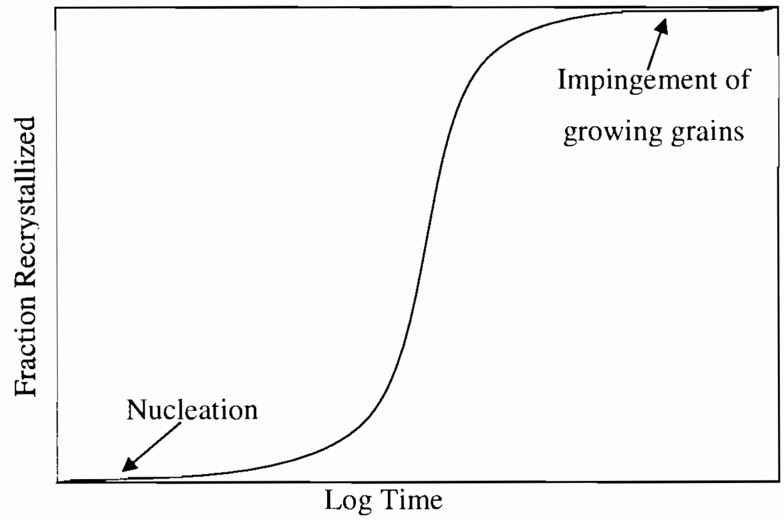

Figure 2-3: Characteristic form of recrystallization curve during isothermal annealing.

2.5.3 Quantifying Recrystallization

When recrystallization is an important factor, calculating the length of time a material takes to soften is an important issue in hot working Equation 2-7 is often modified for calculation purposes as seen in Equation 2-8[35 - 39].

$$X_{SRX} = 1 - \exp\left[(-\ln 2)\left(\frac{t}{t_{0.5}}\right)^k\right]$$

Equation 2-8

Where $t_{0.5}$ is the length of time taken for recrystallization to continue until half complete and in Equation 2-9 we see the factors it depends on:

$$t_{0.5} = A\dot{\varepsilon}^u \varepsilon^v D_o^w Z^x \exp\left[\frac{Q_{srx}}{RT}\right]$$

Equation 2-9

Where: D_o = grain size (μm) before deformation

$\dot{\varepsilon}$ = strain rate (s^{-1}) during deformation

ε = strain after deformation

Q_{srx} = activation energy of static recrystallization ($J.mol^{-1}$)

T = annealing temperature (K)

The other values not given above for Equation 2-9 are constants and are given for AISI304 in Table 2-3.

Table 2-3: Constants for Equation 2-9 for AISI304, determined by various researchers.

A (μm^{-2})	u	v	w	x	Q_{srx} ($kJ.mol^{-1}$)	Q_{def} ($kJ.mol^{-1}$)	k	Ref
-	0	-2	2	-0.375	362	393	1.66	32
2×10^{-10}	-0.81	-1.6	1	0	197	380	1.02	35
-	0	-2	2	-0.375	63	-	1.3	40, 41
-	0	-4	2	-0.375	365	-	0.5 - 1.5	42, 43
3.7×10^{-15}	0	*	2	-0.38	425	410	2	44
6.3×10^{-5}	-0.68	0	0	0	107	280	-	45

*The equation does not have a strain value in this format and the form of the equation is given in Equation 2-10[44].

$$t_x = \frac{AZ^{-0.38}D_o^2 \exp\left(\frac{425000}{RT}\right)}{1 - \exp\left[-1.5\left\{\frac{(\varepsilon - 0.08)}{\varepsilon_p}\right\}^2\right]}$$

Equation 2-10

The peak strain (ε_p) is the strain at which the peak stress occurs. Peak strain is associated with dynamic recrystallization (DRX) see section 2.5.6.1. Use of ε_p does not imply that DRX has occurred, DRX only occurs when the strain reaches 60% to 80% of ε_p. The peak strain can established from the Equation 2-11 below[23]:

$$\varepsilon_p = 3\times10^{-3} D_o^{0.5} Z^{0.09}$$

Equation 2-11

From Table 2-3, there is a range of constants from literature. Note that only one of the exponents of Z or $\dot{\varepsilon}$ will always be zero. The strain rate is already contained in the Z parameter so having both exponents non-zero would be redundant. In equations where the exponent of Z is zero, the deformation temperature and the temperature at which recrystallization is occurring are the same. These equations assume that recrystallization is independent of the activation energy of deformation.

2.5.4 Factors Affecting Recrystallization Rates

Various factors affect the rates of recrystallization. There are many important material and processing parameters that need to be taken into account when considering recrystallization. These are summarised in Equation 2-9 and Equation 2-10.

2.5.4.1 Deformation

The amount and type of deformation can affect the rate of recrystallization. This can be rationalised by noting that the amount of deformation changes the stored energy, which provides the driving force for recrystallization. The number of recrystallization nuclei also increase. A minimum amount of strain is required to initiate recrystallization. This is usually about 0.01 to 0.05 strain[15]. As the amount of strain increases the recrystallization rate increases until a maximum is reached at about 2 to 4 strain.

2.5.4.2 Grain Orientation

In polycrystals, the rate of recrystallization also depends on the initial grain texture and the deformation texture. Different texture components will recrystallize at different rates which can lead to inhomogeneous recrystallization. The strain path history which is related to the initial texture affects the stored energy which may make seemingly identical texture components recrystallize differently[15].

2.5.4.3 Grain Size

A decrease in the initial grain size leads to increases in dislocation density at low strains ($\varepsilon < 0.5$) which then increases the stored energy and increases the recrystallization rate.

As grain size decreases the grain boundary area increases which increases the amount of sites available for recrystallization.

Deformation texture will change as the initial grain size changes which will affect the recrystallization kinetics as detailed in section 2.5.4.2.

2.5.4.4 Annealing Temperature

Annealing temperature has a great influence on the rate of recrystallization since the process is thermally activated. Increasing the annealing temperature will increase the rate of recrystallization.

2.5.4.5 Deformation Conditions

Deformation at high temperatures and low strain rates reduces the stored energy from deformation. Recrystallization occurs less readily when having lower temperatures or higher strain rates.

2.5.5 Microstructure after Recrystallization

An effective way of quantifying the amount recrystallization is by quantitative metallography i.e. examining the microstructure. The various features will be discussed below.

2.5.5.1 Grain Size

The final grain size may be explained by the effects of the various conditions on the balance between nucleation and growth. Any parameter that increases the nucleation rate or the number of nuclei will reduce the size of the final grains. The effects of various factors can be summarised in Equation 2-12 [40] and Equation 2-13 [44].

$$D_{srx} = A'\varepsilon^{-0.75} D_o^{0.5} Z_{DRV}^{-0.1}$$

Equation 2-12

Where: D_{srx} = grain size after recrystallization

Z_{DRV} = same form as Z parameter except activation energy is for Dynamic Recovery (354 $kJ.mol^{-1}$ for AISI304 stainless steel)

A' = constant (value is $71.4\,s^{0.1}\mu m^{0.5}$ for AISI304 stainless steel)

$$D_{SRX} = \frac{BZ^{-0.1}D_o^{0.5}}{1.15 - \exp\left[-2.5\left\{\frac{(\varepsilon - 0.08)}{\varepsilon_p}\right\}\right]}$$

Equation 2-13

Where: B = constant (value is $125\,s^{0.1}\mu m^{0.5}$ for AISI304 stainless steel)

From the equation above it can be seen that an increase in strain or decrease in grain size would increase the nucleation rate. A finer grain size would then result.

2.5.5.2 Grain Shape

In most cases, the shape of recrystallized grains is approximately equiaxed polyhedrons. Although occasionally in FCC metals grains orientated by approximately 40° about a <111> direction to the deformed matrix grow in an isotropic fashion into a pan cake shape.

2.5.5.3 Annealing Twins

In FCC materials of low or medium γ_{SFE} annealing twins may form during recrystallization. These twins are parallel sided lamellae and are shown in Figure 2-4. They form during primary recrystallization, recovery or grain growth following recrystallization.

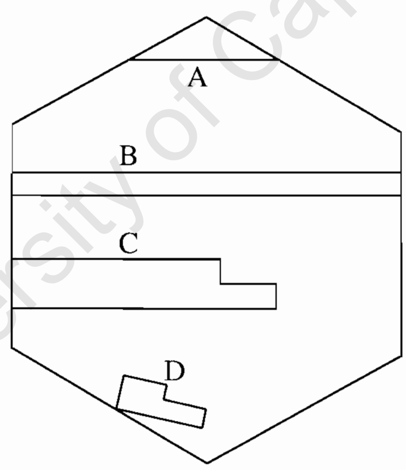

Figure 2-4: Morphologies of various annealing twin morphologies in FCC crystals. Twins are labelled A to D[46].

The mechanism responsible for twin formation is not well understood. Two popular theories for their formation is growth faulting and boundary dissociation. Growth faulting is started (and ended) by a change in the stacking sequence. Boundary dissociation involves the dissociation of HAGB into twin boundaries and some other boundary. The energy is lowered in this process.

The formation of twins is promoted by high to medium level of cold work followed by a short time, high temperature anneal. An example would be 70% cold work followed by a 60 second anneal at 1000°C[47, 48]. A decrease in the stacking fault energy would also increase the proportion of twins.

2.5.6 Dynamic Recrystallization

Recrystallization that occurs during high temperature deformation is called **Dynamic Recrystallization (DRX).** It is an important phenomenon as it increases the ductility of the material and reduces the required working load[49, 50].

2.5.6.1 Onset of Dynamic Recrystallization

When the flow stress is steady state, the energy due to work hardening equals the energy lost by recovery and the stored energy will be less than the critical amount needed for DRX. In this case DRX will not occur. However in materials where recovery is slow DRX occurs at a critical strain (ε_c) which is usually 60% to 80% of peak strain (ε_p), at a range of temperatures above $0.6\,T_M$[35].

2.5.6.2 DRX Evolution

In polycrystalline materials, DRX is preceded by fluctuation in the grain boundary shape. The grain boundaries form serrations and DRX nucleates at prior HAGB. The grains often form in a necklace manner as illustrated in Figure 2-5.

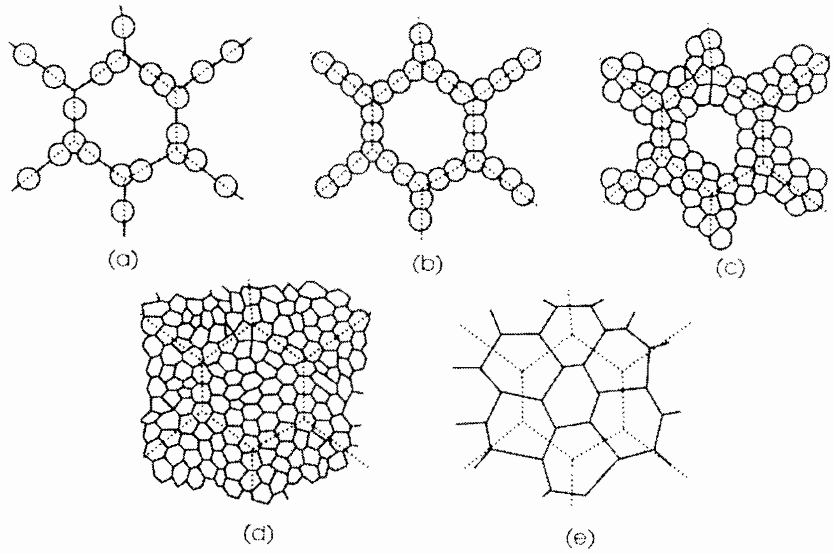

Figure 2-5: Microstructure development during DRX is illustrated. The evolution with a large initial grain size is shown from (a) – (d) and in (e) a small initial grain size is shown[15].

In static recrystallization, there is limited nucleation early in the process and then continuous growth of these nucleated grains until there is impingement on other nucleating grains. Grain size increases as the volume fraction of recrystallized grains increases. In DRX, there is repeated nucleation and limited growth; deformation induces work hardening of the growing grains. As the strain increases, the driving force for grain growth decreases until it reaches a critical level and then ceases. The grain size is unaffected by impingement on other recrystallized grains. This can be seen in Figure 2-6.

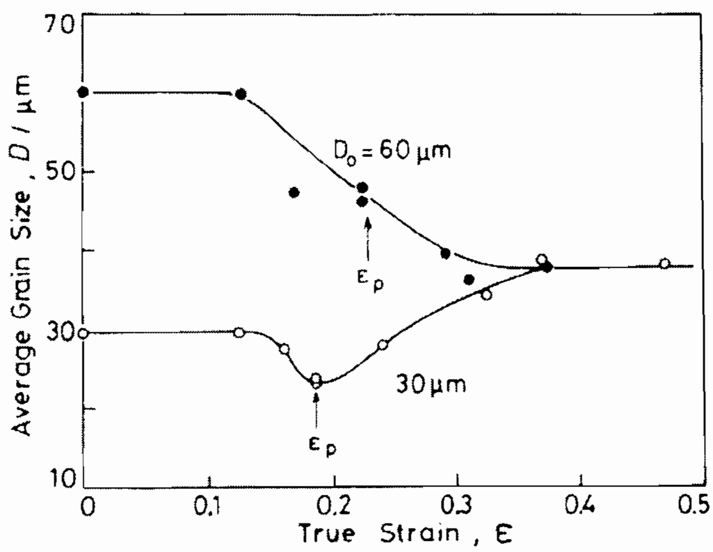

Figure 2-6: DRX grain size development as a function of strain in Nickel, deformed in tension at a strain rate of 0.003s^{-1} and temperature of 923K[51].

The grain size is mainly determined by the deformation conditions. It depends quite sensitively on strain and strain rate. The insensitivity to strain after steady state can be seen from Figure 2-6. This is embodied in the following equation[52, 53]:

$$\sigma_{ss} = KD_{ss}^{-n}$$

Equation 2-14

Where: σ_{ss} = steady state flow stress (MPa)

D_{ss} = grain size during steady state (µm)

K = positive constant

n = exponent usually between 1 and 0.

If full DRX has occurred then the grains are generally equiaxed. Grain boundaries are curved and serrated. Twin boundaries can form which would be curved[33, 54].

2.5.6.3 Metadynamic Recrystallization

If only partial DRX has occurred then the microstructure would be very heterogeneous. Three different regions can result: small, dislocation-free DRX grains; large DRX grains with moderate dislocation density; grains not recrystallized with high dislocation density. During post-deformation annealing each region would restore in a different fashion. The dislocation-free grains may grow by postdynamic or metadynamic recrystallization (MRX). This MRX is a static event. It differs from conventional SRX in that it nucleates from the nuclei formed during DRX. The large DRX grains may exhibit metadynamic recovery or if the dislocation density is sufficiently high it may undergo SRX. The grains not recrystallized may undergo SRV followed by SRX.

2.5.6.4 Flow Stress during Dynamic Processes

The dynamic processes referred to are dynamic recovery (DRV) and dynamic recrystallization (DRX).

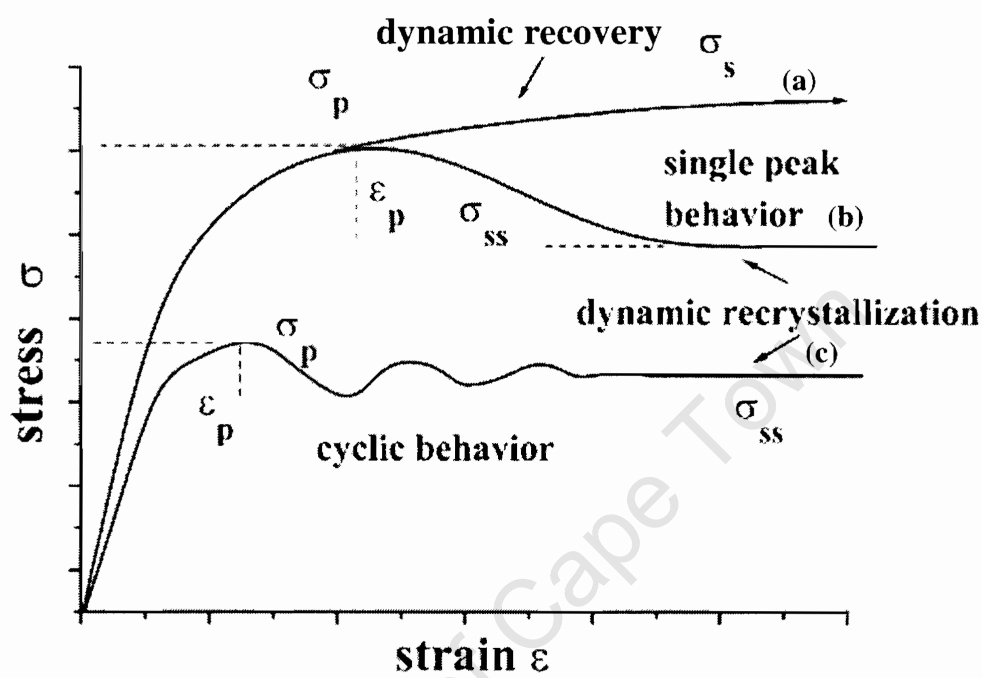

Figure 2-7: Illustration of the flow behaviour of austenitic stainless steels at high temperature[45].

The occurrence of DRV is often seen in flow stress curves as can be seen in Figure 2-7 curve (a). Initially there is a rise in the flow stress or strain hardening where dislocations interact and multiply. As the dislocations increase it gets harder and harder for them to move across each and hence the flow stress increases. The material work or strain hardens. The driving force and therefore the rate of recovery increases until a dynamic equilibrium is achieved between the rate of recovery and work hardening and a steady-state flow occurs. During steady-state flow, the dislocations produced are rearranged and annihilated and lead to the formation of a subgrain structure within the deformed grains. The deformed grains are elongated and have a pancake structure. Even though the high angle grain boundaries change in response to the external shape, the geometry of the substructure remains unchanged. Subgrains are finer at higher strain rates and lower temperatures.

If a critical strain (ε_c) is reached as in curve (b) and curve (c) in Figure 2-7 the stress can be seen to decrease after reaching a peak stress (σ_p). This is attributed to DRX. The flow curves associated with DRX may be single peak as in curve (b) or multiple peaks as can be seen in curve (c)[26]. As the Z parameter increases the flow behaviour changes from multiple to single peak. Then at large strains, steady state is reached where the creation and annihilation of dislocations is balanced.

2.5.7 Grain Growth

After classical or primary recrystallization, the structure is not stable. Further reductions in energy may occur by reducing the grain boundary area and its associated energy.

Two types of grain growth exist: normal grain growth and abnormal grain growth or secondary recrystallization. During normal grain growth the grain size distribution is in a narrow range. During abnormal grain growth a few grains grow in preference to others. These grains consume smaller grains and normal grain occurs when these grains start to impinge on each other.

Grain growth involves the migration of HAGB. The driving force for this is very small and significant grain growth is only likely to happen at high temperatures. The longer the annealing time the larger the grains grow which can be seen in Figure 2-8. Grain growth also results in softening of the material. This can be embodied by the Hall-Petch Equation[55]:

$$\sigma_y = \sigma_r + kd^{-0.5}$$

Equation 2-15

Where σ_y = yield point stress (MPa)

σ_r = stress to overcome resistance (MPa)

k = grain boundary resistance (MPa.μm$^{0.5}$)

d = grain size diameter (μm)

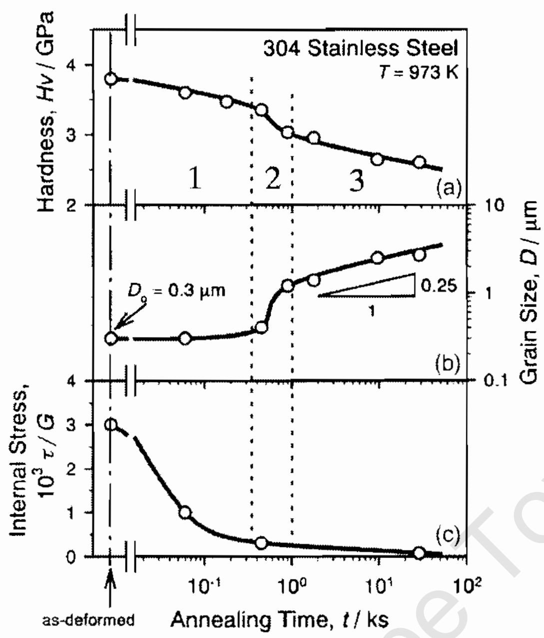

Figure 2-8: Grain size and room temperature hardness measurements as a function of annealing time at 700°C[56].

Further evidence of the increase in strength with decreasing grain size can be seen in Figure 2-8. If the material has undergone SRX, further softening of the material is possible by grain growth.

CHAPTER 3: EXPERIMENTAL METHODS

3.1 Material

The material used is AISI 304 stainless steel, which is the most commonly used stainless steel grade[57]. It is an austenitic stainless steel with low stacking fault energy and its main restoration mechanism is recrystallization.

3.1.1 Composition

The general composition of AISI304 stainless steel as well as the specific material used in this project is given in the table below:

Table 3-1 Composition of AISI304 stainless steel in weight percent.

Component	**Minimum**	**Maximum**	**Transfer Bar**	**Steckel Mill Sample**
Carbon, C		0.08	0.041	0.045
Chromium, Cr	18	20	18.12	18.15
Iron, Fe	66	74	71	72
Manganese, Mn		2	1.5	1.35
Nickel, Ni	8	10.5	8.08	8.11
Phosphorous, P		0.045	0.02	0.028
Sulphur, S		0.03	0.004	0.002
Silicon, Si		1	0.39	0.53
Molybdenum, Mo	-	-	0.074	0.1

The compositions are not very different between the transfer bar and the Steckel mill samples. The minimum and maximum levels given are the American Iron and Steel Institute (AISI) standard specifications for AISI 304[58].

3.1.2 Mill Samples

The samples were cut from the mill strip after the hot rolling process. These samples were then pulled onto the rolling table before being water sprayed on a down coiler. This water spray was to keep the coiler cool, not the strip. The parts were then cut 5 days after being rolled. How long this material was cooling is not known and furthermore the drop in temperature with time is not known. Unlike with lab simulation no after deformation quenching occurred to "freeze" the deformed microstructure.

The restoration state of these coils is not known after deformation. No quantitative statements can be made about the deformation of these coils from their analysis. What analysis can be done is comparative study of the variations in the strip in the normal direction (ND), in the transverse direction (TD) and between the middle section, the tail and head sections. These regions are shown as well as the rolling direction (RD) is presented in the figure below.

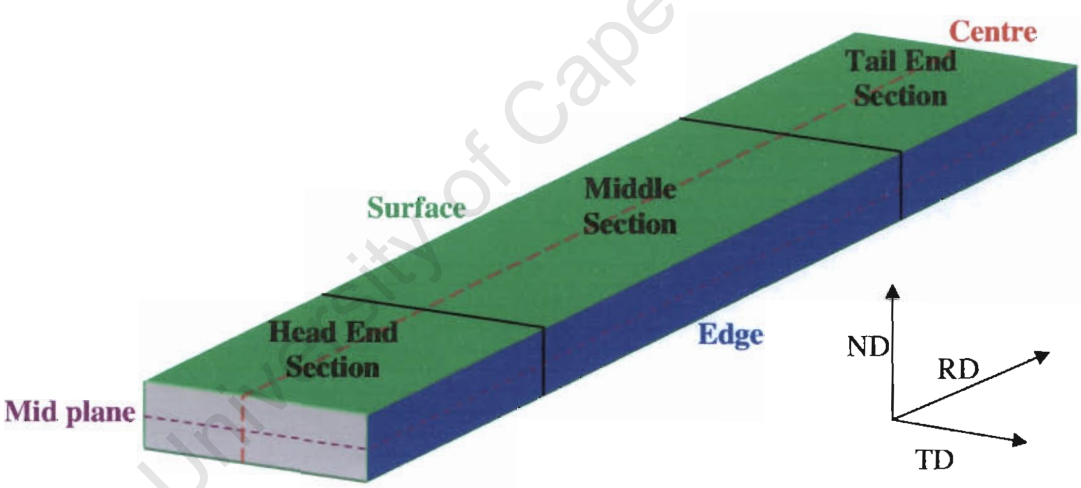

Figure 3-1: Naming conventions for various regions of the mill strip.

3.2 Axisymmetric Uniaxial Compression Testing

Various laboratory simulation tests exist for determining the deformation properties of materials. These tests include rolling, torsion, tensile and compression testing. A review of work done previously on AISI304 stainless steel is given in the Table 3-2. To properly simulate the properties in hot rolling, tests have to be done at high temperatures and strain rates and only plastic deformation is considered.

Table 3-2: Deformation Conditions for AISI304.

Grain Size	Test Type	Deformation Temperatures	Pre-deformation Heat treatment	Strain Rates	Sample Size*	Ref
μm		°C		s^{-1}	mm	
-	Torsion	1100 - 1250	1050°C for 30 minutes	0.1-100	7D, 28-7L	4
64	Torsion	900, 1000, 1100	1050°C for 30 minutes	0.1, 5	6.25D, 25.4L	25
-	Torsion	900 - 1100	-	5 - 0.05	10D, 20L	35
140-530	Torsion	950, 1050, 1150	1200°C for 30 minutes	1 and 0.047	7D, 7L	44
100	Torsion	900, 1000, 1100	1100°C for 30 minutes	5, 1, 0.5, 0.05	10D, 20L	59
100-180	Rolling	900, 1000, 1100	1200°C for 30 minutes	10	75, 13, 100	42
126	Rolling	1050, 1060, 1070	1200°C for 30 minutes	50 - 150	2 thick	43
100	Uniaxial Compression	800 - 1100	-	0.001 - 1	7D, 10L	33
40	Uniaxial Compression	850, 1150	1100°C for 15 minutes	0.0001 - 0.1	10D, 15L	45
50-220	Uniaxial Compression	1100	-	1	10D, 15L	60
80	Uniaxial Compression	1000 - 1250	1050°C for 30 minutes	0.001 - 100	10D, 15L	61, 54
20	Uniaxial Compression	850, 950	1050°C for 25 minutes	1	8D, 10L	62
25	Uniaxial Compression	600 - 950	-	0.0001 - 0.1	6D, 9L	63
25	Multi-axial Compression	600 - 950	-	0.0008	10, 10, 13	31
0.3	Multi-axial Compression	600	After 600 -900	0.001	5.0, 4.2, 3.5	56, 64

*Note D is diameter and L is length

Most testing done above was not performed at the parameters experienced in the Steckel mill rolling process. The tests that were performed at conditions close to the rolling process had different aims to the present study. Another factor that required more study was that although all these tests were performed on AISI304 stainless steel which has nominally the same composition, small compositional changes can give different results.

Careful consideration of the various tests is required to decide on the most appropriate to simulate hot rolling. Tensile tests are easy to carry out and the specimen is only subjected to a uniaxial stress that is simple to analyse. Tensile tests do have critical drawbacks. They cannot be used to produce flow curves since the amount of deformation before failure depends on the work hardening index. If the work hardening index is zero, which can occur at elevated temperatures, necking and failure occur with yield and little or no plastic deformation is possible. Thus tests are limited by the plastic instability.

Torsion tests do not have stability constraints but do have radial strain and strain rate gradients. These require the computation of surface equivalent stress and strain and tangential microstructural study. The practical maximum strain rate is $10s^{-1}$ which is insufficient to simulate some industrial rolling practices[65].

The most suitable testing method is compression testing. The preferred method of performing these compression tests is on a Cam Plastometer.

3.2.1 Cam Plastometer

Testing was done on the MTL Cam Plastometer at the Materials Technology Laboratory, a Canadian government testing facility, in Ottawa, Canada. The Cam Plastometer is designed to simulate industrial simulation processes especially hot rolling of plate in a laboratory environment[66].

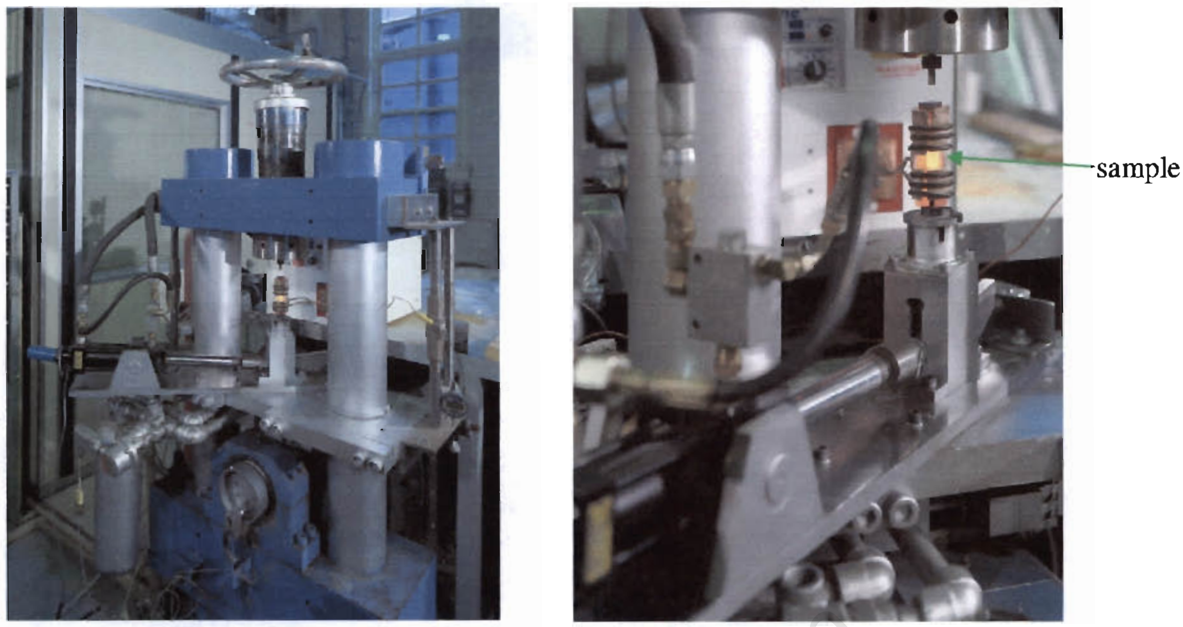

(a) (b)

Figure 3-2: Cam Plastometer side view showing close up of sample and induction coils.

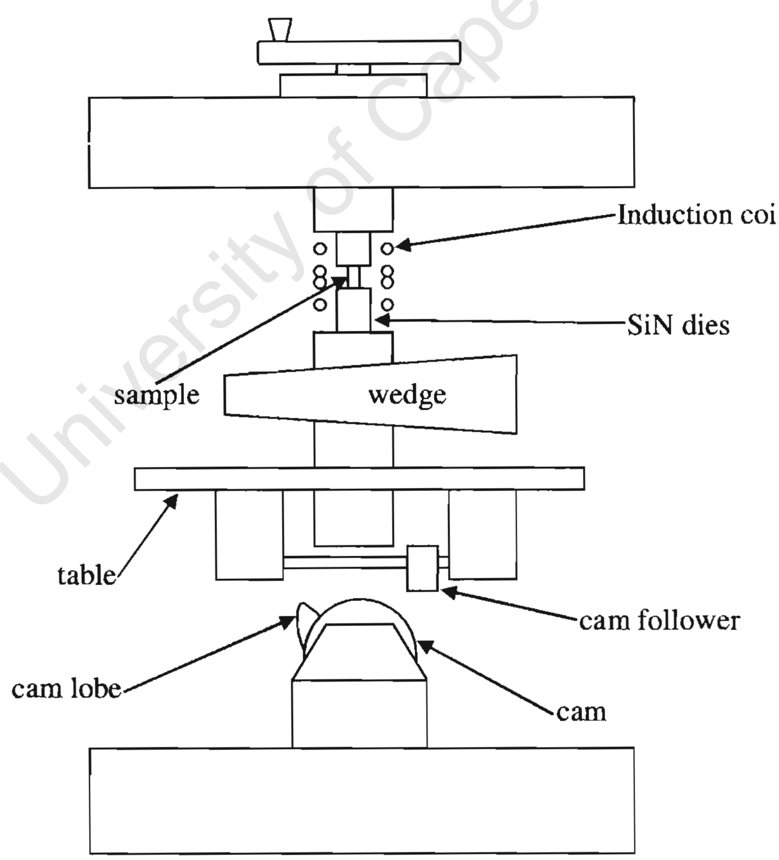

Figure 3-3: Schematic of Cam Plastometer adapted from Barager[66].

The deformation process is described with reference to Figure 3-3. The first step in the deformation process starts with the cam rotating. The cam follower is then shot across and when the cam lobe rotates pass the hit position, the lower bearing die is forced up compressing the sample which causes a gap in the load train. The cam follower is then retracted and the wedge moves across filling this gap preparing for the next hit. This process then repeats from the first step.

The cam shape is specially designed so that the strain rate remains constant throughout the deformation of the material. The rotation speed of the cam governs the strain rate and strain rates of $300s^{-1}$ have been achieved. The height of the cam lobe and relative position of the table dictates the reduction of the specimen. In this case, the reduction achieved was approximately 4mm. For different specimen heights, the reduction varied less than 10% due to elastic spring back of the material after the load is removed.

The heating is done through induction coils which heats a stainless steel susceptor that radiates heat to the dies. The dies are silicon nitride (SiN) which does not heat inductively. These allow temperatures of up to 1300°C to be achieved. The specimen is surrounded by an insulating blanket of fibre frax. This reduces heat loss from the specimen and ensures a more homogeneous temperature distribution across the specimen. The quenching was done manually. The operator manually pulled the specimen out by the thermocouple and submerged it in water. The delay time before quenching is estimated to be less than a second. The thermal mass of the specimen is quite small and consquently the time taken to reach the room temperature from the deformation temperature is considered to be negligible.

3.2.2 Specimen Preparation

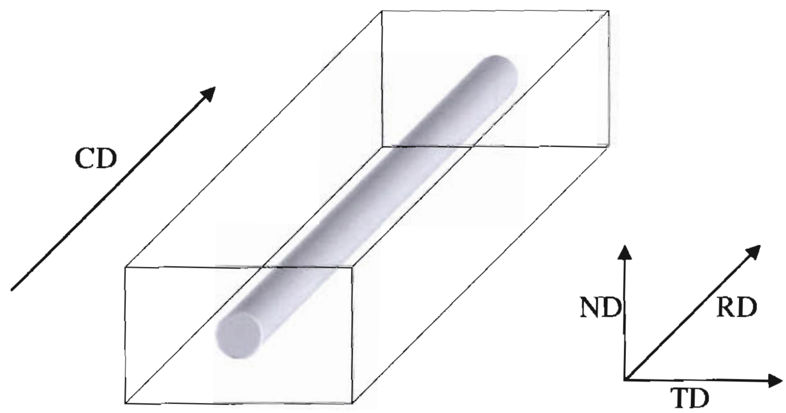

Figure 3-4: Schematic of cylindrical test specimen showing the compression axis direction (CD).

Cylindrical test specimens were cut from the transfer billet supplied by Columbus Stainless as indicated above. The specimens were heat treated at 1050°C for 30 minutes. At this temperature, all the carbide precipitates would also dissolve (see Figure 2-1). The heat treatment was done to homogenise the sample before testing, to ensure that all the tested samples were in the same condition prior to testing. The sample hardness is 162HV and the grain size is 35μm. Oil quenching was done to avoid carbide precipitation as can be seen from section 2.1.4.2. No martensite formation is possible by quenching since the M_s is –160°C, using Equation 2-2 and the composition data of the transfer billet from Table 3-1.

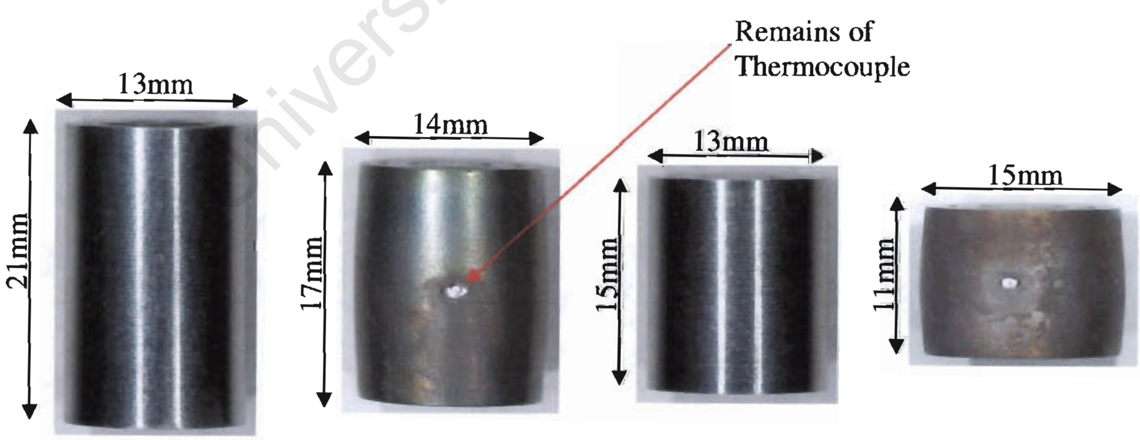

(a) **(b)** **(c)** **(d)**

Figure 3-5: Dimensions of single hit test specimens before and after testing: (a) and (c) is the starting sample for 0.2 and 0.3 strain respectively; (b) and (d) is the deformed specimen for 0.2 and 0.3 strain respectively. Diameter dimensions are given for widest part of specimen.

The specimen dimensions are given in Figure 3-5. The double hit specimens start dimensions are the same as Figure 3-5(a) and the final size diameter and height is 16mm and 13mm respectively.

Holes were drilled half height into each specimen for the thermocouple placement. The thermocouple was K-type, (Chromel-Alumel) sheathed in stainless steel. The thermocouple is welded into place and is sacrificed on every hit.

To prevent barrelling, lubricant is used between the deformation platens and the specimen. The lubricant used is a boron nitride powder. It is applied in an ethanol solution to ensure adherence to the specimen. The ethanol then evaporates off leaving the boron nitride. Grooves are machined into the specimen to keep the lubricant from escaping.

3.2.3 Barrelling

One of the biggest problems in direct compression is due to frictional effects between the specimen and the loading surface. The friction restricts the ends of the specimen from expanding in a radial direction. As a result cone shaped zones of relatively undeformed metal occurs at the ends[67]. These undeformed zones are known as dead zones and are illustrated in Figure 3-6.

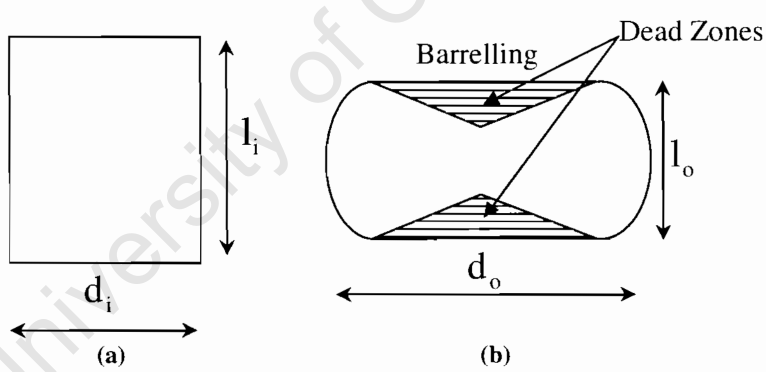

Figure 3-6: Uniaxial compression illustrating barrelling.

The barrelling coefficient B can be used to verify the validity of the compression test and whether or not friction compensation has to be applied. The barrelling coefficient is given below[68, 69]:

$$B = \frac{l_o d_o^2}{l_i d_i^2} \quad \textbf{Equation 3-1}$$

Where: l_i = initial height (mm)

l_o = deformed height (mm)

d_f = initial diameter (mm)

d_o = deformed diameter (mm)

In Evan's work[68], the maximum deformed diameter is used and in the Gleeble notes[69], an average of four diameter readings is taken. In the first case, the barrelling coefficient will always be greater than or equal to 1 whereas in the second case the barrelling coefficient could be less than 1.

According to the Gleeble Notes the need to correct for flow stress is only required when the barrelling coefficient is lower than 0.9. The barrelling coefficients were calculated and were all greater than 0.9.

If the barrelling coefficient is greater than 0.9, the strain distribution would be inhomogeneous in the specimen, with lower strains at the interfaces and the highest strain at the centre. The actual flow stress would be higher[70].

3.2.4 Deformation Conditions

The deformation conditions were based on processing parameters in the Steckel mill. Further considerations were limitation imposed by the Cam Plastometer. The deformation parameters are given below.

Table 3-3: Strain Rate Range

Temperature (°C)	Strain	Strain Rates (s^{-1})
1000	0.30	30, 60, 90,120

Table 3-4: Temperature and Strain Range

Temperatures (°C)	Strain	Strain Rate (s^{-1})
900, 950, 1000, 1050	0.30	60
850, 900	0.20	20

All conditions listed in the above table are based on the Steckel mill logs.

The test conditions (for single stage)

1. Heat up to deformation temperature and hold for one minute.
2. Deformation event.
3. Immediate quench to room temperature.

Table 3-5: Double hit strain rate and temperature range

Temperatures (°C)	Strain	Strain Rate (s^{-1})
800, 850, 900, 950,1000, 1050	0.20 + 0.25	60

The test conditions (for double stage)

1. Heat up to deformation temperature and hold for one minute.
2. First deformation event.
3. Hold for 60s.
4. Second deformation event.
5. Immediate quench to room temperature.

3.3 Characterisation of Post-Deformation Softening

Post deformation softening can be used to calculate the fraction recrystallized. Softening may be due to recovery or recrystallization. The contribution of these effects will be established below.

3.3.1 Restoration of Yield

The restoration of yield may be used to determine the interpass softening. The difference in yield stress between the first and second hit may be used to calculate the restoration of yield stress (FS)[71]:

$$FS = \frac{\sigma_f - \sigma_{y2}}{\sigma_f - \sigma_{y1}}$$ **Equation 3-2**

Where: σ_f = flow stress after the first pass (MPa)

σ_{y2} = yield stress of the second hit (MPa)

σ_{y1} = original yield stress during first compression. (MPa)

The restoration of flow stress includes the restoration effects like static recovery.

3.3.2 Restoration of Hardness

Isothermal heat treatments were performed in a salt bath to ensure temperature homogeneity of the specimens and to ensure that the specimens reached the required temperature in the shortest possible time. Immediately following the heat treatment the samples were oil quenched to "lock in" the heat treated microstructure and to prevent carbide precipitation.

The fraction softened (X_h) for AISI304 stainless steel is defined as follows[43], [44], [62]:

$$X_h = \frac{h - h_i}{h_f - h_i}$$

Equation 3-3

Where: h = instantaneous measured hardness (HV)

h_i = initial hardness (HV)

h_f = fully recrystallized hardness (HV)

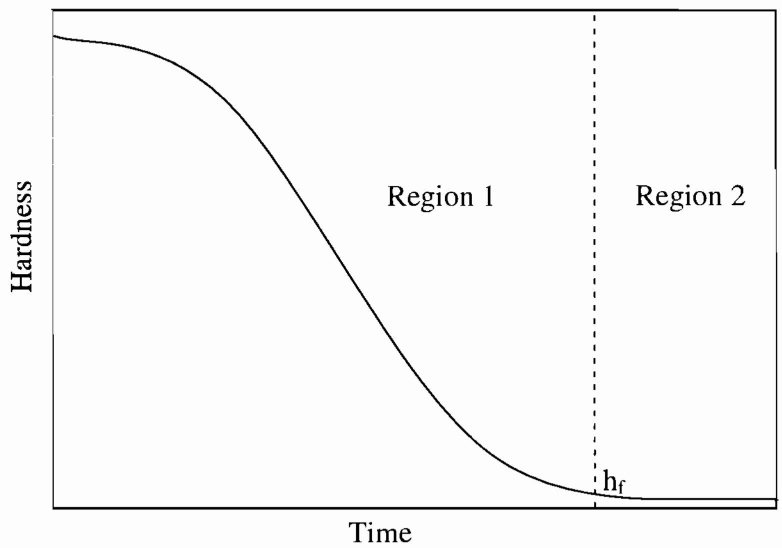

Figure 3-7: Determination of h_f adapted from Sheen[62].

Typical hardness curve is given in Figure 3-7. Region 1 represents the area where recrystallization is the only measurable phenomenon and Region 2 the area where other phenomena dominate like grain growth. Grain growth occurs during Region 1 but its effects can only be seen in Region 2. A change in the rate of change of hardness is observed between the two regions. The h_f value is determined from the transition point between the two regions. A point of inflexion occurs and the hardness levels off.

The literature differs on the relationship between X_{srx} and X_h for AISI304 stainless steel. These relationships are to compensate for any recovery. Barraclough[44] proposes the relationship given in Figure 3-8. Zhang[43] utilises a 5% recrystallized state as h_i and establishes h_i by metallography. Sheen determined that the X_h equals the X_{srx} within experimental error and establishes this relation by using electron backscatter diffraction. Sheen's work was performed on AISI304 stainless steel that is from the same source as the present study and therefore that is the relationship used.

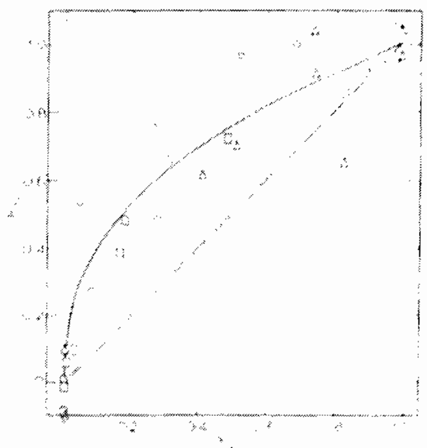

Figure 3-8: Relation of restoration of hardness (R_h) to fraction recrystallized (X_v) for AISI304 stainless steel[44].

The total error w_R associated with X_{srx} was calculated using the following formula[72]:

$$w_R = \left[\left(\frac{\partial R}{\partial x_1} w_1 \right)^2 + \left(\frac{\partial R}{\partial x_2} w_2 \right)^2 + \ldots + \left(\frac{\partial R}{\partial x_n} w_n \right)^2 \right]^{1/2}$$

Equation 3-4

Where: x_i = independent variables

R = function of the variables

w_i = error associated with each variable. The error in this case was assumed to be the standard deviation of the hardness indents.

Evaluating Equation 3-4 with respect to Equation 3-3, we get:

$$w_R = \left[\left(\frac{w}{h_f - h_i} \right)^2 + \left(\frac{w_f (h - hi)}{(h_f - h_i)^2} \right)^2 + \left(\frac{w_i (h - h_f)}{(h_f - h_i)^2} \right)^2 \right]^{0.5}$$

Equation 3-5

Where: w = standard deviation of instantaneous measured hardness (HV)

w_i = standard deviation of initial hardness (HV)

w_f = standard deviation of fully recrystallized hardness (HV)

3.3.3 Determination of Time to 50% recrystallization

Rearranging Equation 2-8 in section 2.5.3 into a straight line equation form of $y = mx + c$, the Avrami Constant(k) can be calculated[62]:

$$\ln\left(\ln\left[\frac{1}{1-X_{srx}}\right]\right) = \ln(\ln 2) - k\ln(t_{0.5}) + k\ln(t)$$

Equation 3-6

Where: $y \quad = \quad \ln\left(\ln\left[\frac{1}{1-X_{srx}}\right]\right)$

$x \quad = \quad \ln(t)$

$c \quad = \quad \ln(\ln 2) - k\ln(t_{0.5})$

$m \quad = \quad k$

Assuming the following constants for Equation 2-9, which are the most popular of the equations in the literature:

$$t_{0.5} \quad = \quad A\varepsilon^{-2}D_o^2 Z^{-0.375}\exp\left[\frac{Q_{srx}}{RT}\right]$$

Equation 3-7

$$\Rightarrow \ln(t_{0.5}) = \frac{Q_{srx} - 0.375(Q_{def})}{R}\left(\frac{1000}{T}\right) + \ln\left(A\varepsilon^{-2}D_o^2\dot{\varepsilon}^{-0.375}\right)$$

Equation 3-8

where: $y \quad = \quad \ln(t_{0.5})$

$m \quad = \quad \frac{Q_{srx} - 0.375(Q_{def})}{R}$

$x \quad = \quad \left(\frac{1000}{T}\right)$, T is both the annealing and deformation temperature

$c \quad = \quad \ln\left(A\varepsilon^{-2}D_o^2\dot{\varepsilon}^{-0.375}\right)$

The values of A and Q_{srx} can be calculated from the above relations

3.4 Mill Log Calculations

Industrial mill logs contain information like temperatures, loads and various dimensions of the strip being worked. They are invaluable in predicting the microstructural evolution of the strip through the rolling process and the end properties.

3.4.1 Mean Flow Stress

Mean flow Stress (MFS) can be defined mathematically by integrating under the stress strain curve[38]:

$$\mathrm{MFS} = \frac{1}{\varepsilon_2 - \varepsilon_1} \int_{\varepsilon_1}^{\varepsilon_2} \sigma \, d\varepsilon$$

Equation 3-9

Analysis of the MFS curves versus the inverse absolute temperature allows the various metallurgical phenomena that occur during hot deformation to be identified and provides insight into how the microstructure is evolving. It also demonstrates the dependence of hot strength on temperature[73]. This lays the foundation to connect mill operation variables to an online determination of microstructure evolution and prediction of the properties and shape. This analysis is illustrated in Figure 3-9 by the changes in slope of curve. A five pass schedule is shown.

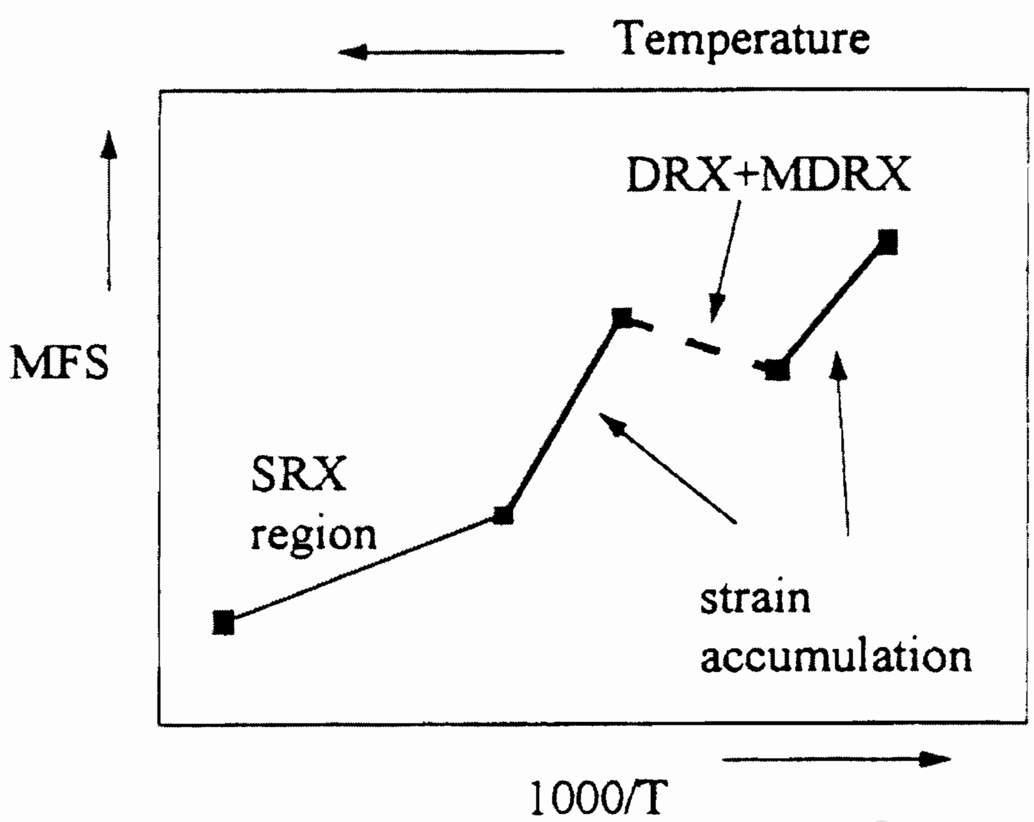

Figure 3-9: MFS plotted against inverse absolute temperature. Changes in slope are indicative of changes in microstructure[74].

The passes begin from the left hand side. The shallower slope indicates that static recrystallization (SRX) has occurred on the interpass between pass 1 and 2. The temperature is too low after pass 2 and the steeper slope shows strain accumulation. This strain accumulation leads to dynamic recrystallization (DRX), then metadynamic recrystallization (SRX) between pass 3 and 4.

3.4.1.1 Calculating Mean Flow Stress

Since the process conditions vary through the thickness of the metal strip, the flow stress would vary through the thickness of the strip. The mean flow stress is just an average value of flow stress in the strip during a pass.

Calculating MFS and various other parameters is quite dependent on the assumptions made which shall be discussed below.

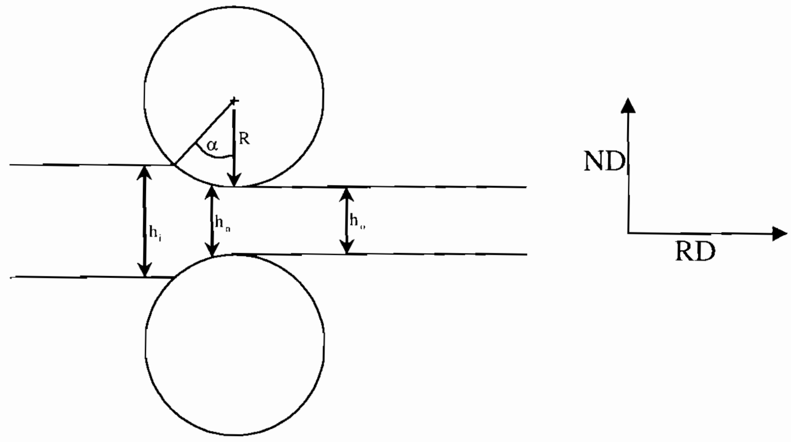

Figure 3-10: Rolling nomenclature, the normal direction (ND) and is the rolling direction (RD) are indicated.

The equation for calculating the mean flow stress ($\overline{\sigma}$) was first given below[75, 76]:

$$\overline{\sigma} = \frac{\sqrt{3}}{2}\frac{P}{wQ\sqrt{R'(\Delta h)}}$$

Equation 3-10

Where: w = width of strip (mm)

R' = flattened work roll radius (mm)

Δh = draft = $h_i - h_o$ (mm)

h_i = input gauge or thickness (mm)

h_o = output gauge or thickness (mm)

P = roll force (N)

Q = geometric factor in flow stress calculations (dimensionless)

$$Q = \frac{1}{2}\left(\sqrt{\frac{1-r}{r}}\right)\left(\pi \tan^{-1}\sqrt{\frac{r}{1-r}} - \sqrt{\frac{R'}{h_o}}\ln\left[\left(\frac{h_n}{h_o}\right)^2(1-r)\right]\right) - \frac{\pi}{4}$$

Equation 3-11

Where: r = reduction $= \frac{\Delta h}{h_i}$ (dimensionless)

The various assumptions made in deriving Equation 3-10 are given below:

3.4.1.2 Stress and Plasticity Assumptions

The strip material is assumed to be plastic rigid. This means the Young's Modulus is considered infinite and any elastic behaviour of the strip is ignored.

The deformation of the sheet is in plane strain. This means that the strain in the sheet is inhibited laterally or in other words in the direction parallel to the roll axis. This assumption is appropriate in cases where the width to thickness ratio is greater than 10:1. The stress in plane strain compression or the constrained yield stress is not equal to the flow stress. Using the Huber-Mises Theory for plastic yielding the relationship between the two variables is[77]:

$$\overline{\sigma} = \frac{\sqrt{3}}{2} k$$

Equation 3-12

Where: k = constrained yield stress or stress in plane strain compression (MPa)

3.4.1.3 Friction

There are two types of friction encountered in rolling namely sticking friction (static) and slipping friction (dynamic). With the static friction condition, the contact area of the strip moves at the same rate as the work rolls. Slipping friction allows different regions of the contact area to move at different rates. In this case only one region of the roll moves at the same speed as the work roll, which is at the neutral plane (thickness of plate in neutral plane equals h_n). By considering mass flow equations, it can be seen that the strip moving out of the roll moves quicker than the strip moving in.

In actual rolling the friction is a combination of slipping and sticking, with sticking around the neutral plane area and slipping on the edges of the contact area. Furthermore, in cold rolling more slipping friction is seen with the effective lubricants used. In hot rolling often, welding of the strip to the rolls can occur and in view of the uncertainty and for simplification, sticking friction with a constant friction coefficient is assumed over the whole contact arc.

3.4.1.4 Hitchcock Equation for Flattened Work Roll Radius

The radial stress exerted between the work rolls and the strip surface results in elastic deformation of the work rolls. This deformation is termed roll flattening. To compensate for roll flattening, Sims proposed that the radius of curvature remains constant over the contact area. The new radius is then calculated using Hitchcock's formula as follows[78 - 80]:

$$R' = R\left(1+\frac{PC}{w\Delta h}\right)$$

Equation 3-13

Where: R = nominal radius of work rolls (mm)

C = work material parameter (GPa^{-1}) and is given below:

$$C = \frac{16(1-\nu^2)}{\pi E}$$

Equation 3-14

Where: ν = Poisson's ratio for outer shell of work roll material (0.3)

E = Young's modulus for outer shell of work roll material (180GPa)

The work rolls experience thermal fatigue due to frequent thermal shocks. This results in thermal fatigue cracks on the work roll surface. The work rolls are then dressed by skimming and grinding to remove the cracks. This dressing reduces the work roll radius. In the present study, the Steckel mill diameter is 750mm when new and 690mm before the outer shell is replaced.

3.4.2 Temperature

The temperature is one of the most important factors in deciding the recrystallization behaviour and therefore the end properties. Therefore it is worthwhile analysing the mill temperatures in depth for an increased understanding of the process.

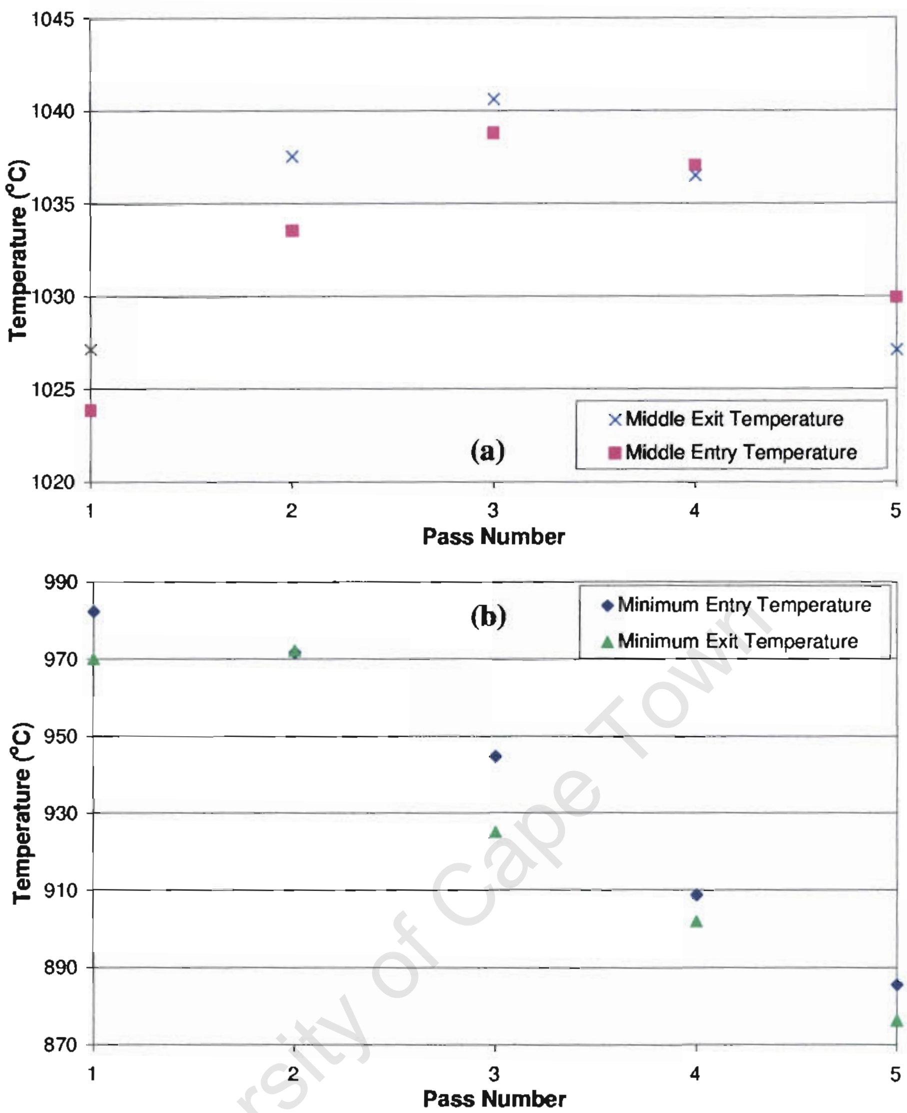

Figure 3-11: Each point represents an average of 5 roll schedules. In (a) the temperature represents the temperature at the middle section of the strip and (b) the lowest temperatures recorded. The mill data is given in Appendix A.

Temperature at each pass taken of the surface of the strip 3.5m before work roll for the entry and 3.5m after work roll for exit with an optical pyrometer.

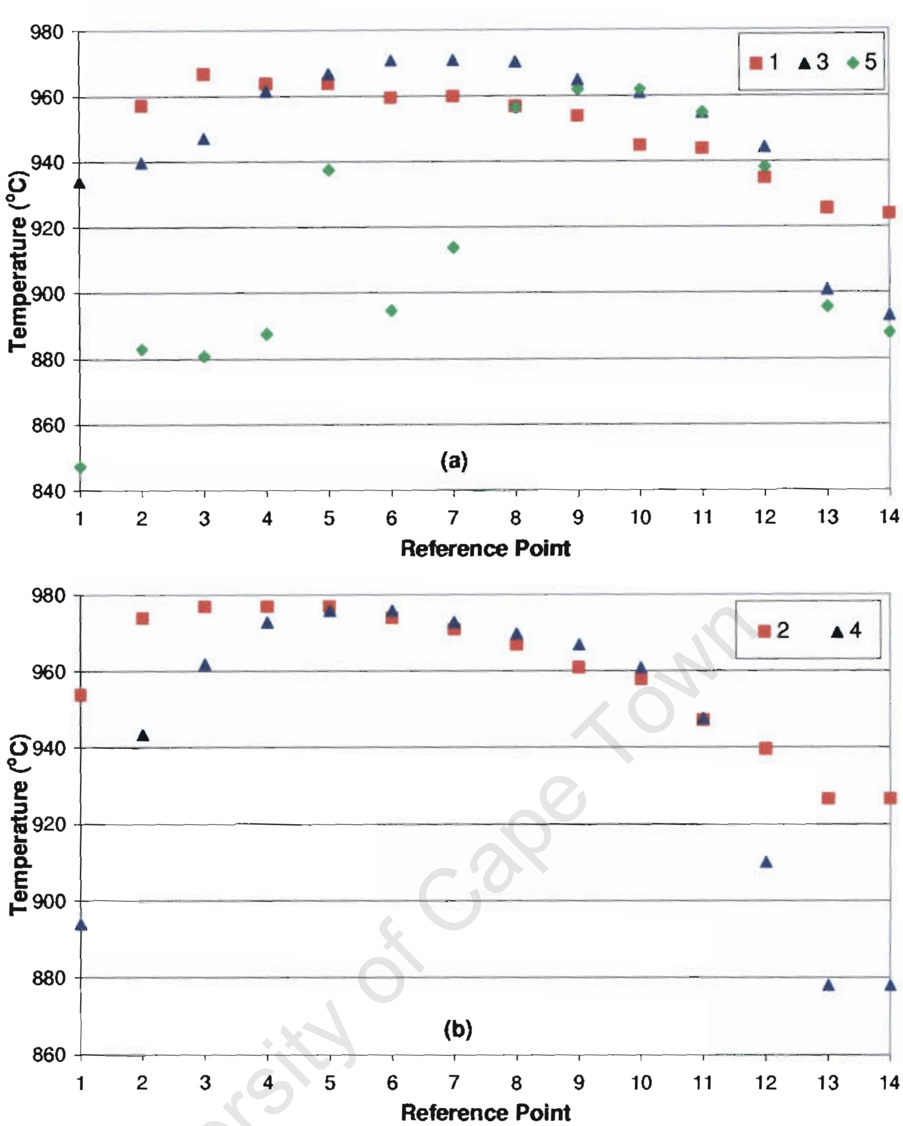

Figure 3-12: Temperatures at various points on the mill strip per pass is given. Detailed data for one heat given. The odd passes are plotted in (a) where the head section (reference point 1) is leading and the even passes in (b) where the tail section (reference point 14) is leading. Data is given in Appendix A.

From Figure 3-11 (a), temperature rises from pass 1 to pass 3. In those passes, the exit temperature is higher than the entry temperature. Both these effects can be attributed to the adiabatic heating from deformation. Approximately 99% of the energy from deformation is given off as an increase in temperature, the rest is stored energy.

The temperatures decrease from passes 3 to 5 in Figure 3-11 (a) where it can be seen that the increase in the surface area of the strip and therefore increased contact with the air, dominates the over the adiabatic heating effect. In Figure 3-11(b), the minimum temperature decrease continuously.

In Figure 3-12 , the temperature is plotted along each $^{1}/_{14}{}^{th}$ of the strip. These temperatures are lower than those in Figure 3-11. The temperature of the transfer billet from the rougher mill is higher in the latter case. The reference point 1 is the head section and reference point 14 is the tail section. As the rolling proceeds, these points will get further and further apart with the increasing length of the strip. The temperature distribution is roughly maintained through the passes with the bulk being warmer than the ends and the tail section being colder than the head section. The tail section is colder than the head section because the cold part of the head section was cropped after the roughing process. This shows the thermal retention of the strip in the early passes. The head section does eventually become colder than the tail section in the last pass. The leading end of the strip protrudes from the hot coil furnace and on the last pass it is the head end. This is when the gauge thickness is at its lowest, the thermal retention is at its lowest and the head end experiences the lowest temperature.

The inverse temperature versus mean flow stress was plotted for the ends and the middle section. The temperatures used for the middle section was plotted using an average of the middle section exit and entry temperatures and the temperatures for the ends were plotted using the minimum temperatures.

3.4.3 Strain

The effective nominal strain is calculated according to the following formula[76, 81]:

$$\varepsilon_n = \frac{2}{\sqrt{3}} \ln\left(\frac{h_i}{h_o}\right)$$

Equation 3-15

An additional strain amount occurs due to the finite length of the working zone and the work required "folding" and "unfolding" the material as it leaves the deformation zone. This is the redundant strain (ε_r)[82]:

$$\varepsilon_r = \frac{\Delta h}{4\sqrt{4R'^2 \sin^2\left(\frac{\alpha}{2}\right) - \frac{(\Delta h)^2}{4}}}$$

Equation 3-16

The total strain (ε_i) for the i^{th} pass is then

$$\varepsilon_i = \varepsilon_r + \varepsilon_n$$

Equation 3-17

During rolling the strain accumulates depending on the amount of recrystallization that has taken place. If the material fully recrystallizes, no strain will accumulate. To accommodate this we calculate the accumulated effective strain (ε_a) in the i^{th} pass and the following equation is used[23]:

$$\varepsilon_a = \varepsilon_i + (1 - X_{i-1})\varepsilon_{a-1}$$

Equation 3-18

Where: ε_{a-1} = Accumulated strain in pass i-1

X_{i-1} = Fraction recrystallized in pass i-1

3.4.4 Strain Rate

The two different conditions of friction should be considered when determining the strain rate in the roll gap, whether the condition for friction is static or dynamic. As was mentioned in section 3.4.1.3, the condition of static friction was assumed, so the work rolls move at the same speed as the strip in the area of contact. The average effective strain rate ($\dot{\varepsilon}$) is given below[76]:

$$\dot{\varepsilon} = \frac{\varepsilon}{t}$$

Equation 3-19

Where: t = Time to move through the angle of bite, (α).

$$t = \alpha \div \frac{2\pi U}{60}$$

Equation 3-20

Where: U = angular speed in rpm

α = contact angle (radians) or angle of bite $= \cos^{-1}\left(1 - \frac{\Delta H}{2R}\right)$

Referring to section 2.1.5.1 on the Steckel mill the strip is threaded into the work rolls at a slower speed and then accelerates to roll speed, after which it decelerates again. The inlet roll speed was ascribed to the ends and the roll speed to the middle section.

3.4.5 Interpass Time

The restoration time of various parts of the mill strip is important in considering the metallurgical evolution of the mill strip. The interpass time represents the restoration time between deformation events in consecutive passes.

The roll time is given on the mill logs and represents the physical roll time of the whole strip. The material spends about 5 to 7 seconds between the actual passes. This time is not included in physical roll time. During this time the roll gap is adjusted in preparation for the next pass.

The middle section interpass time is then calculated by taking an average of consecutive roll times and adding 6 seconds for the roll gap adjustment. The idea is illustrated in Figure 3-13. This time would only represent the central line of the middle section with material entering the roll gap before this region having a shorter interpass time and the material leaving the roll gap after this region section having a longer interpass time.

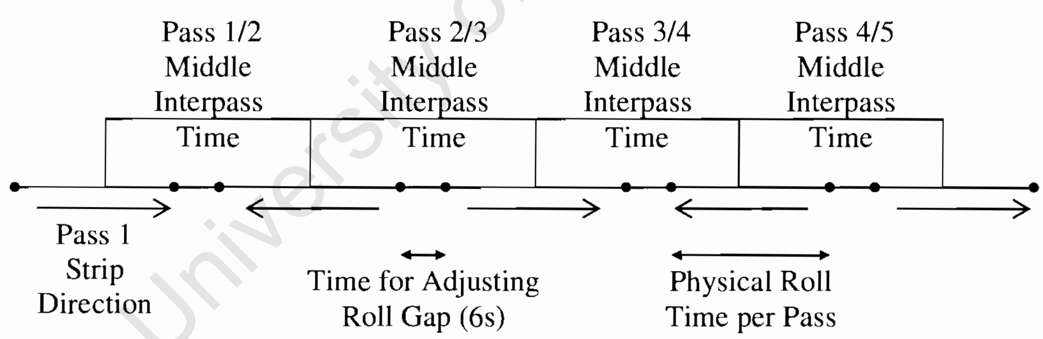

Figure 3-13: Timing in a 5 pass schedule illustrating middle interpass time.

The head and tail interpass time are calculated by the addition of consecutive physical roll times and adding 6 seconds. This is shown schematically in Figure 3-14.

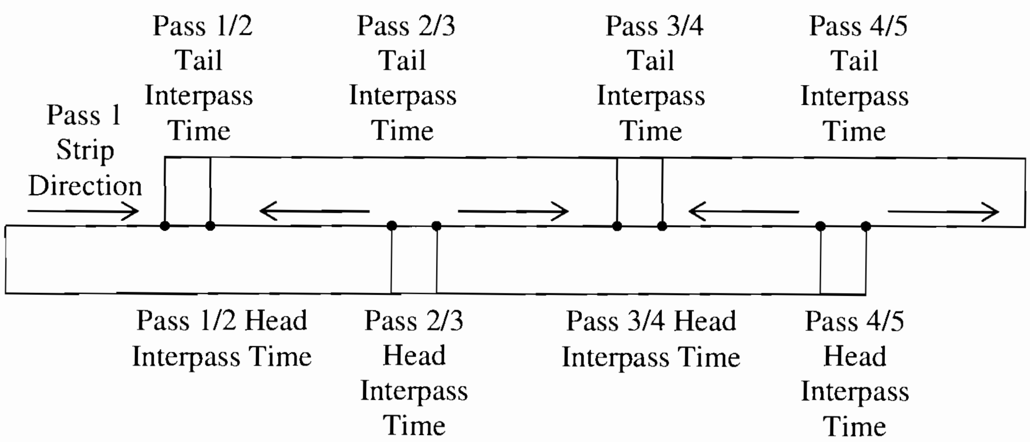

Figure 3-14: Calculating the end interpass times.

3.4.6 Calculating the Grain Size

The time to 50% recrystallization ($t_{0.5}$) is very dependant on the grain size as was explained in section 2.5.4.3. The finer the grain size the more sites there are for recrystallization therefore the shorter the $t_{0.5}$. Of the two equations presented, Equation 2-12[40] is used since the ε_p value in Equation 2-13 is not known. Equation 2-12 is presented again below but relabeled for use in mill log calculations.

$$D_i = A'\varepsilon_i^{-0.75} D_{i-1}^{0.5} Z_i^{-0.1}$$

Equation 3-21

Where: D_i = recrystallized grain size after i^{th} pass

Z_i = Dynamic Recovery, Z parameter in i^{th} pass (352 kJ.mol^{-1} for AISI304 stainless steel)

ε_i = accumulated strain in the i^{th} pass

A' = constant (value is $71.4\,s^{0.1}\mu m^{0.5}$ for AISI304 stainless steel)

Note that there is no time associated with this equation. The grain size is calculated after recrystallization is complete and does not take grain growth effects into consideration. The original grain size is required and is calculated from the transfer billet using the method which is described in section 3.5.2. For verification the final grain size is calculated and compared with the results from this analysis

3.4.7 Steady State Stress

The steady state stress is a way of combining strain rate, temperature and material properties as a single quantity. It has a drawback of being independent of strain but is still a useful parameter.

The steady state stress is calculated from the universal hot working equation (Equation 2-6). The equation constants are from Smal and Stumpf[24] and are given in Table 2-2. These values are used because the material originates from the same source as the present study and would have a similar composition. The equation with constants would be:

$$\dot{\varepsilon}\exp\left(\frac{434000}{RT_{def}}\right) = 5\times10^{-15}(\sinh 0.012\sigma)^{4.7}$$

Equation 3-22

3.4.8 Finite Element Analysis of through thickness deformation conditions

In a parallel study done by Floweday[83], a finite element model was done to evaluate the through-thickness variations in the strip, to show if the through thickness variation is significant. The data outputs from Floweday's are analysed in the present study. A 2-d model was done with nine elements through thickness. As can be seen in Figure 3-15, elements are labelled 60 at the mid plane and 1020 at the surface of the strip. The strain, temperature and strain rate history of these elements as they move between the roll gap are presented. The data presented here is of the first pass outputs. The mill log data was used as the inputs. The raw data is given in Appendix A.

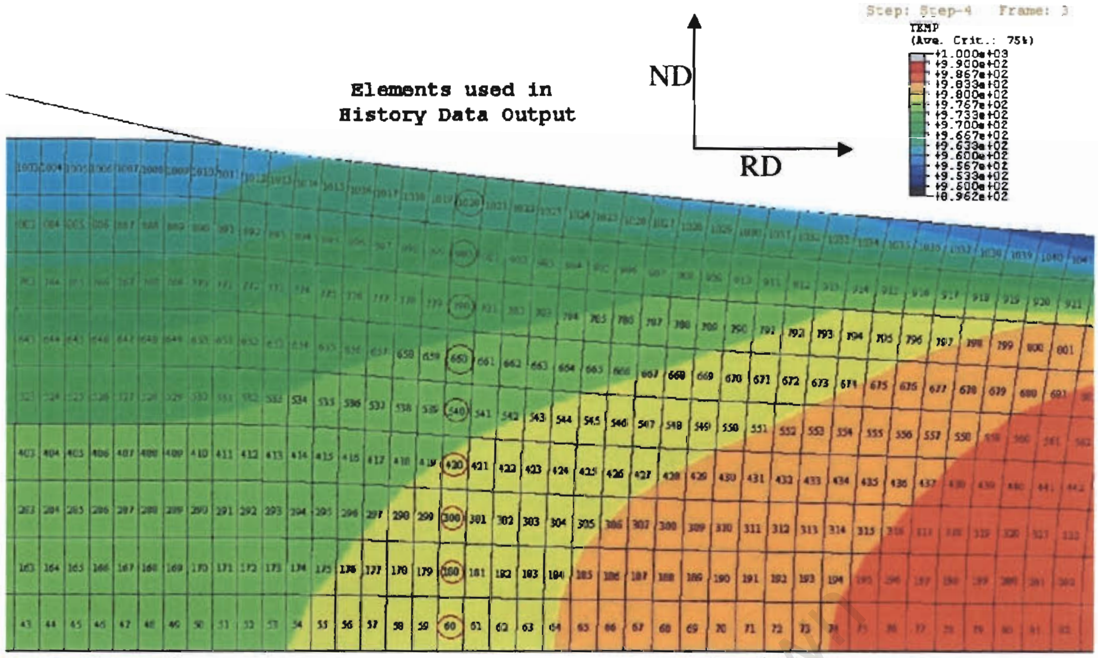

Figure 3-15: Graphical finite element output, showing the temperature profile[83]. The rolling direction (RD) and the normal direction (ND) are indicated.

The elements are relabelled for clarity.

Table 3-6: New element labelling.

60	180	300	420	540	660	780	900	1020
M1	M2	M3	M4	M5	M6	M7	M8	M9

M1 would be the mid plane element and M9 would be the surface element

3.4.8.1 Assumptions

The material was assumed to be fully annealed after each pass. This means the strain is reset to zero after each pass. Compression is assumed to be plane strain, so the strains normal to the page are zero. These strains are for the rolling direction and are numerically equal to the strain through thickness due to the plane strain assumption.

3.5 Microstructural Analysis

The specimen preparation procedure is very important for the microstructural analysis. The way the material is cut, polished and grinded are all important considerations.

The specimens were polished with a modified Struers™ Method C polishing method. The forces associated with method C were found to cause martensite formation which would mask the microstructure. The specimens were then electropolished for electron backscatter diffraction.

3.5.1 Microscopy

The samples were hot mounted in a clear acrylic resin. Two different etchants were used to reveal different microstructures. A general etchant which revealed annealing twins was oxalic acid 10g and 100 ml water at 10V for approximately 25s to 60s. The condition of the material dictated the etching conditions. An etchant of 60% nitric acid and 40% water was used to reveal grain boundaries and grain shape[84]. The voltage was set at 1.6V and the current was approximately $10 mA.cm^{-2}$.

3.5.2 Grain Size Calculation[85]

The grain size was calculated using the Heyn Intercept method. Lines are superimposed on the micrograph in the form of a grid. The magnification was 50 times. The line intercepts with boundaries are counted. Twin boundary interceptions are ignored. Where the lines intersect triple points or are tangential to boundaries the interceptions are counted as 1.5 and 0.5 intercepts respectively. To ensure the results are statistically meaningful at least 50 intercepts are required per field of view. The mean intercept length which represents the grain size is given below

$$\bar{L}_3 = \frac{L_T}{P}$$

Equation 3-23

Where: P = number of interceptions with the grain boundaries

L_T = Total length of line (μm)

$\bar{L}_3$ = Mean intercept length (μm)

To obtain the aspect ratio, the mean length intercept is calculated for parallel lines and perpendicular lines separately and a ratio obtained between the two.

The error associated with grain size is calculated by taking an average of 10 fields of view of the same sample and calculating the standard deviation. The standard deviation was calculated to be 1.0HV

3.5.3 Hardness Testing

Mechanically polished specimens were used for microstructural analysis. All hardness tests were done on the Highwood Digital Micro hardness tester, model HWDM-3. The load was decided by a few factors. The hardness was done in Vickers that requires making a square indent and measuring the diagonals. The formula for converting the indent size to hardness Vickers (H_v) is given in Equation 3-24[86, 87].

$$H_v = \frac{1854.4W}{D^2}$$

Equation 3-24

Where: W = Load in g F in this case 2000g

D = Length of the diagonal (μm)

The spacing between the indents has to be conservatively greater than three diagonals. This was done to ensure that the strain field caused by an indent does not interfere with the next indent made. The indent has to be at least three diagonals from an edge. The size of the indents has to be greater than the grain size. If this was not done then the indent inside a grain would be bigger than an indent on a grain boundary. The grain size in this case was approximately 30μm. The accuracy of the hardness indent is suggested, from literature, to be 1.5μm under good optical conditions.[87] Making the indent bigger reduces the percentage error. With the diagonal being 120μm, this gives an error of less than 1%. For the compression test samples, 9 indents represented one data point and for the plate samples, 3 indents all the same distance from the edge, represented one data point.

3.5.3.1 Sampling procedure

Certain areas of the mill strip material were sampled. These are shown in Figure 3-16.

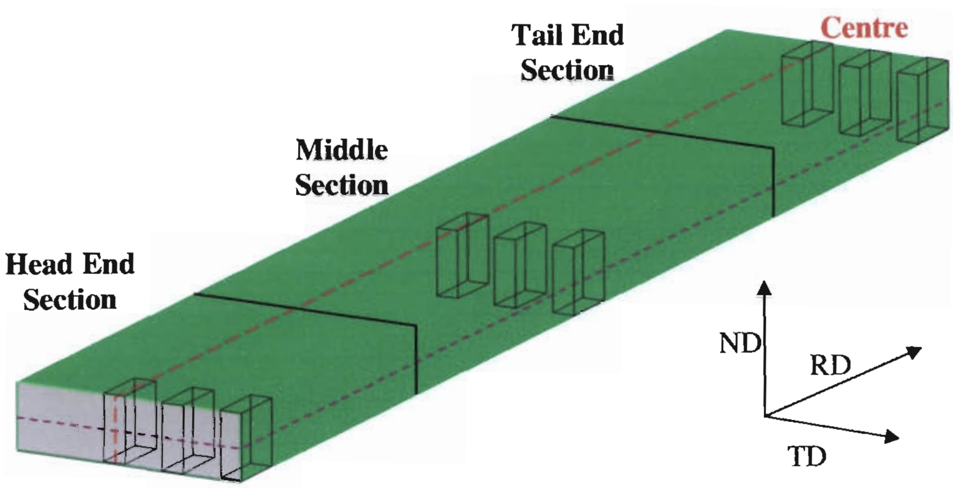

Figure 3-16: Illustration of sampling for metallographic examination on mill strip.

Three samples (shown as box outlines above) are taken from each section, the middle, head and tail section.

In order to maintain consistent results for each sample, hardness testing was done on a 3 by 3 grid. Indentations were made on the specimen in the centre of the specimen for the compression samples and starting 0.5mm from the edge for the plate samples. The sampling distance is 1mm between indents and therefore a 2mm square grid of 9 indents would result. For the compression test samples 9 indents represented one data point and for the plate samples 3 indents, all the same distance from the edge, represented one data point.

3.5.4 Electron Backscatter Diffraction

Electron backscatter diffraction (EBSD) is a technique that allows crystal orientation relationships or texture relationships to be obtained from the Scanning electron microscope (SEM). The SEM is a Cambridge Stereoscan 200. The CCD camera is combined with phosphor screen in one unit the HKL detector. The system setup is shown in Figure 3-17. The image processor was a Hamamatsu Argus 20 digital processor.

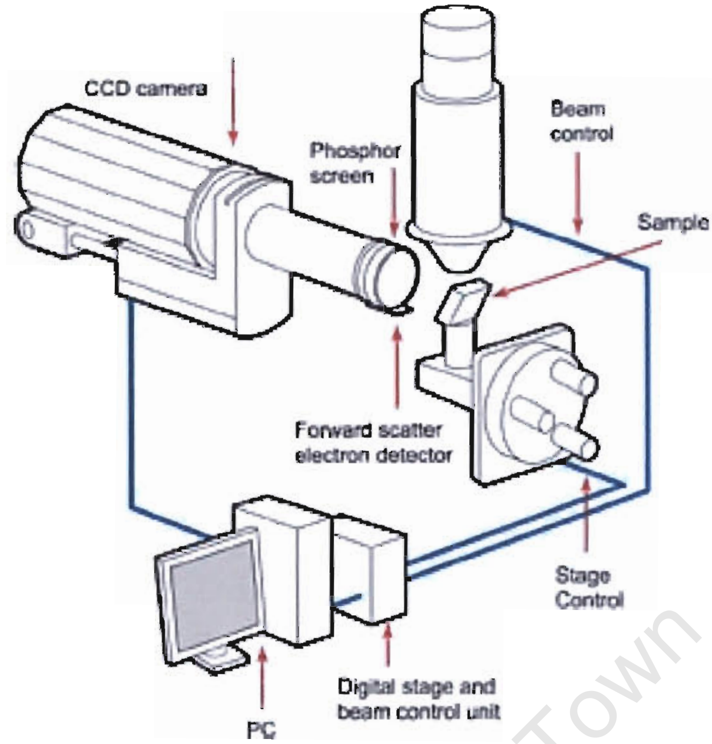

Figure 3-17: Schematic of SEM and EBSD setup.

3.5.4.1 Sample Preparation

The sample preparation for the SEM is similar to that for the optical microscopy. The difference lies in the fact that the diamond polishing stage introduces a deformed layer. The electrons only penetrate less than 100nm into the specimen surface. This deformed layer reduces the EBSD pattern quality. The sample is mechanically polished with the Struers Method "C" technique as described previously, but the polishing with colloidal silica continues for 20 minutes opposed to 2 minutes. This is done to remove as much of the deformed layer as possible. Then more of the deformed layer is removed by electropolishing in 133ml Acetic Acid, 7ml Water and 25g Chromic Trioxide. Continuous stirring of the solution is required to promote even attack. Stirring also prevents bubbles from forming which may cause relief or pitting[88]. The voltage is 10V and the time is 30s. The sample is then carefully broken out of its mounting which is non-conductive and mounted using conductive carbon cement onto a metal stub.

3.5.4.2 Operating Parameters

The accelerating voltage controls the pattern brightness. A higher accelerating voltage gives a brighter diffraction pattern. The electrons penetrate further and this minimises the effects of surface contamination and surface deformation. However, a lower accelerating voltage increases the spatial resolution. An ideal compromise is 25kV.

The working distance is chosen so that the electrons are backscattered towards the phosphor screen. Another practical consideration is the distances inside the chamber. If the working distance is too small the sample might collide with the pole piece. The working distance used was 20mm.

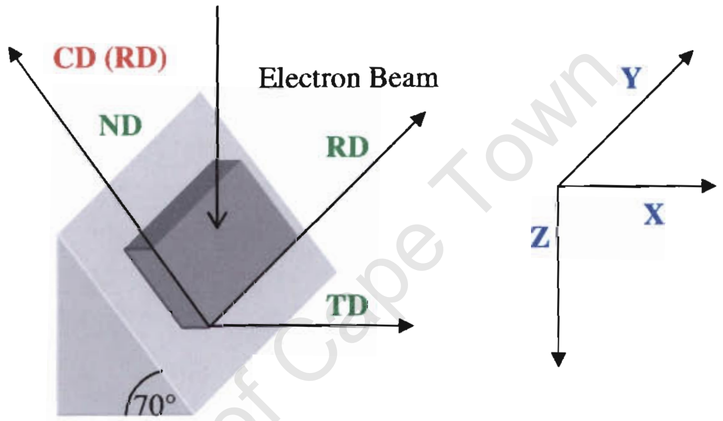

Figure 3-18: Orientation for specimens relative to chamber direction. Green text is the mill samples directions and red is the compression sample directions and blue is the SEM chamber direction.

As the specimen tilt angle of the specimen increases the path length of the backscattered electrons increases which leads to better pattern contrast. Very high angles cause excessive anisotropy and image distortion. A good tilt angle is 70° to the horizontal. This angle can be seen in Figure 3-18.

3.5.4.3 Grain Maps

An automated beam scan was done of the specimen surface which results in a grain map. The beam spacing was 1μm and the map size is 200μm by 200μm for the compressed samples and 100μm by 100μm for the mill samples. Three maps were done per specimen to ensure that an accurate representation of the material was captured.

3.5.4.4 Non Indexed Points

When the pattern quality is too poor to be analysed at a point a non-indexed point may occur. These non-indexed points may be due to artefacts in the microstructure such as inclusions or pits. Another source of non-indexing is where patterns overlap from grains, subgrains, phase boundaries or strongly dislocated structures. If the non-indexing fraction is too large then it may be difficult to glean microstructural information from the sample. If there are a small number of non indexed points then they may be systematically removed by making them the same as their neighbouring pixels. This scenario is shown below:

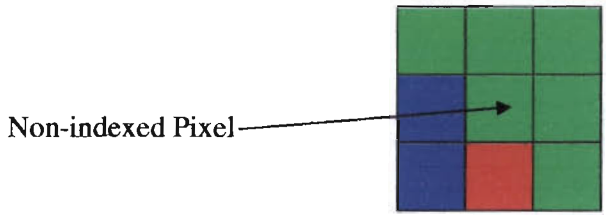

Figure 3-19: Indexing showing five neighbours to index a previously un-indexed pixel.

In VMAP[a] a level 3 cleaning routine is used which is equivalent to using five neighbours to index a pixel.

3.5.4.5 Calculating the Recrystallization Fraction

VMAP software was used to calculate the recrystallization fraction. The fraction is calculated based on the following definition of a recrystallized RX grain[89]:

1. Area which is bounded by a certain fraction of HAGB between 1 and 0
2. Area where pattern quality is some fraction greater than the mean
3. Area that is larger than some multiple of the cells or subgrains

Definition 1 and 3 would depend on the definition of the misorientation angle for a LAGB and a HAGB respectively.

---

[a] VMAP software was written by John Humphries, of the Manchester Materials Science Centre

To make a decision on these parameters a sample that was annealed to full recrystallization was tested and the parameters were chosen to ensure that the fraction recrystallized was close to unity.

The following decisions were then made with respect to the recrystallized grain for the AISI304 stainless steel studied:

1. Bounded by **0.4** HAGB.
2. Pattern quality is **0.7** times greater than the mean.
3. Size is **2** times greater than the subgrain size.

The HAGB and LAGB were defined to have 15 and 1.5 misorientation angle respectively.

CHAPTER 4: RESULTS

4.1 Finite Element Analysis of Through Thickness Deformation Conditions

The results of the finite element study of the mill strip are presented below. The significance of the through thickness variations are evaluated. These variations are in the process parameters: strain, strain rate and temperature (interpass and deformation).

4.1.1 Strain

The assumptions used in developing the Finite Element Model (FEM) presented are detailed in section 3.4.8.1. The strain in the transverse direction is assumed to be zero. The rolling direction strain per pass can be seen in the table below. M1 is an element in the mid plane and M9 is an element on the surface.

Table 4-1: Strains per pass in rolling direction through thickness.

Pass Number	M1	M2	M3	M4	M5	M6	M7	M8	M9
1	0.32	0.32	0.32	0.32	0.32	0.32	0.32	0.33	0.33
2	0.31	0.31	0.31	0.31	0.31	0.31	0.31	0.31	0.32
3	0.30	0.30	0.30	0.31	0.31	0.31	0.31	0.30	0.31
4	0.23	0.23	0.23	0.23	0.23	0.24	0.24	0.24	0.24
5	0.17	0.17	0.17	0.17	0.17	0.18	0.18	0.18	0.18

From the Table 4-1 it can be seen that the strains do not differ significantly from the mid plane to the surface. There is a slight decrease of no more than 5%, from the surface to the mid plane of the mill strip.

The green highlighted elements in Table 4-1 are presented in Figure 4-1 and Figure 4-2. The figures represent the changes in the rolling direction strain with time. Elements are presented for the first pass at the mid plane and at the surface.

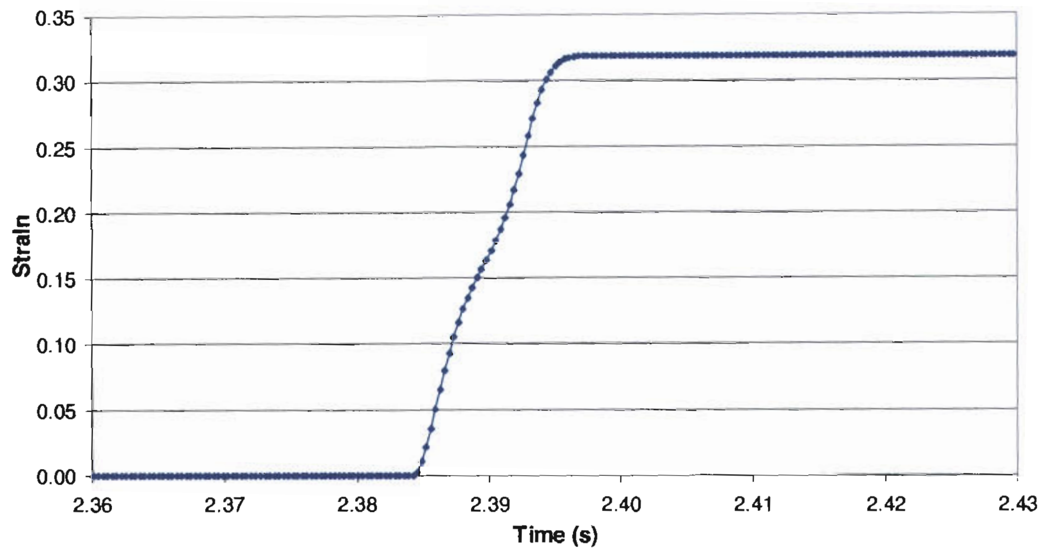

Figure 4-1: The rolling direction strain at the mid plane and as it moves through the roll gap during the first pass.

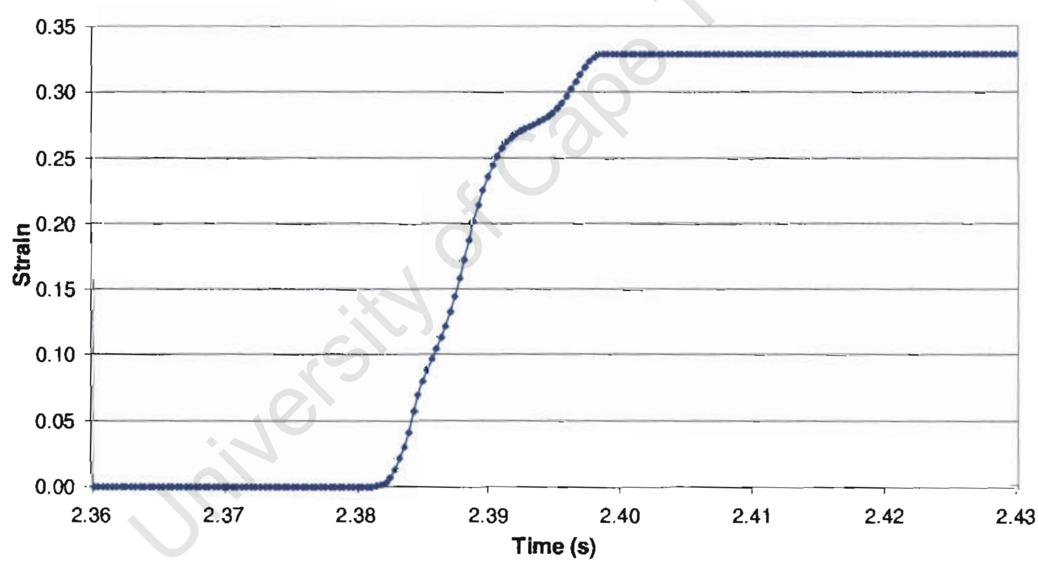

Figure 4-2: Same presentation as Figure 4-1 but at the surface of the strip for the first pass.

From the two figures above the straining can be seen to have occurred over a longer time at the surface than at the mid plane.

4.1.2 Strain Rate

Strain rates were calculated as the slope of the straight line through the strain over the deformation period (for example Figure 4-1 and Figure 4-2).

Table 4-2: Strain rate(s^{-1}) per pass for each through thickness element.

Pass Number	M1	M2	M3	M4	M5	M6	M7	M8	M9
1	28	28	28	28	29	29	28	28	24
2	35	35	34	33	33	32	30	28	28
3	72	74	74	77	80	81	81	80	55
4	103	103	101	99	97	95	91	86	79
5	60	60	59	58	57	56	54	51	46

As can be seen in Table 4-2, the strain rates are a little lower at the surface even though the strains are slightly higher. This is due to deformation occurring over a longer period at the surface. The strain rates are not significantly different from the mid plane to the surface. The changes in the strain rate from pass to pass are due to changes in the roll speed.

4.1.3 Temperature

The FEM output of the temperature during the first roll pass is presented below. In the model the temperature profile of the strip is made homogenous after each pass. As in section 4.1.1 the temperature change per unit time will be shown for the surface and the mid plane on the first pass.

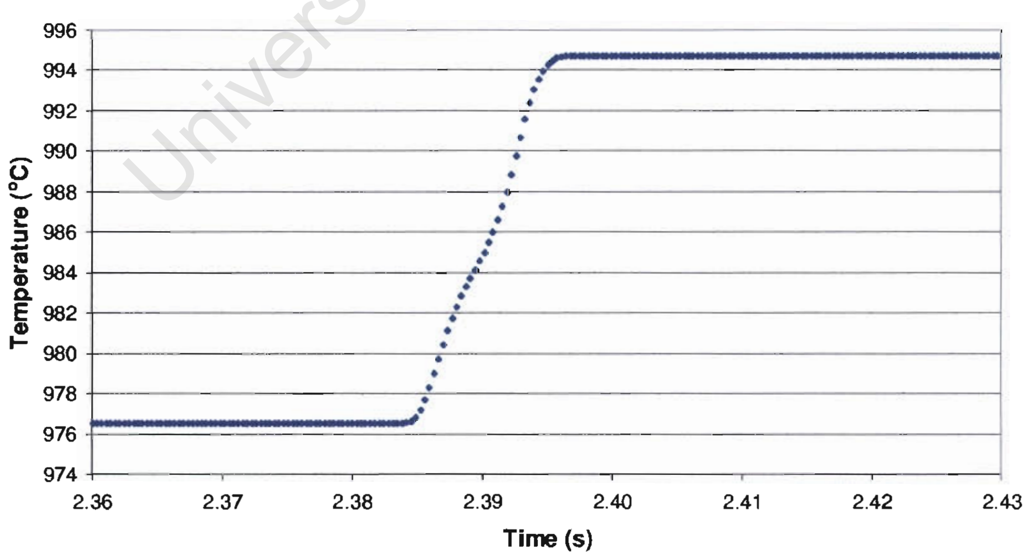

Figure 4-3: Temperature through the roll gap at the mid plane of the strip in the first pass.

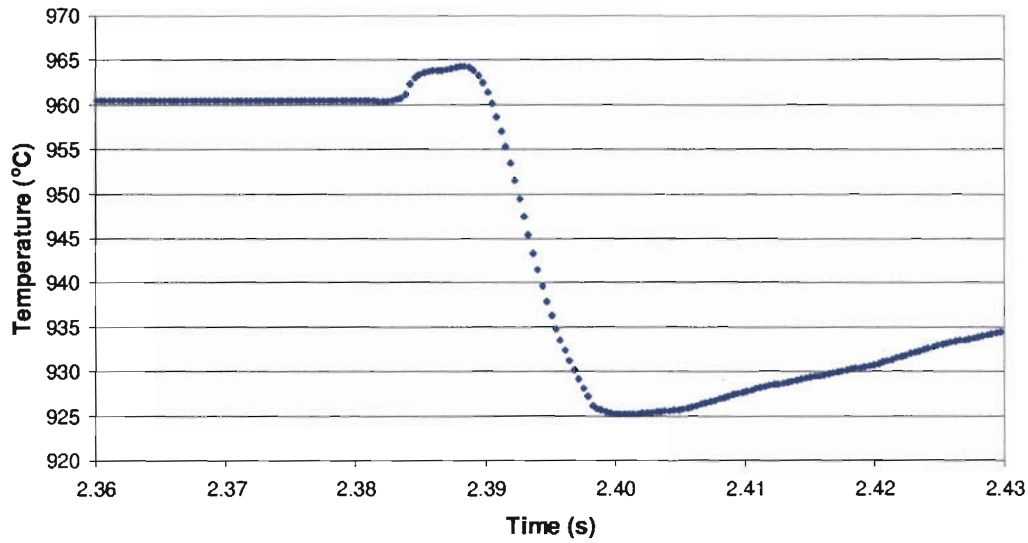

Figure 4-4: Temperature through the roll gap at the surface of the strip in the first pass.

The temperature increases at the surface and mid plane are due to deformation by the work rolls (adiabatic heating). A decrease in temperature is observed at the surface as shown in Figure 4-4. This is due to heat conduction to the work rolls. The steady state increase is due to heat conducted from mid plane to the surface to equalise the temperatures. The average deformation temperature over the deformation period is presented in Table 4-3, below:

Table 4-3: Average deformation temperatures (°C).

Pass Number	M1	M2	M3	M4	M5	M6	M7	M8	M9
1	986	986	985	984	983	982	979	976	953
2	980	980	980	980	980	980	979	977	936
3	990	990	990	990	990	989	989	986	951
4	982	982	982	982	982	982	982	981	963
5	925	924	924	924	924	924	923	922	911

The gradual decrease in temperature is observed with pass step is due to the increase in surface area per unit volume of the mill strip. Therefore the increased contact with the colder air allows more heat conduction. The surface element M9 is also the coldest region on the strip since it is the only region directly exposed to the air.

The interpass temperatures experienced after the actual deformation event are shown below in Table 4-4. These interpass temperatures are average temperatures after the deformation events until the temperature is reset.

Table 4-4: Average interpass temperatures (°C).

Pass Number	M1	M2	M3	M4	M5	M6	M7	M8	M9
1	978	978	978	978	978	977	977	976	976
2	950	950	950	950	950	950	949	949	949
3	981	981	981	981	981	981	981	981	981
4	977	977	977	977	976	976	976	976	976
5	922	922	921	921	920	920	919	918	916

The interpass temperatures are generally lower than the deformation temperatures. The drop from M9 to M8 in the deformation temperatures is not seen in the annealing temperatures.

4.2 Mill Sample Microstructural Analysis

Mill samples were cut from various areas of the mill strip and analysed for variations in the normal and transverse direction, as well as variations between the head, tail and middle section. The through thickness variations examined in this section will serve as a validation of the finite element results in the previous section.

These samples were not quenched as would happen in a controlled laboratory experiment. The samples were air cooled for an unknown time after the last pass and various restoration events could have occurred over this period. The mill logs describing the deformation conditions are given in Appendix A.

The montage of micrographs of the tail section from the surface to mid plane is shown in Figure 4-5 to illustrate microstructural variations through thickness. Areas on the surface and the mid plane were magnified further to clarify the microstructure. The etchant used was oxalic acid and is described in section 3.5.1.

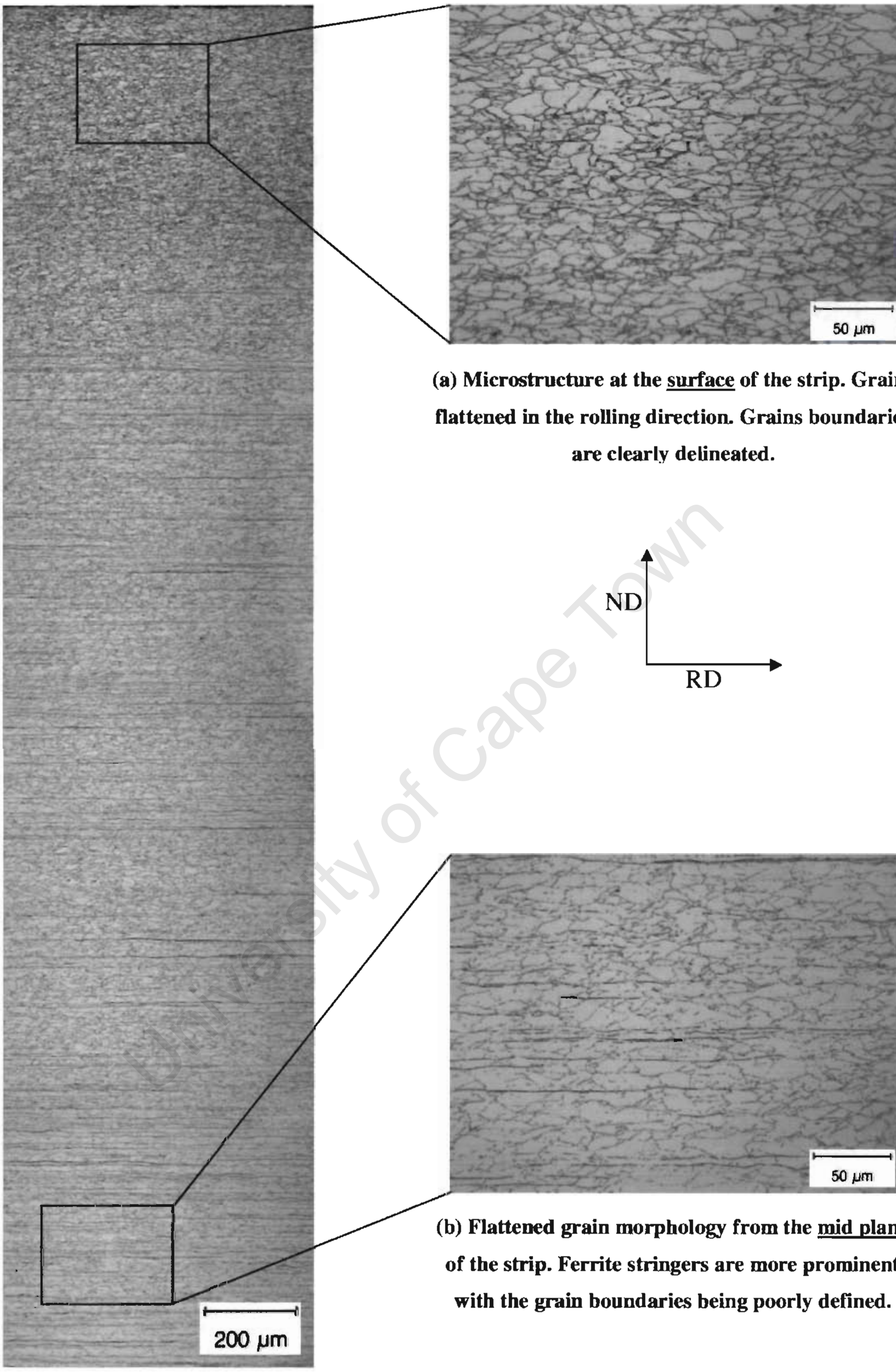

(a) Microstructure at the surface of the strip. Grains flattened in the rolling direction. Grains boundaries are clearly delineated.

(b) Flattened grain morphology from the mid plane of the strip. Ferrite stringers are more prominent with the grain boundaries being poorly defined.

Figure 4-5: Montage of micrographs showing variation in microstructure in the tail section of the strip. Sections are magnified for clarity from the surface (top) and the mid plane (bottom). Only half the strip is presented due to symmetry through the mid plane.

The grains in the surface and the mid plane have roughly the same flattened grain morphology. The grains are less distinctive in the mid plane than at the surface. There is a complete absence of annealing twins, even though oxalic acid etchant is used which preferentially attacks these twins.

The hardness results are presented for the head and tail section of the sample in Figure 4-6. The variations in hardness in the rolling direction as well as the transverse direction are studied.

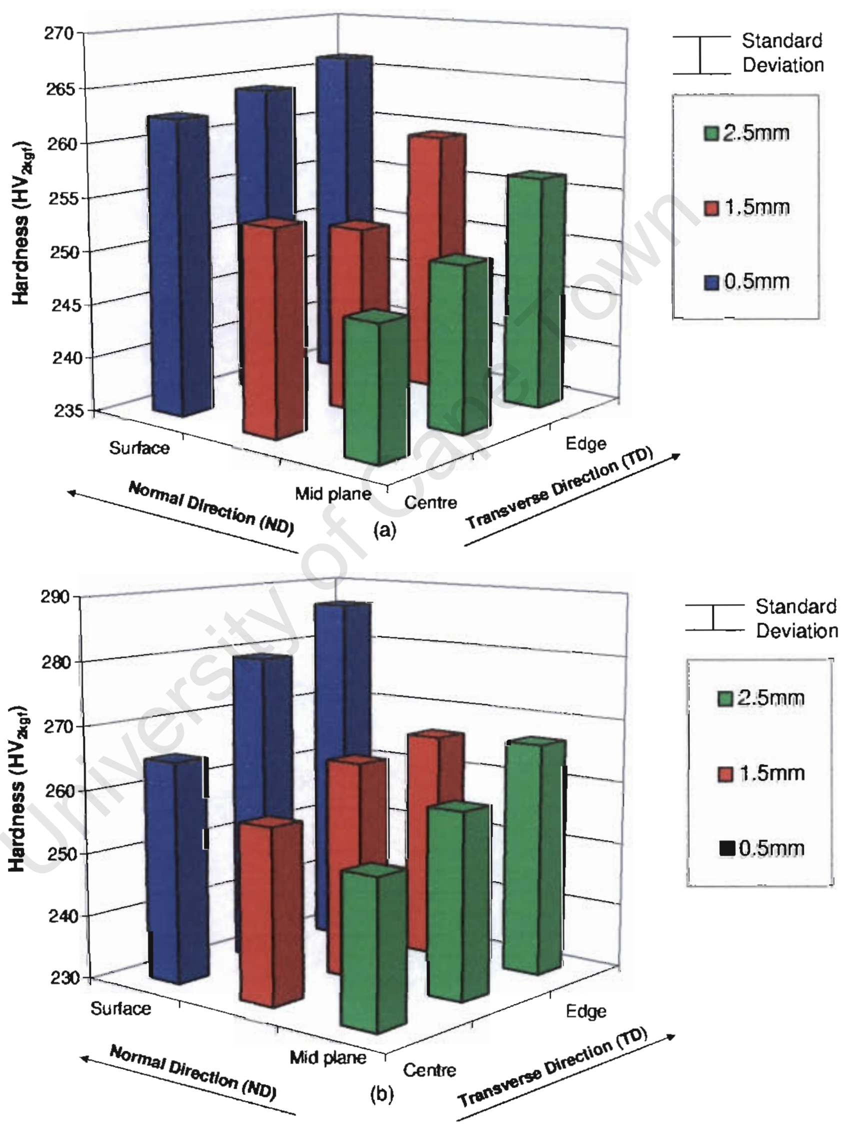

Figure 4-6: Hardness variation at the end sections of the strip, showing head section in (a) and tail section in (b). Each bar represents an average of three readings. The legend indicates the distance in the normal direction from the surface. The standard deviation indicated is 4 HV and is an average of all the deviations in all the mill strip hardness values.

Hardness variations are seen in all directions. Note that the hardness axis range is larger in (b) than in (a). The tail section can be seen to be harder than the head section. In both samples the hardness is greatest on the edge surface and lowest in the centre of the mid plane. The three dimensional setup of the graph accentuates and highlights any differences between the hardness measurements. The change is roughly a 10% change from the smallest to the highest reading in the head and tail section.

The next series of micrographs shows the middle section which can be compared to tail section of the strip in Figure 4-5 which was etched under the same conditions in oxalic acid.

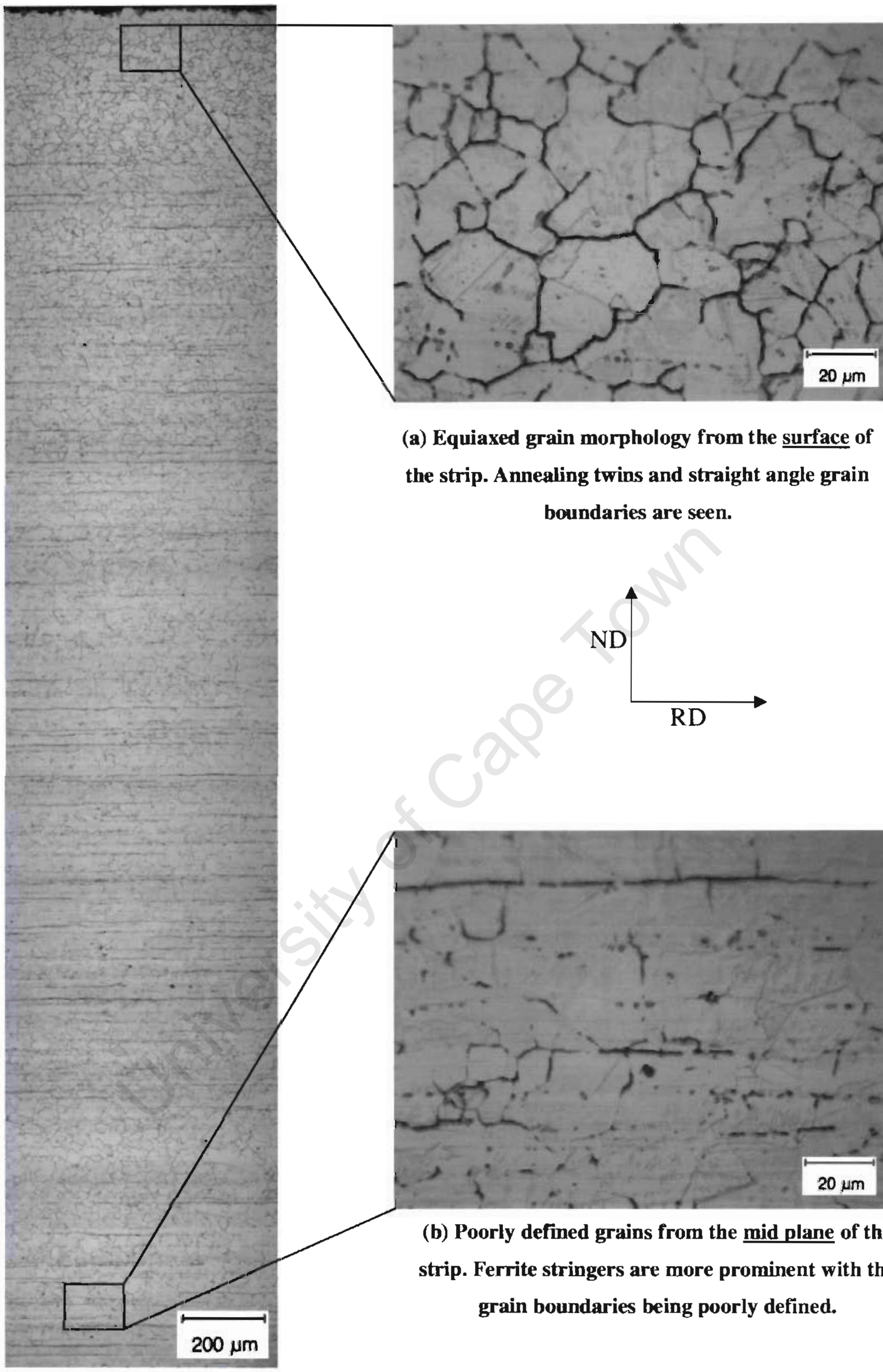

(a) Equiaxed grain morphology from the <u>surface</u> of the strip. Annealing twins and straight angle grain boundaries are seen.

(b) Poorly defined grains from the <u>mid plane</u> of the strip. Ferrite stringers are more prominent with the grain boundaries being poorly defined.

Figure 4-7: Montage of micrographs from the middle section. Same presentation as Figure 4-5.

A contrast is seen between the tail section and the middle section. The middle section has equiaxed grains in contrast to the pancake shaped grains of the tail section. A similarity between the sections is the poor grain definition in the mid plane of the sample with a stronger grain definition at the surface of the strip.

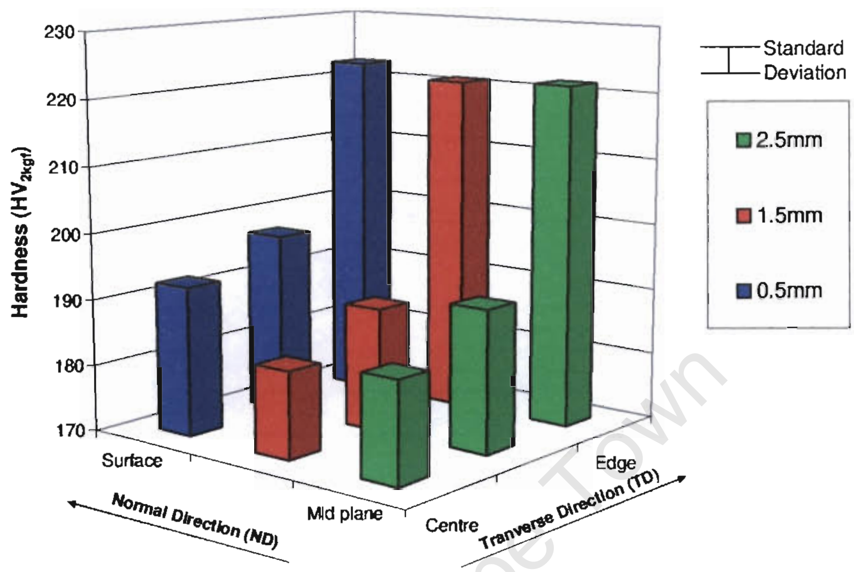

Figure 4-8: Material from the middle section of the strip. Same presentation as Figure 4-6.

To summarise Figure 4-6 and Figure 4-8 the average hardness in each section is given in Table 4-5, below.

Table 4-5: Average hardness in each section of the strip.

Head Section	Middle Section	Tail Section
260HV	200HV	270HV

The hardness in the middle section is significantly lower than the ends of the strip. The hardness on the surface of the strip is similar to the mid plane of the strip. The hardness is greater on the edge of the strip than in the centre.

EBSD was performed on the samples to show the recrystallized fraction of the samples. It was not possible on the ends or the outside of the middle section due to their deformed nature. Therefore EBSD was done on the centre of the middle section:

Table 4-6: Recrystallization Fraction in middle section of strip.

Area	Recrystallization Fraction
Surface	0.96
Mid plane	0.92

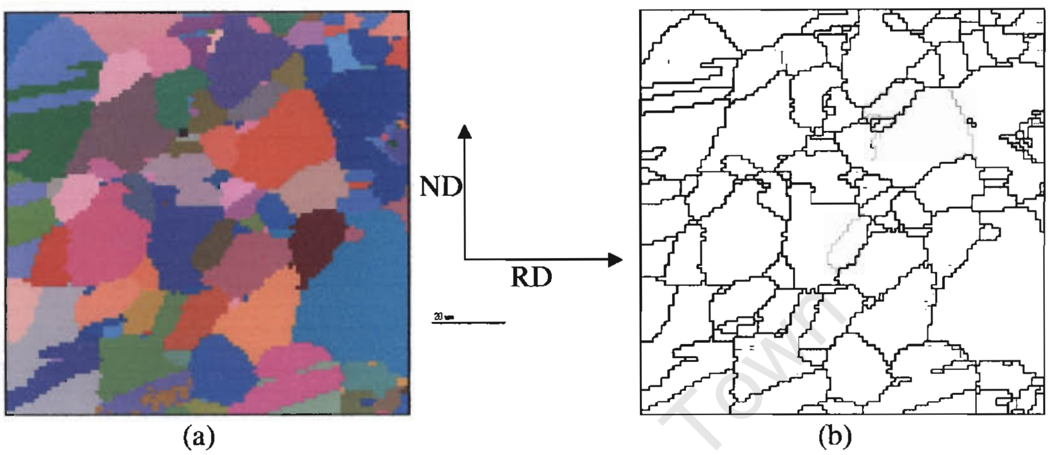

Figure 4-9: Grain maps of middle section showing level of recrystallization. In (b) low angle grain boundaries are grey and high angle grain boundaries are black.

The paucity of LAGB is noted in Figure 4-9. The relatively equiaxed grain structure is also noted. This is expected for a recrystallized grain structure. The equiaxed microstructure can also be seen in the optical micrographs as well shown in Figure 4-7.

4.3 Mill Log Analysis

The through thickness variations were seen to be relatively small in the context of the hot rolling process. The parameters are then assumed to be uniform through thickness. A detailed analysis was done of the mill logs to aid in assessing the microstructural evolution in the mill strip during the rolling process. Two different sets of mill logs will be presented and the details are given in Table 4-7.

Table 4-7: Details of mill logs presented.

Designation	Number of Passes	Number of Heats
L1	5	5
L2	7	8

A heat refers to the rolling schedule of one strip. The average of the heats is presented in this section. The raw data is given in Appendix A.

The labels L1 – L2 describe the different rolling schedules for each set of heats.

4.3.1 Interpass times

The interpass times are how much time each section of the strip has to restore between deformation events. The values are calculated as per section 3.4.5.

Table 4-8: Interpass time(s) for middle, head and tail section for L1 calculated from average values in Appendix A.

Pass Numbers	1-2	2-3	3-4	4-5
Middle	43	50	56	64
Head	80	6	103	6
Tail	6	91	6	121

In the above table we note that after deformation in the first pass the middle section will have 43s to restore before deformation in the second pass. As can be seen from the Table 4-8 the middle section has a relatively large amount of time to recrystallize from 43s to 64s. From the first pass to the second pass the head would have 80s to restore whereas the tail would have 6s to restore. In the short time of 6s the tail section is unlikely to have restored and strain is likely to accumulate. The opposite is true for the head section that is likely to restore completely. The strain accumulation in the tail section and not the head section indicates that the tail section would have the highest mean flow stress (MFS) on the second pass. Following the same logic the head and tail would alternate to provide the highest MFS in the strip.

4.3.2 Mean Flow Stress

The results of the MFS analysis are presented in this section. The MFS values are calculated using Equation 3-10 and explained in section 3.4.1.1.

In Figure 4-10, below, the MFS for a 5 pass schedule for L1 is contrasted to a 7 pass schedule for L2.

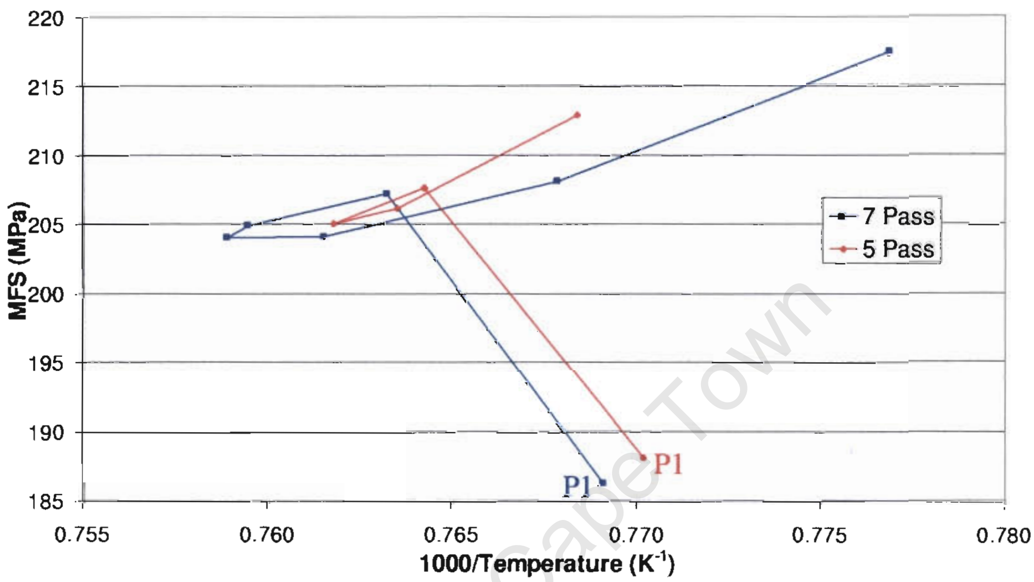

Figure 4-10: Average middle section MFS for five and seven pass schedules as related to inverse temperature. These are plotted for mill logs L1 and L2. The MFS for pass 1 is represented by the label P1. The lines are drawn in to indicate the sequence of the passes and the change in slope between passes.

A large increase from pass one to pass two, followed by passes where the stress values are at the same level and then an increase in the last few passes is seen in both curves in Figure 4-10. The seven pass graph increases to a larger extent than the five pass graph. The stress axis range is relatively small and only increases 35MPa from 185MPa to 220MPa. Another observation is that even though temperature is increasing from pass 1 to pass 2, the MFS increases.

In Figure 4-11 the predicted steady state stress and strain per pass is presented on the same axis as the MFS to attempt to account for the changes or to at least to distinguish which factors have an influence on the MFS. An increase in the steady state stress indicates that either the temperature is decreasing and/or the strain rate is increasing.

The strain is calculated as per Equation 3-16 and Equation 3-17. The steady state stress was calculated from Equation 3-22 and using constants from Smal et al[24]. Smal's results were from the same type of stainless steel from the same mill as used in this study. The strain rate was calculated from Equation 3-19 and Equation 3-20 for use in the steady state equation. The absolute value of the steady state stress is not of great importance but the relative change from one pass to another is of interest. The steady state stress is a compact way of capturing temperature and strain rate in one variable.

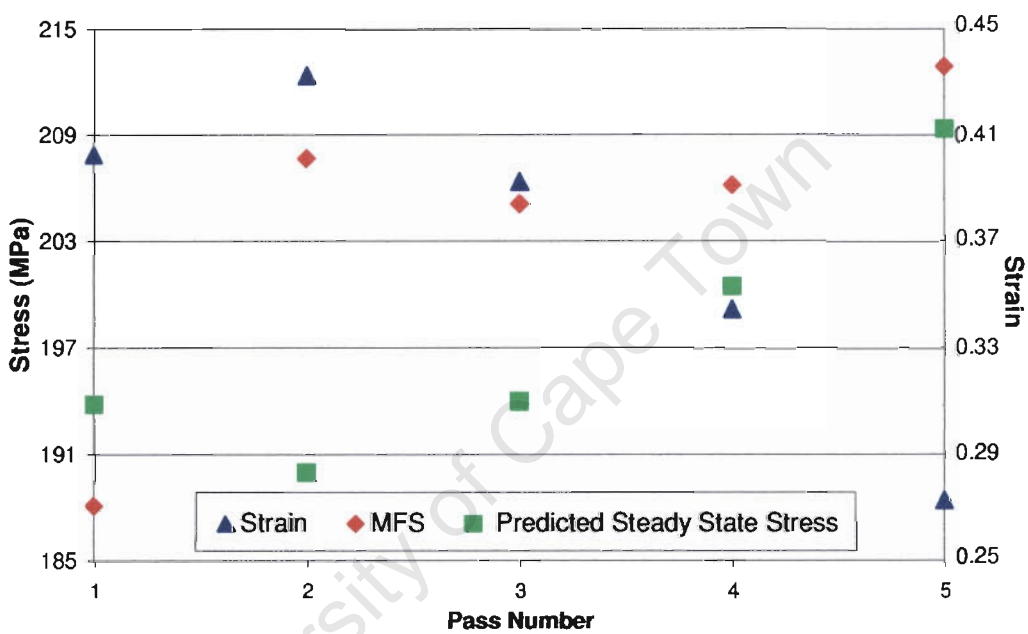

Figure 4-11: Relation of calculated steady state stress and strain to MFS for the middle section for L1. These comparisons are per pass.

The relationships between variables are shown above. Similar to Figure 4-10 the range of stress values is quite small, only 30 MPa. The steady state stress increases from the second pass to the last pass. The strain demonstrates opposite behaviour and decreases from the second pass to the last pass.

The maximum steady state stress is compared to the maximum MFS in contrast with the MFS for the middle section for mill log L1 in Figure 4-12. The maximum MFS can correspond to the head section or the tail section depending on which pass. In section 4.3.1 explanations are given of which pass corresponds to the highest MFS besides the first pass. The tail section in the first pass demonstrates the lowest temperature (see Figure 3-12 on page 49). This means that it will then have the highest MFS.

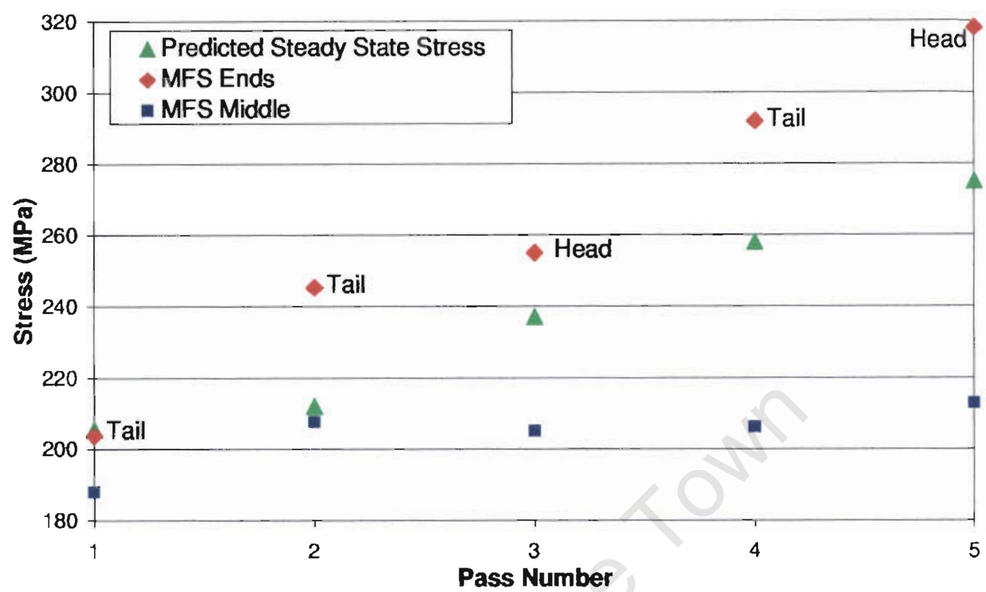

Figure 4-12: MFS middle and ends compared to minimum steady state stress.

In the end section, a very large increase in the MFS is seen from at least 200MPa to nearly 320MPa. This increase is very large compared to the narrow range of values experienced by the middle section. The MFS and the steady state stress can be seen to increase from the first to the last pass. The change in the MFS is greater than the changes in the steady state stress.

4.4 Axisymmetric Uniaxial Compression

The results of the uniaxial compression tests are presented in Figure 4-13. The effects of the process parameters such as strain, strain rate and temperature on the MFS and the resulting microstructure are evaluated. These are compared to the MFS from the mill logs and the mill sample microstructure. The decision to test at these temperatures and strain rates is described in the section 3.2.4 and is based on the mill logs.

4.4.1 Temperature Effects at a Strain Rate of $60s^{-1}$

The flow stress is plotted at temperatures between 900°C and 1050°C at a strain rate of $60s^{-1}$. This is described in Table 3-4.

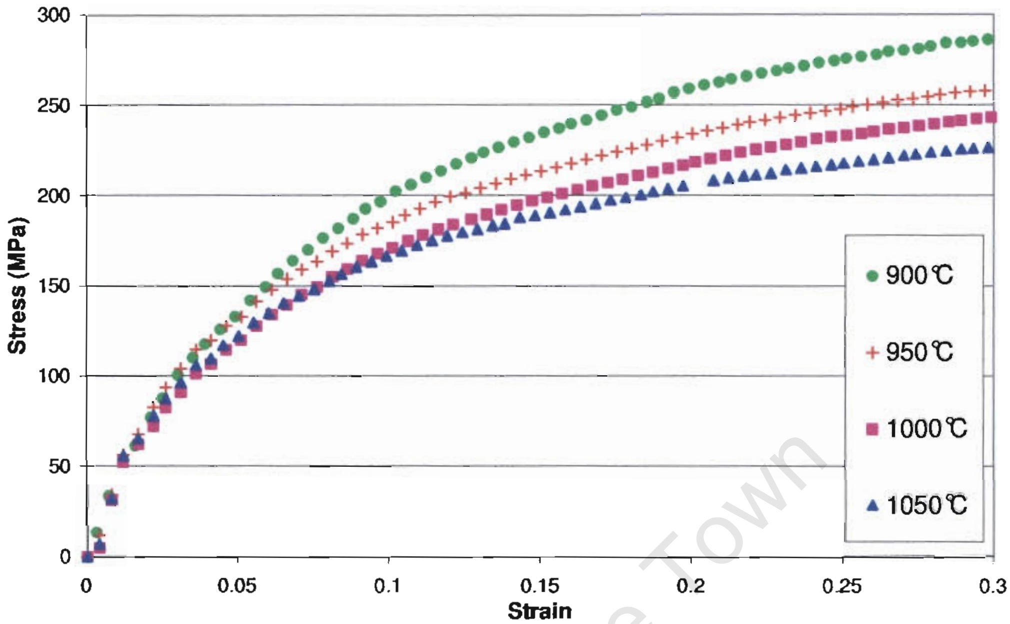

Figure 4-13: Flow stress at $60s^{-1}$ showing the effects of temperature.

As can be seen in Figure 4-13 above increasing the deformation temperature decreases the flow stress. The decrease in flow stress with an increase in temperature is due to thermally induced restoration such as recovery and recrystallization.

The microstructural change of the uniaxial compression sample with an increase in deformation temperature is presented in Figure 4-14. In Figure 4-15 the hardness of the quenched material after deformation at the above parameters is given. Nine readings were taken for each measurement and the sampling procedure is described in section 3.5.3.1. The change in hardness and microstructure with deformation temperature at a fixed strain rate of 60^{-1} is presented here.

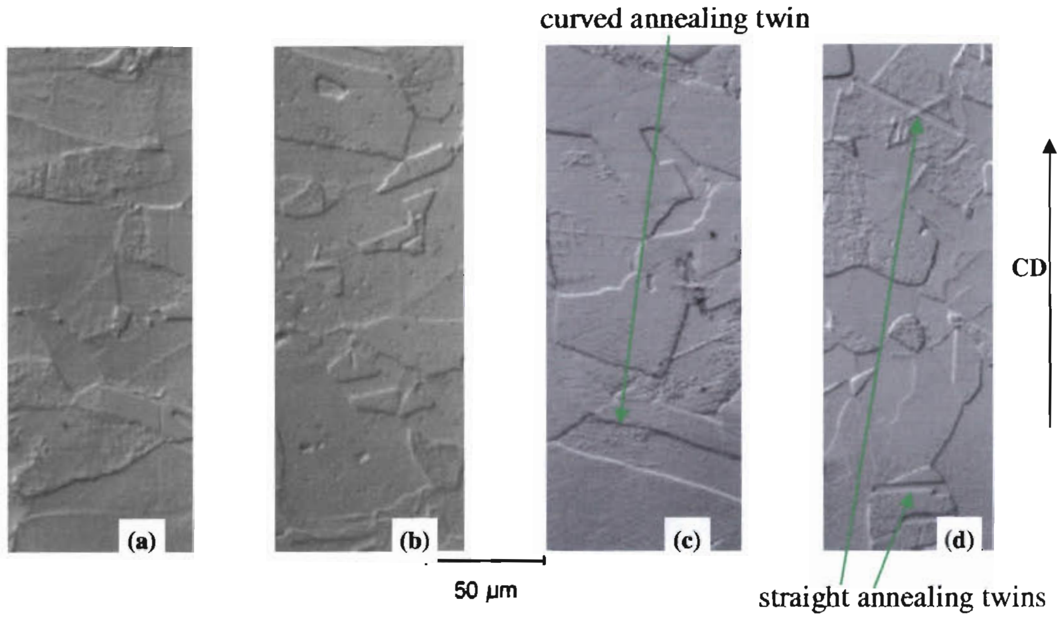

Figure 4-14: Change in microstructure of the uniaxial compression specimen. Deformation conditions are 60s^{-1} and 0.3 strain for all micrographs. Oxalic acid etchant was used. Temperatures are as follows: (a) 900°C; (b) 950°C; (c) 1000°C; (d) 1050°C Note the compression direction (CD) is indicated.

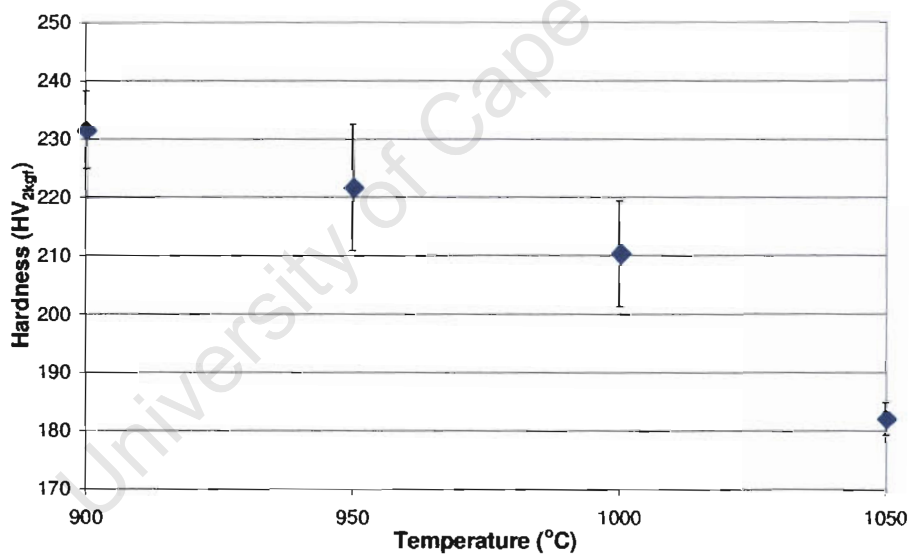

Figure 4-15: Hardness values of specimens deformed with strain rate 60s^{-1} and 0.3 strain at varying temperatures. Error bars indicate standard deviation.

The annealing twins are not seen at the lower temperatures in Figure 4-14. The grain boundaries become straighter with the increasing temperature. Annealing twins are also seen at the higher temperatures. This demonstrates clear evidence of recrystallization.

In Figure 4-13 is repeated in Figure 4-15, an increased resistance to dislocation movement with a decrease in temperature. This increased resistance may be measured by an increase in hardness or an increase in flow stress.

For the conditions and material as in Figure 4-14, a different etchant, Nitric Acid is used which preferentially attacks grain boundaries. The grains size can therefore be ascertained. The grain size is then quantified in Figure 4-17. The Heyn intercept method which is described in section 3.5.2. was used.

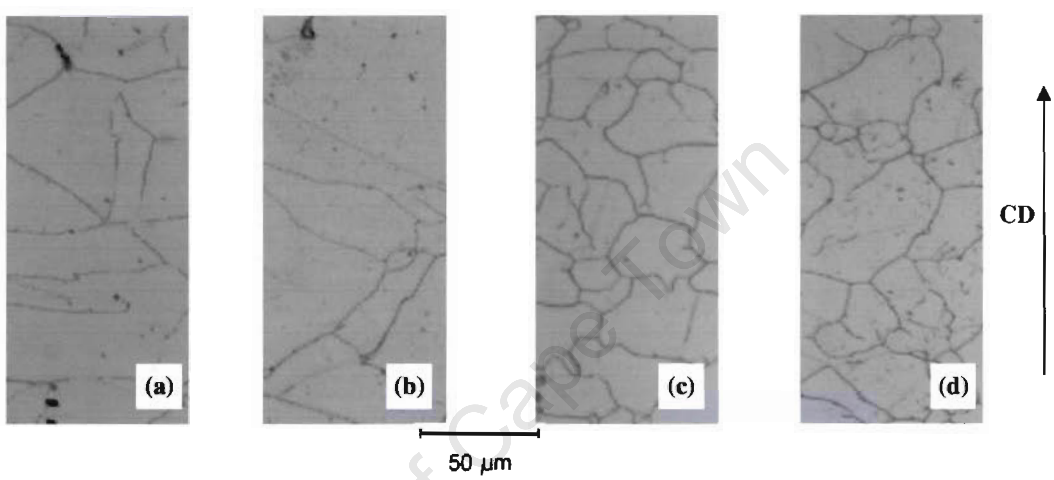

Figure 4-16: Micrographs was of the same specimen as Figure 4-14 but a different etchant of 60% nitric acid - 40% water was used. Temperatures are as follows: (a) 900°C; (b) 950°C; (c) 1000°C; (d) 1050°C and corresponds to the figure below.

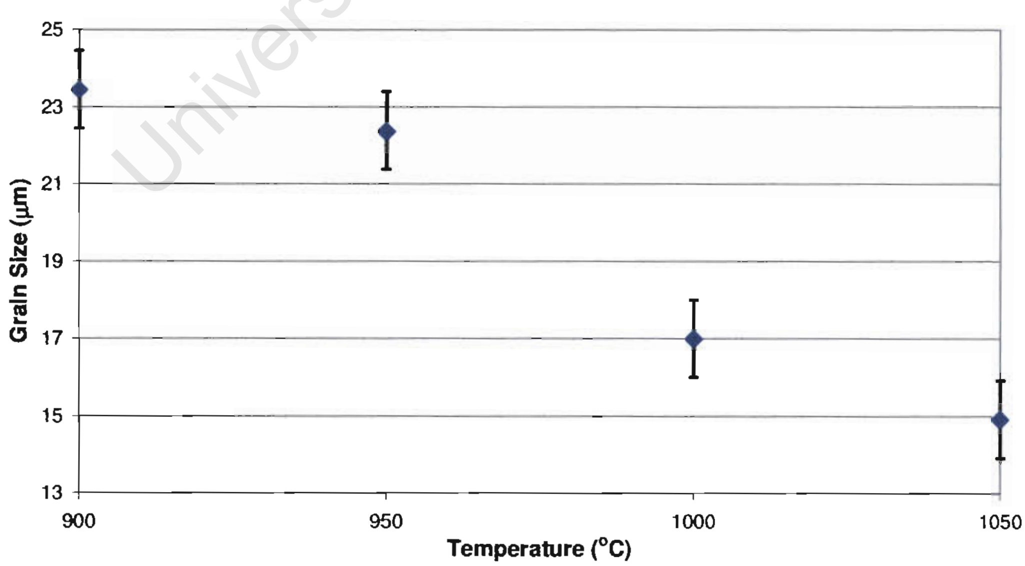

Figure 4-17: Grain size measurements as a function of temperature at 0.3 strain and $60s^{-1}$. Error bars indicate standard deviations that are the same for all the grain size measurements.

The contrasting microstructure between Figure 4-14 and Figure 4-16 can be seen. Grain refinement can be seen with an increase in temperature and is quantified in Figure 4-17 with the method of calculation explained in section 3.5.2.

4.4.2 Strain Rate Effects at 1000°C

In the figure below the deformation temperature is fixed and the effect of strain rate on the MFS at the strain rates experienced in hot rolling from $120s^{-1}$ to $30s^{-1}$ is presented.

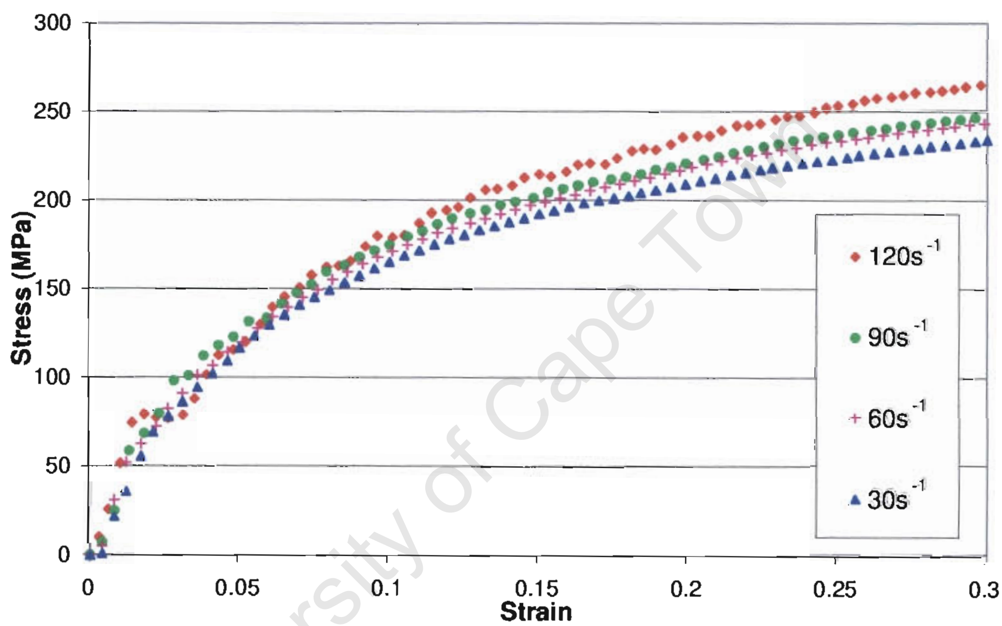

Figure 4-18: Flow stress at 1000°C showing effects of strain rate as indicated in the legend.

As seen in Figure 4-18 an increase in flow stress is seen as is expected with increase in strain rate. The increase is less than the temperature related increase in flow stress (see Figure 4-13). As in the previous section the as-quenched hardness of the deformed specimen is measured and the results are presented below.

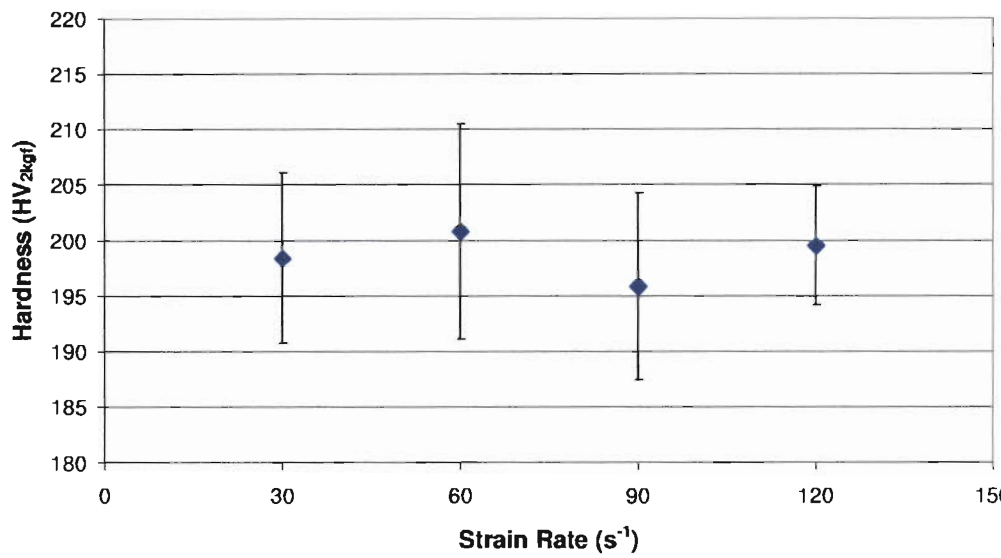

Figure 4-19: Variation in hardness with strain rate, Deformed at 1000°C to 0.3 strain. Error bars indicate standard deviation.

The increase in flow stress with strain rate is not observed in the hardness tests as seen in Figure 4-19. The standard deviation in the hardness testing is greater than any discernable upward trend. The hardness is insensitive to strain rate in the range tested.

4.4.3 Double Hit Temperature Effects

The results of the double compression or double hit tests are presented below as detailed in Table 3-5, section 3.2.4. The specimens are held at temperature, then compressed and then held for 60s before being compressed again at the same temperature. The MFS of the first hit and the second hit are compared with varying temperature.

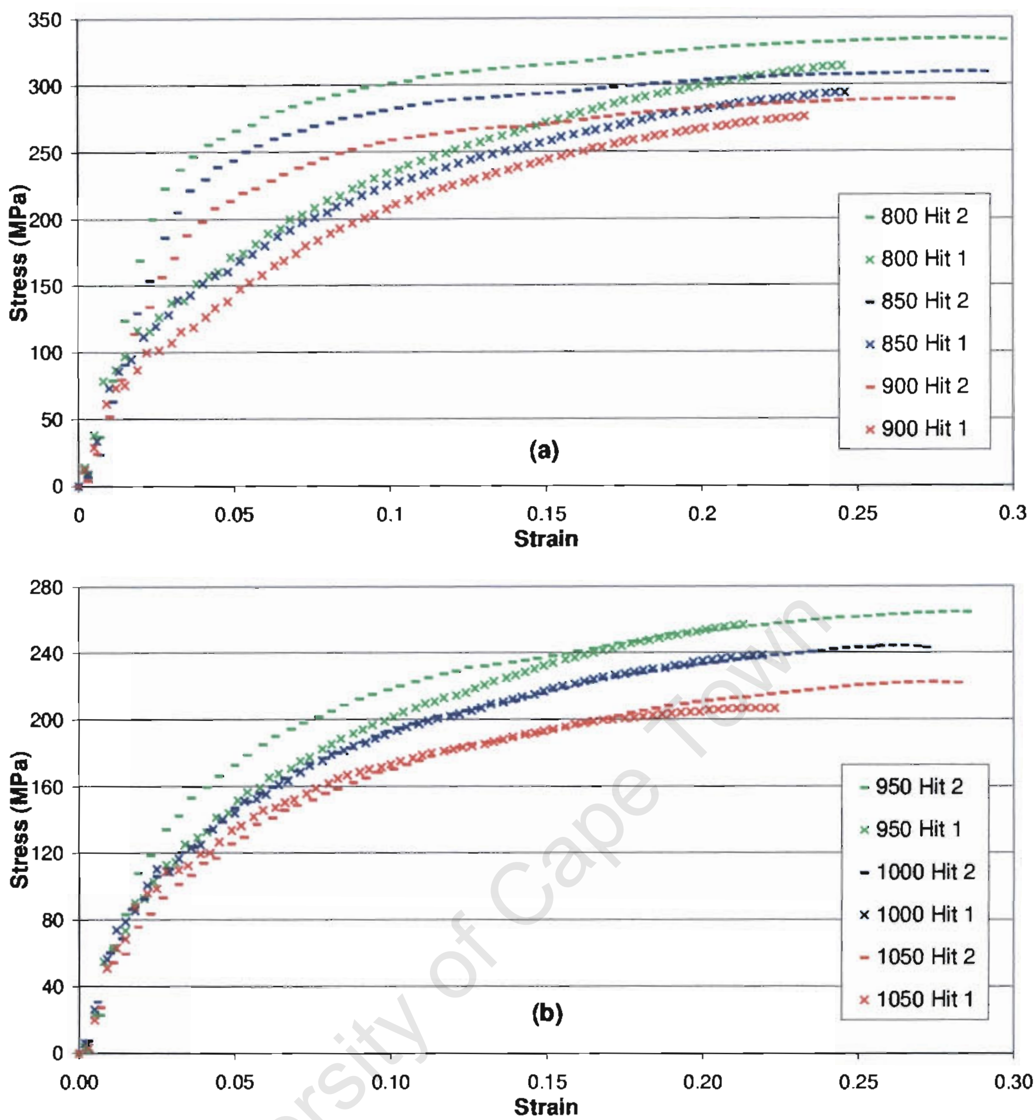

Figure 4-20: All flow stress curves deformed at 60s^{-1} at the various temperatures. Hit 1 indicates the flow stress during the first deformation event and Hit 2 during the second deformation event. The temperature(°C) is given in the legend.

In Figure 4-20 (b), for 1050°C and 1000°C the Hit 1 and Hit 2 are virtually identical. This indicates that full restoration of properties between passes has occurred. From 950°C to 800°C, the flow stress increases in a marked fashion between passes which indicates strain accumulation.

The as-quenched hardness and microstructure from these compression tests are presented in Figure 4-21. The double hit hardness is compared to the single hit hardness with changes in temperature.

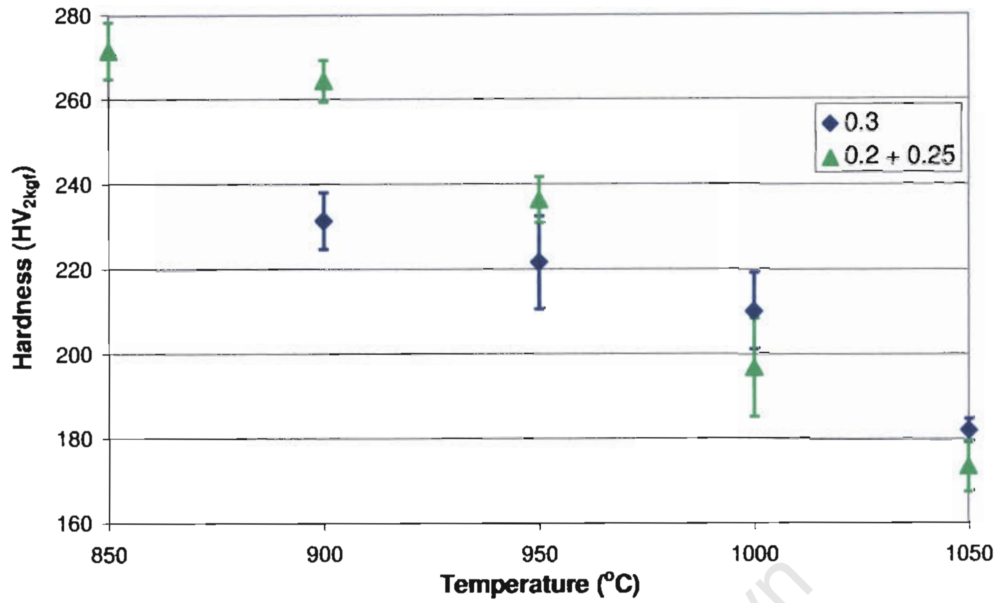

Figure 4-21: Hardness as function of temperature. Results are plotted for single hit (strain = 0.3) and double hit (strain = 0.2 + 0.25). Error bars indicate standard deviation.

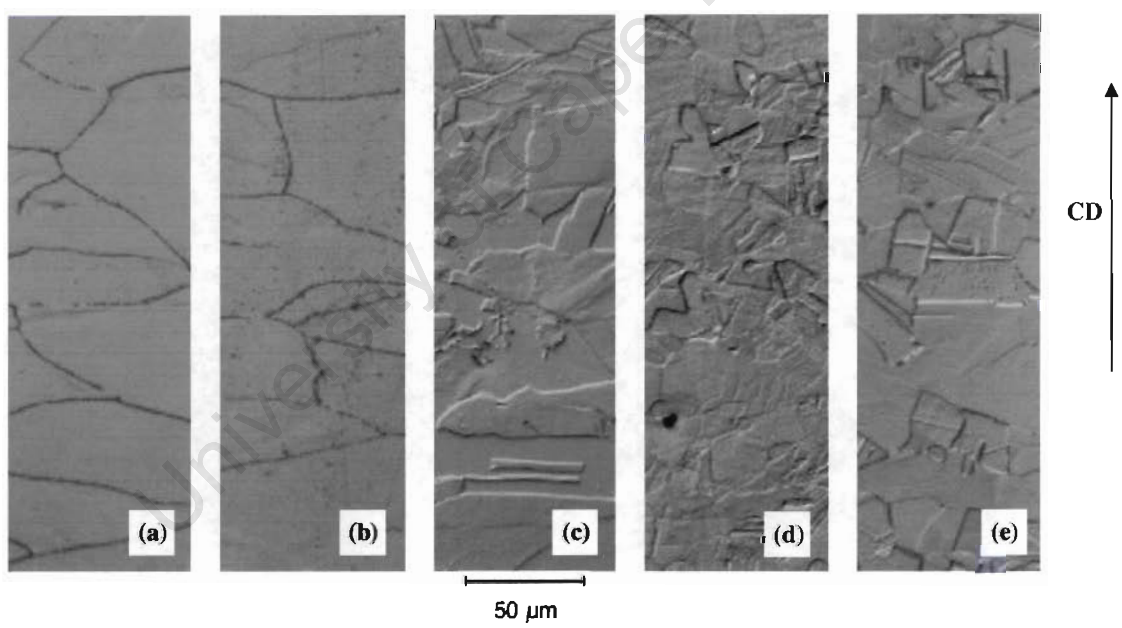

Figure 4-22: Double hit micrographs where the strain is first 0.2 and then 0.25 at a strain rate of $60s^{-1}$. The etchant is oxalic acid and the etch time is 15 seconds. Temperatures are as follows: (a) 850°C; (b) 900°C; (c) 950°C; (d) 1000°C; (e) 1050°C.

As can be seen in Figure 4-21, above at temperatures of 950°C and below the double hit hardness is greater than the single hit hardness. This indicates effective strain accumulated between the hits is greater than 0.3. At 1000°C the double hit hardness is lower indicating that restoration has occurred between hits and the cumulative strain is lower than that for a single hit event. The large change in restoration rate is again observed from above 950°C.

As can be seen in Figure 4-22 the grain boundaries are straighter at higher temperatures. At 900°C and 850°C a distinct difference in etch behaviour is seen. The annealing twins are not revealed. The grains are also flattened in the compression axis direction at the lower temperatures.

4.5 Characterisation of Post-Deformation Softening

Heat treatments were done on the deformed uniaxial compression samples. The results of these heat treatments were analysed by two different methods. The first method is to deform the sample again after the heat treatment and compare the yield stress from the first and second deformation. The second method is to study the changes in hardness with the heat treatment time. Both these methods are described in section 3.3.

4.5.1 Restoration of Yield Stress

The restoration of yield stress (FS) is plotted in Figure 4-23 using Equation 3-2 in section 3.3.1. The yield stress values were taken from Figure 4-20.

In Figure 4-28 the strain rate change can be seen to have a minimal effect on the restoration. The temperature effect is much stronger. The effects of restoration are clearest at the higher temperatures as seen in Figure 4-29. The straight grain boundaries can be clearly seen in the final microstructures.

4.5.3 Determining Time to 50% Recrystallization

To calculate Avrami constants and $t_{0.5}$ equation constants the fraction recrystallized (X_{srx}) has to be calculated. This is done for the samples deformed to the same strain and strain rate. In this study, X_{srx} is calculated for the specimens deformed at 0.3 strain and $60s^{-1}$ strain rate.

The calculation of the X_{srx} value requires the determination of the fully recrystallized hardness (h_f) (see section 3.3.2). No levelling off was seen on samples deformed at 900°C in Figure 4-26 and at 950°C in Figure 4-28 and there were insufficient samples to continue with the annealing treatments so the h_f could not be evaluated directly from the hardness data. The value of h_f would have to be evaluated in some other fashion. The X_{srx} could first be determined for some instantaneous measured hardness (h) and rearranging Equation 3-3 the h_f value could then be calculated. Electron backscatter diffraction (EBSD) was done to ascertain this X_{srx} value. The results of the EBSD are presented in Table 4-9, below. A set of three maps were done of 200μm by 200μm.

Table 4-9: Results of EBSD fraction recrystallized analysis.

Number	Temperature	Annealing Time	Average X_{srx}
1	900°C	240s	1.0
2	950°C	120s	1.0

Both samples are seen to be fully recrystallized at the final annealing times of 240s and 120s for 900°C and 950°C respectively. Consequently the h values measured at these temperatures were then deemed to be the h_f. Using the h_f, the X_{srx} may be determined. The X_{srx} for 900°C, 950°C and 1000°C as a function of annealing time is presented in the following figure.

The activation energy in hot working (Q_{def}) is 434kJ.mol^{-1} from Smal et al. His work was based on stainless steel from the same mill as the present study. From the values then calculated from the equation defining the straight line in Figure 4-32 , A in Equation 3-7 is 6×10^{-16} and the activation energy for recrystallization (Q_{srx}) is 478kJ.mol^{-1}.

The full equation is then

$$t_{0.5} = 6\times10^{-16}\varepsilon^{-2}D_o^2Z^{-0.375}\exp\left[\frac{478000}{RT}\right]$$

Equation 4-1

This result compares favourably with the results from literature as seen in Table 2-3 despite the limited data as presented in Figure 4-32.

CHAPTER 5: DISCUSSION

5.1 Mill Strip Analysis

The finite element analysis of the mill strip in conjunction with the microstructural analysis is considered in this section. Due discretion is required in analysing the mill samples since they are not quenched as is mentioned in section 4.2.

5.1.1 Through Thickness Variations

The results of the finite element analysis are considered in conjunction with the microstructural analysis.

Using the tabulated data from Table 4-1 through to Table 4-4, assuming an original grain size of 35μm and fitting these into Equation 4-1 the time to 50% recrystallization ($t_{0.5}$) can be determined which represents the combined effect of all the process variables on the mill strip properties. The distribution of the $t_{0.5}$ value through thickness is presented for the middle section. The detail of this calculation is given in Appendix B.

Table 5-1: Time(s) to 50% recrystallization for the middle section using Equation 4-1.

Pass Number	M1	M2	M3	M4	M5	M6	M7	M8	M9
1	24	25	25	26	27	28	30	32	29
2	9	9	9	9	9	9	10	10	6
3	4	4	4	4	4	4	4	4	2
4	5	5	5	5	5	5	5	5	3
5	60	60	61	61	60	59	60	59	48

Note: M1 = mid plane and M9 = surface

From Table 5-1, there is little variation and no discernable trends in the values of $t_{0.5}$ through thickness. The change in $t_{0.5}$ is validated by the hardness measurements which differ from the mid plane to the surface in the order of 5% (see Figure 4-8). The montage of the microstructures also shows very little change in the recrystallization through thickness. The grain boundaries are not clearly delineated in the centre but this could be a relic from segregation during the casting of the billet. The effects of this segregation could have been carried through to the end microstructure during the rolling process.

5.1.2 Middle, Head and Tail Section Property Variations

The hardest section of the strip is the tail section followed by the head section and the softest is the middle section as can be seen in Table 4-5. The tail section is only marginally harder than the head section. The hardness difference is quite large between the end sections and the middle section, and is greater than 30%. The microstructure differs in a marked fashion between the ends and the middle section. Deformed elongated grains are seen in the ends whereas an equiaxed grain structure is seen in the middle section. The end section samples also have no annealing twins, which are seen in the middle section. By comparison the only axial compression samples (laboratory simulations) that did not show annealing twins with the oxalic acid etchant was the double hit samples deformed at 900°C and 850°C (see Figure 4-22). All the compression samples deformed at higher temperatures demonstrated annealing twins. The middle section was nearly fully recrystallized according to the EBSD analysis whereas the end sections showed a high level of deformation as can be seen in the hardness measurements and the microstructure.

The relative difference between the edge of the strip and the centre is greater in the middle section than in the end sections. By considering how the strip is coiled; it can be seen that the edge of the middle section would be the only area directly exposed to the air. It would be colder and therefore harder than the rest of the material. The end sections are not coiled in the hot coiler on every other pass and the edge and the centre are exposed to the air so the transverse variations in hardness are not as pronounced.

5.2 Mill Log Analysis

The analysis of the mill logs is an important step in understanding the metallurgical evolution of AISI304 stainless steel. The results of section 4.3 will be discussed in this section.

5.2.1 Middle Section MFS trends

The MFS for mill log L1 is presented below. This data is a representative sample of the mill logs.

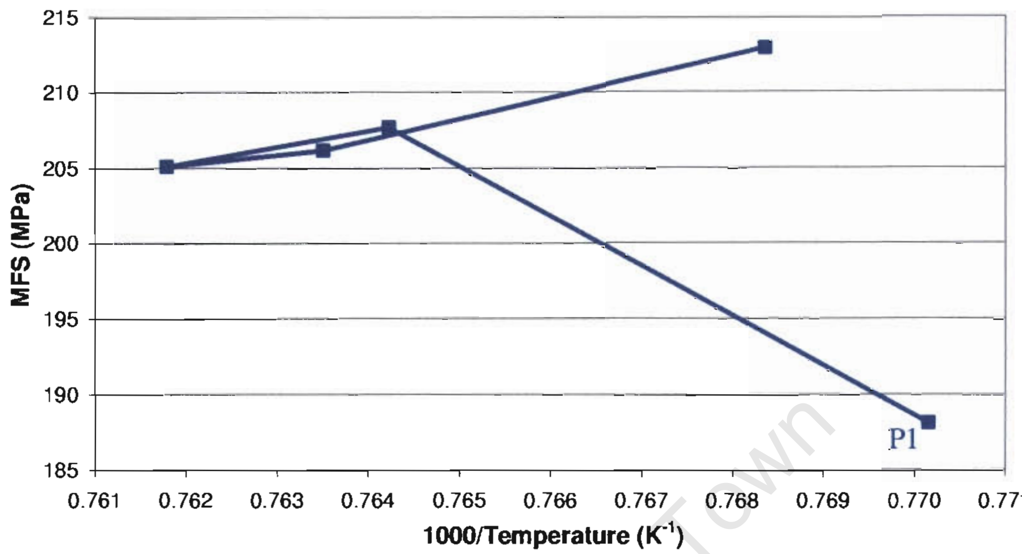

Figure 5-1: Pass schedule for L1 representing the middle section. Pass 1(P1) is indicated.

In all the MFS plots (Figure 4-10) there is a relatively large increase in MFS from the first to the second pass. This increase is despite a temperature increase which would normally decrease the MFS as was shown previously (see section 4.4.1 where the decrease in temperature would cause an increase in flow stress). At 1000°C full restoration would occur in 30s and the interpass time is 43s (see section Figure 4-28). This indicates that full restoration would have occurred after pass 1 and no strain could accumulate. The only other parameter that could increase the MFS is the strain (see Figure 4-11). This parameter increases only marginally and subsequent decreases in the strain do not cause such large changes in the MFS. In both the seven and the five pass schedules the data is roughly in a straight line with the exclusion of the first pass. The first pass data would be distant from this line. This would indicate that the temperature measurement of P1 is inaccurate to some extent. It is the only pass where the strip was not heated and coiled up in the hot coil furnace before the optical pyrometer measures the surface temperature. The material was heated in the preheat furnace prior to rough rolling. The contact of the work rolls of the roughing mill with the surface may have cooled the surface to such an extent that the surface temperature is not representative of the bulk material. The FEM also shows a low temperature on the surface. Thus the recorded surface temperature for P1 is most likely much lower than the bulk and consequently the MFS-temperature relationship for P1 is erroneous. In passes 2, 3 and, 4 the MFS falls in a very narrow range of values and this seems to be a balance between the strain and the steady state stress as can be seen from Figure 4-11 with no strain accumulation.

5.2.2 End Section kinetics

The time to 50% recrystallization ($t_{0.5}$) is also calculated and presented in Table 5-2, for mill log L1. The deformation parameters required to calculate $t_{0.5}$ is also included. Equation 4-1 is the equation used to calculate these times. The temperature used for both the head and the tail is the minimum temperature experienced. Due to a lack of data the deformation temperature was assumed to be equal to the annealing temperature. The steps used to calculate $t_{0.5}$ and to calculate all the variables in Table 5-2 are given in Appendix B.

Table 5-2: Time(s) to 50% recrystallization for the head section.

Pass	Strain per pass	Interpass Time	Effective Strain	X_{srx}	$t_{0.5}$ (s)
1	0.40	80	0.40	0.18	274
2	0.43	6	0.76	0.43	7
3	0.39	103	0.83	1.00	6
4	0.35	6	0.35	0.02	253
5	0.27	-	-	-	37

The head section kinetics can be seen in Table 5-2 above. Full restoration is only seen on pass 3 as can be seen by the X_{srx} of 1.00 in that pass. Otherwise strain accumulation can be on all other passes. The pass 5 $t_{0.5}$ is quite short considering that the head end of the strip had no signs of recrystallization. The temperature used to calculate this value was the last temperature as measured by the pyrometer as the strip is exiting the roll gap. The strip thickness is very thin so significant cooling could occur that would increase the value of $t_{0.5}$.

Table 5-3: Time (s) to 50% recrystallization for the tail section.

Pass	Strain per pass	Interpass Time	Effective Strain	X_{srx}	$t_{0.5}$ (s)
1	0.40	6	0.40	0.02	274
2	0.43	91	0.83	1.00	2
3	0.39	6	0.39	0.27	13
4	0.35	121	0.63	1.00	3
5	0.27	-	-	-	65

Recrystallization occurs in both passes 2 and 4 as can be seen by the X_{srx} of 1.00 in those passes. The tail section $t_{0.5}$ is again relatively low at 65s but the explanation of why it is so low is the same as for the head section.

5.2.3 Comparison of Flow Stress and MFS

The flow stress at 0.3 strain for 1050°C is 228MPa as can be seen in Figure 4-13. The data values for the mill log in Figure 5-1 are between 1000°C and 1050°C and the highest value is below 215MPa. Except for the last pass the strain is greater than 0.3 strain in the mill schedule. Despite a higher temperature and lower strain the flow stress is greater than the calculated MFS. The mill log MFS values are lower than corresponding flow stress values from the compression tests. This could be due to inadequate compensation for the specimen tension in the strip. The specimen tension would reduce the working load and give a lower MFS value.

5.3 Time to 50% Recrystallization

The time to 50% recrystallization ($t_{0.5}$) is evaluated in this section and compared to equations from literature. The form of this equation is given by Equation 2-9 and their constants are given in Table 2-3. The first step is to determine which equations are usable. Equations can be excluded where the deformation temperature is equal to the annealing temperature since that is not always the case in the rolling schedules. Equations are excluded where not enough constants are given. The only equation is left is from Barraclough et al and is Equation 2-10[44]. To calculate the $t_{0.5}$ the same procedure is followed as detailed in the Appendix B, with an extra calculation for calculating the peak strain.

Table 5-4: Time(s) to 50% recrystallization for mill log L1 using Equation 2-10.

Pass Number	Tail Section	Middle Section	Head Section
1	0.409	0.106	0.409
2	0.040	0.009	0.040
3	0.024	0.003	0.024
4	0.022	0.002	0.022
5	0.029	0.002	0.029

The times indicate that recrystallization would have occurred in the whole strip. This is clearly not correct for tail and the head section, from the microstructural analysis of the mill strip the head and tail are deformed with very little sign of recrystallization.

CHAPTER 6: CONCLUSIONS

6.1 Mill Strip Analysis

The conclusions here are drawn from the discussion in section 5.1.

- The mill strip through thickness variation is relatively small in both the middle sections and the end sections. The mill strip deformation and microstructure evolution can be considered uniform through thickness.
- The property variation in the transverse direction is greater in the middle section than in the end section.
- The ends are significantly more deformed than the middle section of the strip. The middle section is fully recrystallized where as the ends show no signs of recrystallization

6.2 Mill Log analysis

The mill log analysis provides valuable insight into the metallurgical evolution of the mill strip during the rolling process. Due discretion is required when interpreting the mill log data. Very few mill logs were analysed (five to eight) and these mill logs can show scatter in the data. Therefore no detailed conclusions can be drawn from analysis of these mill logs alone. All conclusions will be supported with other information. Here the other information was gained from metallography of the mill strips and uniaxial compression tests. An example of the problem is the measured temperature of the strip in the first pass. The measured temperature was lower than the speculated bulk temperature and the slope from the first to the second pass could be erroneously construed to be due to strain accumulation. But due to the occurrence of recrystallization this is not possible. The conclusions for this section are drawn from section 5.2:

- Complete restoration occurs between every pass in the middle section. The recrystallized state of the middle section mill samples verifies that this is possible.
- The kinetics of the head section and the tail section are different in every pass.

6.3 Axisymmetric Uniaxial Compression

Hot axial compression testing provided a valuable understanding of the flow stress changes with the changes in strain, strain rate, temperature and with single or double hits. The conclusions drawn below are based on section 4.4.

- The temperature has a profound influence on the flow stress and the microstructure. The higher the temperature the finer the grain sizes but the lower the hardness.
- The strain rates experienced in hot rolling does not have a significant effect on the flow stress and no measurable effect on the hardness.
- At temperatures above 950°C the material restores fully at the interpass times typically experienced during hot rolling (approximately 60s).

6.4 Characterisation of Post Deformation Softening

Performing heat treatments on the samples deformed in uniaxial compression allows us to draw conclusions on the restoration of the samples - on how different parameters influence the restoration kinetics.

- An increase in strain has the same effect as increasing the temperature which accelerates the restoration.
- The changes in the strain rates associated with hot rolling have no measurable effect on restoration kinetics.

6.5 The Time to 50% Recrystallization Equation

The time to 50% recrystallization ($t_{0.5}$) equations from literature are inadequate in predicting the microstructural evolution in the mill strip based on data from the mill logs. Either the equations have data missing from them or they are inaccurate. The need is seen for a more accurate equation which can predict the microstructural evolution in the mill strip during the rolling process.

CHAPTER 7: RECOMMENDATIONS

7.1 Direct Annealing Practice for Full Softening

The t_{50} given are based on a particular mill log and is not valid for all mill logs. Different mill strips will need different times to fully soften based on their individual mill logs. The individual mill log should then be used and the steps in Appendix B followed to calculate the $t_{0.5}$. This value of $t_{0.5}$ could then be used to make a judgement on how long the annealing practice would take. The quality of the data that is used in the equation would influence the accuracy of the $t_{0.5}$ equation.

7.2 Simulations

In this section recommendations are made to future research to enable better simulation of the hot rolling practice. These recommendations are made for the MTL Cam Plastometer that was used in these studies.

- Uniaxial deformation studies could be done with a larger number of hits to match the number of passes in a hot rolling schedule. This would be five or seven. With a greater number of hits the initial length of the specimen has to increase and therefore the specimen becomes more unstable. The chance of the load being placed eccentrically on the specimen increases. A second issue that would arise is that the barrelling would increase. This would cause greater strain inhomogeneity in the specimen. To compensate for this, measurements should not be taken in the middle but rather in the strain shell, where the local strain is very close to the nominal strain[70]. This strain shell can either be found by doing a finite element model or by taking profiles of hardness across the specimen.

- The uniaxial compression testing could be done to higher strains. Since the reduction is fixed, the length of the specimen would have to be decreased for a higher strain. With the increased strain, as with increasing the number of hits, barrelling would occur and would have to be compensated for.

- The variables in the compression testing can be varied in a number of ways. The temperatures between 950°C and 1000°C are very critical. Doing double hit tests in that range at possibly 10°C intervals would be quite enlightening. The time between hits could also be shortened from 60 seconds to 30 seconds.

7.3 Mill Strip Temperature

The temperature profile of the strip is very complex during deformation. There is a need to more accurately gauge the temperature profile during the rolling operation. This information would then be valuable for use in a $t_{0.5}$ equation. A new $t_{0.5}$ equation could then be produced to account for temperature fluctuations. Here are a few suggestions to achieve more accurate temperature data.

- A finite differences approach could be used to assess the temperature profile.

- Laboratory simulation could be done by rolling the material with a thermocouple embedded in the rolling strip. This facility is available at the CANMET MTL lab in Ottawa, Canada.

CHAPTER 8: BIBLIOGRAPHY

[1] *Alloy digest sourcebook: stainless steels.* edited by J. R. Davis, Ohio: ASM International, 2000

[2] *The metallurgical evolution of stainless steels.* edited by F. B. Pickering, Ohio: American Society for Metals, 1979

[3] P. Marshall, *Austenitic stainless steels: microstructure and mechanical properties.* New York: Elsevier Applied Science Publishers, 1984

[4] S. Venugopal, Y. V. R. K. Prasad and S. L. Mannan, **Influence of strain rate and state-of-stress on the formation of ferrite in stainless steel type AISI 304 during hot working,** *Materials Letters,* Vol. 26(3), 1996, pp. 161-165

[5] M. F. McGuire, **Austenitic Stainless Steels,** *Encyclopedia of Materials: Science and Technology* Editors-in-chief, K. H. Jürgen Buschow [et al.]. Amsterdam: Elsevier, pp 406-411

[6] *Stainless steels.* scientific editors, P. Lacombe, B. Baroux, G. Beranger; English translation by James H. Davidson and John B. Lindquist, France: Éditions de Physique, 1993

[7] L. Gavard, F. Montheillet and J. Le Coze, **Recrystallization and grain growth in high purity austenitic stainless steels,** *Scripta Materialia,* Vol. 39(8), 1998, pp. 1095-1099.

[8] F. Gauzzi, R. Montanari, G. Principi, A. Perin and M. E. Tata, **Martensite formation during heat treatments of AISI 304 steel with biphasic structure,** *Materials Science and Engineering A,* Vols 273-275, 1999, pp 443-447

[9] S. Kramer, G. Kneppe and D. Rosenthal, **Technology and performance of modern Steckel mills** *Iron and Steel Engineer,* Vol. 74(7), 1997, pp 17-26

[10] G. J. McManus, **Can Steckel mill combine efficiency of strip mill with properties of a universal mill**? *Iron and Steel Engineer,* Vol. 72, 1995, pp. 55-56

[11] E. Scholtz, I. K. Craig, and P. C. Pistorius, **Modelling for Control of a Steckel Hot Rolling Mill.** *ISIJ International,* Vol. 40(10), 2000, pp.1003-1012

[12] J. Schriefer, **The revival of Steckel mills in rolling plate.** *New Steel,* Vol. 11, 1995, pp. 26-33

[13] B. M. Gonzalez, C. S. B. Castro, V. T. L. Buono, J. M. C. Vilela, M. S. Andrade, J. M. D. Moraes and M. J. Mantel, **The influence of copper addition on the formability of AISI 304 stainless steel,** *Materials Science and Engineering A,* Vol. 343 (1-2), 2003, pp. 51-56

[14] F. B. Pickering. **Relationship between microstructure and properties in stainless steels.** *Micon 78: Optimization of processing, properties and service performance through microstructural control* Philadelphia : A.S.T.M., 1979, pp. 263-295

[15] F. J. Humphreys and M. Hatherly, *Recrystallization and related annealing phenomena.* New York: Pergamon, 1995

[16] P. Cotterill and P. R. Mould, *Recrystallization and grain growth in metals.* London: Surrey University Press, 1976

[17] C. Zener and J. H. Hollomon, **Effect of Strain Rate on the Plastic Flow of Steel.** *Journal of Applied Physics.* Vol. 15, 1994, pp. 22-32

[18] N. D. Ryan and H. J. McQueen, **Work hardening, strength and ductility in the hot working of 304 austenitic stainless steel.** *High Temperature Technology* , Vol. 8(1), 1990, pp. 27-44

[19] A. Cingara and H. J. McQueen, **New formula for calculating flow curves from high temperature constitutive data for 300 austenitic steels**, *Journal of Materials Processing Technology*, Vol. 36(1), 1992, pp. 31-42

[20] N. D. Ryan and H. J. McQueen, **Bar mill torsional simulation of 304 stainless steel.** *Canadian Metallurgical Quarterly* vol. 30(2), 1991, pp. 113-24

[21] N. D. Ryan and H. J. McQueen, **Flow stress, dynamic restoration, strain hardening and ductility in hot working of 316 steel**, *Journal of Materials Processing Technology*, Vol. 21(2), 1990, pp. 177-199

[22] N. D. Ryan, H. J. McQueen and E. Evangelista, **Dynamic recovery and strain hardening in the hot deformation of type 317 stainless steel.** *Materials Science and Engineering*, Vol. 81, 1986, pp259-272

[23] S. H. Cho and Y. C. Yoo, **Hot rolling simulations of austenitic stainless steel.** *Journal of Materials Science,* Vol. 36(17), 2001, pp. 4267-4272

[24] C. A. Smal and W. E. Stumpf, **Modelling the hot rolling properties of locally produced AISI 304 Stainless Steel**, *Proceedings of the 2nd international conference of the African Materials Research Society*, 2003, pp. 171-172

[25] N. D. Ryan, HJ McQueen and J. J. Jonas, **The Deformation behaviour of types 304, 316, and 317 Austenitic Stainless steels during Hot torsion** *Canadian Metallurgical Quarterly*, Vol. 22(3), 1983, pp. 369-378,

[26] R. D. Doherty, D. A. Hughes, F. J. Humphreys, J. J. Jonas, D. Juul Jensen, M. E. Kassner, W. E. King, T. R. McNelley, H. J. McQueen and A. D. Rollett, **Current issues in recrystallization: a review**, *Materials Science and Engineering A*, Vol. 238(2), 1997, pp. 219-274

[27] T. Maki, **Recovery of Ferrite and Austenite.** 2001. In *Encyclopedia of materials: science and technology.* Editors-in-chief, K H Jürgen Buschow [et al.]. Amsterdam: Elsevier, pp 2375 - 2381

[28] F. J. Humphreys, **Recovery**. 2001. In *Encyclopedia of materials: science and technology.* Editors-in-chief, K. H. Jürgen Buschow [et al.]. Amsterdam: Elsevier, pp. 8061 – 8064

[29] H. J. McQueen, **Dynamic Recovery and Recrystallization**. 2001. In *Encyclopedia of materials: science and technology.* Editors-in-chief, K. H. Jürgen Buschow [et al.]. Amsterdam: Elsevier, pp. 2375 – 2381

[30] R. D. Doherty, **Primary Recrystallization**. 2001. In *Encyclopedia of materials: science and technology.* Editors-in-chief, K. H. Jürgen Buschow [et al.]. Amsterdam: Elsevier, pp. 7846 – 7850

[31]A. Belyakov, T. Sakai, H. Miura and R. Kaibyshev, **Grain refinement under multiple warm deformation in 304 type austenitic stainless steel.** ISIJ International, vol. 39(6), 1999, pp. 592-599

[32] N. D. Ryan, and H. J. McQueen, **Comparison of static softening in 304 and 301 stainless steels in constant and declining temperature tests.** *Materials Forum*, Vol. 14(4), 1990, pp. 283-95

[33] A. A. Vieira, D. B. Santos, and R. A. N. M. Barbosa, **Dynamic recrystallization in austenitic stainless steels.** Recrystallization. '90, International Conference on the Recrystallization of Metallic Materials, (1990), pp 295-300

[34] N. D. Ryan and H.J. McQueen, **Dynamic softening mechanisms in 304 austenitic stainless steel.** *Canadian Metallurgical Quarterly*, Vol. 29(2), 1990, pp. 147-162

[35] S. H. Cho, and Y. C. Yoo, **Static recrystallization kinetics of 304 stainless steels.** *Journal of Materials Science* Vol. 36(17), 2001, pp. 4273-4278

[36] T. M. Maccagno, J. J. Jonas and P. D. Hodgson, **Spreadsheet modeling of grain size evolution during rod rolling.** *ISIJ International,* Vol. 36(6), 1996, pp. 720-728

[37] P. D. Hodgson and R. K. Gibbs, **A mathematical model to predict the mechanical properties of hot rolled carbon-manganese and microalloyed steels.** *ISIJ International,* Vol. 32(12), 1992, pp. 1329-1338

[38] A. Laasraoui and J. J. Jonas, **Recrystallization of austenite after deformation at high temperatures and strain rates - analysis and modeling.** *Metallurgical Transactions A: Physical Metallurgy and Materials Science*, Vol. 22A(1), 1991, 151-60

[39] A. J. McLaren and C. M. Sellars, **Modeling distribution of microstructure during hot rolling of stainless steel.** *Materials Science and Technology* Vol. 8(12), 1992, pp. 1090-1094

[40] N. D. Ryan and H. J. McQueen, **Comparison of static softening in 300 series stainless steels under iso- and anisothermal conditions.** *Materials Science and Technology,* Vol. 7, 1991, pp. 818-826

[41] N. D Ryan, E. Evangelista and H. J. McQueen, **Static recrystallization associated with hot working of austenitic stainless steels.** Materials Science Forum (1993), pp. 113-115.

[42] D.J. Towle and T. Gladman, **Recrystallization of austenitic stainless steels after hot rolling.** *Metal Science* Vol. 13(3-4), 1979, pp. 246-256

[43] X. J. Zhang, P. D. Hodgson and P. F. Thomson, **The effect of through-thickness strain distribution on the static Recrystallisation of hot rolled austenitic stainless steel strip,** *Journal of Materials Processing Technology,* Vol. 60(1-4), 1996, pp. 615-619

[44] D. R. Barraclough, and C. M. Sellars, **Static recrystallization and restoration after hot deformation of Type 304 stainless steel.** *Metal Science*, Vol. 13(3-4), 1979, 257-67

[45] M. El Wahabi, J. M. Cabrera and J. M. Prado, **Hot working of two AISI 304 steels: a comparative study,** *Materials Science and Engineering A,* Vol. 343(1-2), 2003, pp. 116-125

[46] S. Mahajan, C. S. Pande, M. A. Imam and B. B. Rath, **Formation of annealing twins in f.c.c. crystals**, *Acta Materialia*, Vol. 45(6), 1997, pp 2633-2638

[47] R. J. Romero and L. E. Murr, **Torque-related lamellar carbide growth associated with annealing twins in 304 stainless steel,** Acta Metallurgica et Materialia, Vol. 43(2), 1995, pp. 461-469

[48] V. Randle, **Mechanism of twinning-induced grain boundary engineering in low stacking-fault energy materials**, Acta Materialia, Volume 47(15-16), 1999, pp. 4187-4196.

[49] C. M. Sellars, **Dynamic recrystallization.** *Metals Forum*, Vol. 4(1-2), 1981, pp. 75-80

[50] E. I. Poliak and J. J. Jonas, **A one-parameter approach to determining the critical conditions for the initiation of dynamic recrystallization**, *Acta Materialia*, Vol. 44(1), 1996, pp. 127-136

[51] T. Sakai, **Dynamic Recrystallisation microstructures under hot working conditions**. *Journal of Materials Processing Technology*, Vol. 53(1-2), 1995, pp 349-361

[52] T. Sakai, **Plastic Deformation: Role of Recovery and Recrystallization**. 2001. In *Encyclopedia of materials: science and technology*. Editors-in-chief, K. H. Jürgen Buschow [et al.]. Amsterdam: Elsevier, pp. 7079 – 7084

[53] J. Elfmark, **Plasticity limit of metals during hot plastic deformation.** *Czechoslovak Journal of Physics*, Vol. B 35(3), 1985, pp. 269-74

[54] S. Venugopal, S. L Mannan and Y. V. R. K Prasad **On the modeling of grain size during hot working of stainless steels type AISI 304 and 316.** *Journal of Materials Science Letters*, Vol. 16(2), 1997, pp 137-142

[55] R. Kopp, **Metal Forming: General and Economic Aspects**. 2001. In *Encyclopedia of materials: science and technology*. Editors-in-chief, K. H. Jürgen Buschow [et al.]. Amsterdam: Elsevier, pp. 5408 – 5417

[56] A. Belyakov, T. Sakai, H. Miura, R. Kaibyshev and K. Tsuzaki, **Continuous recrystallization in austenitic stainless steel after large strain deformation.** *Acta Materialia*, Vol. 50(6), 2002, pp. 1547-1557

[57] B. Ahlblom and R. Sandström, **Hot workability of stainless steels: influence of deformation parameters, microstructural components and restoration processes.** *International Metal Reviews* Vol. 27, 1982, pp. 1 – 27

[58] Matweb. AISI Type 304 Stainless Steel [Online] last accessed 29 October 2004 http://www.matweb.com/search/SpecificMaterial.asp?bassnum=Q304A

[59] S. I. Kim and Y. C. Yoo, **Dynamic recrystallization behavior of AISI 304 stainless steel**, *Materials Science and Engineering A*, Vol. 311(1-2), 2001, pp 108-113

[60] W. Roberts, H. Boden, and B. Ahlblom, **Dynamic recrystallization Kinetics.** Metal Science (1979), 13(3-4), 195-205

[61] S. Venugopal, Y. V. R. K. Prasad and S. L. Mannan, **Processing map for cold and hot working of stainless steel type AISI 304.** *Journal of Nuclear Materials*, Vol. 206(1), 1993, pp 77-81

[62] M. Sheen, MSc Thesis University of Cape Town, 2001

[63] A. Belyakov, H. Miura and T. Sakai, **Dynamic recrystallization under warm deformation of a 304 type austenitic stainless steel**, *Materials Science and Engineering A*, Vol. 255(1-2), 1998, pp. 139-147

[64] A. Belyakov, T. Sakai and H. Miura, **Microstructure and deformation behaviour of submicrocrystalline 304 stainless steel produced by severe plastic deformation.** *Materials Science and Engineering A*, Vols 319-321, 2001, pp. 867-871

[65] H. J. McQueen and N. D. Ryan, **Constitutive analysis in hot working.** *Materials Science and Engineering A,* Vol. 322(1-2), 2002, pp 43-63

[66] D.L Barager *The MTL CAM Plastometer Theory and Operation.* Metals Technology Laboratories Report MTL 89-25(TR)

[67] W. F. Hosford, *Metal forming--mechanics and metallurgy.* Englewood Cliffs, N.J : Prentice-Hall, 1983

[68] R. W. Evans and P. J. Scharning, **Axisymmetric compression test and hot working properties of alloys.** *Materials Science and Technology*, Vol. 17(8), 2001, pp. 995-1004

[69] *Axisymmetric Uniaxial Testing using ISO-T anvils on Gleeble Systems* Dynamic Systems Inc.(DSI) Gleeble Systems Application Note (APN001).

[70] R. W. Evans and P. J. Scharning, **Strain inhomogeneity in hot axisymmetric compression test.** *Materials Science and Technology*, Vol. 18(11), 2002, pp. 1389-1399

[71] N. D. Ryan and H. J. McQueen, **Mean pass flow stresses and interpass softening in multistage processing of carbon-, HLSA-, tool- and γ-stainless steels,** *Journal of Mechanical Working Technology*, Vol.12(3), 1986, pp 323-349

[72] J. P. Holman, *Experimental methods for engineers.* 7th edition. Boston: McGraw-Hill, 2001

[73] S. Yue; D. Q. Bai; J. J. Jonas, **The influence of static and dynamic recrystallization on mean flow stress and grain size in steel.** *Canadian Metallurgical Quarterly*, Vol. 33(2), 1994, pp. 145-54

[74] F. Siciliano and J.J. Jonas, **Mathematical Modeling of the Hot Strip Rolling of Microalloyed Nb, Multiply-Alloyed Cr-Mo, and Plain C-Mn Steels.** *Metallurgical and Materials Transactions A: Physical Metallurgy and Materials Science*, Vol. 31A(1), 2000, Vol. 511-530

[75] R.B. Sims, **The Calculation of Roll Force and Torque in Hot Rolling Mills.** *Proceedings: Institute of Mechanical Engineers*, Vol. 168, 1954, pp.191-200

[76] T. M. Maccagno, J. J. Jonas, S. Yue, B. J. McCrady, R. Slobodian and D. Deeks, **Determination of recrystallization stop temperature from rolling mill logs and comparison with laboratory simulation results.** *ISIJ International,* Vol. 34(11), 1994, pp. 917-922

[77] A. A. Popoff, **Simplified hot rolling load calculations incorporating material strain rates.** *International Journal of Mechanical Sciences*, Vol.18(11-12), 1976, pp. 529-532

[78] W. Stumpf, **Grain Size modeling of a low carbon strip steel during hot rolling in a Compact Strip Production (CSP) plant using the hot charge route.** *Journal of the South African Institute of mining and metallurgy,* Vol. 103(10), (2003), 617 - 631

[79] U.S. Dixit and P. M. Dixit, **A finite element analysis of flat rolling and application of fuzzy set theory.** *International Journal of Machine Tools and Manufacture*, Vol. 36(8), 1996, pp. 947-969

[80] E. C. Larke, *The Rolling of strip, sheet and plate.* 2nd ed. London: Chapman and Hall, 1963

[81] C. M. Sellars and J. A. Whiteman, **Recrystallization and grain growth in hot rolling.** *Metal Science* , Vol. 13(3-4), (1979) pp. 187-94

[82] F.Siciliano Jr, K. Minami, T. M. Maccagno, J.J. Jonas, **Mathematical modeling of the mean flow stress, fractional softening and grain size during the hot strip rolling of C-Mn steels.** *ISIJ International*, Vol. 36(12), 1996, pp. 1500-1506

[83] G. Floweday Internal Report UCT 2003

[84] F. C. Bell and D. E. Sonon, **Improved metallographic etching techniques for stainless steel and for stainless steel to carbon steel weldments.** *Metallography*, Vol. 9(2), 1976, pp. 91-107

[85] G. F. Vander Voort, *Metallography, principles and practice.* New York: McGraw-Hill, 1984 pp. 447 - 451

[86] D. Tabor, *The hardness of metals.* New York : Oxford University Press, 2000

[87] L.E. Samuels **Microindentation in Metals** in *Microindentation techniques in materials science and engineering.* Philadelphia: International Metallographic Society, 1986, pp.5 – 25

[88] V. Randle and O. Engler, *Introduction to texture analysis : macrotexture, microtexture and orientation mapping.* Amsterdam: Gordon & Breach, 1999

[89] F. J. Humphreys, **Grain and subgrain characterization by electron backscatter diffraction.** *Journal of Materials Science*, Vol. 36(16), 2001, pp. 3833-3854

APPENDIX A

Table A-1: Five pass mill logs on the 1/4/2003

SLABID	PASSNO	ENTRYGAUGECOLD	EXITGAUGEMAINCOLD	ENTRYWIDTHCOLD	ROLLFORCEMAX	ROLLFORCEMIDDLE	ROLLTORQUEMAX	ROLLTORQUEMIDDLE	ENTRYTEMPMIN	ENTRYTEMPMIDDLE	EXITTEMPMIN	EXITTEMPMIDDLE	THREADINSPEED	THREADOUTSPEED	ROLLSPEED	ROLLTIME
		mm	mm	mm	kN	kN	kNm	kNm	°C	°C	°C	°C	m/s	m/s	m/s	s
3379701	1	25.46	18.36	1303	20755	19326	1047	977	1009	1043	995	1042	2.1	2.0	4.50	25.34
	2	18.36	12.94	1331	25344	21934	1091	951	996	1046	993	1048	2.1	2.0	4.00	31.27
	3	12.94	9.40	1330	24279	19313	832	671	955	1048	933	1049	2.1	2.0	5.40	33.87
	4	9.40	6.84	1328	27123	18519	763	538	916	1047	910	1048	2.1	2.0	6.80	37.79
	5	6.84	5.00	1326	29700	18577	682	449	886	1041	885	1046	2.1	2.0	10.00	47.57
3379683	1	26.06	18.97	1302	22587	20694	1137	1045	974	1018	962	1022	2.1	2.0	5.07	34.97
	2	18.97	13.37	1330	27859	23248	1215	1023	964	1029	965	1033	2.1	2.0	4.37	45.05
	3	13.37	9.71	1330	25357	20171	882	712	942	1035	923	1037	2.1	2.0	5.37	51.28
	4	9.71	7.36	1328	25229	17365	683	485	907	1034	900	1033	2.1	2.0	6.37	57.72
	5	7.36	6.00	1327	21462	13939	432	294	889	1026	874	1022	2.1	2.0	7.50	66.55
3379682	1	25.99	18.91	1301	22673	20782	1139	1048	972	1016	960	1020	2.1	2.0	5.07	34.94
	2	18.91	13.33	1328	27924	23314	1214	1023	962	1027	964	1032	2.1	2.0	4.37	45.02
	3	13.33	9.67	1328	25352	20239	880	712	941	1033	922	1036	2.1	2.0	5.37	51.24
	4	9.67	7.35	1327	25116	17338	677	482	906	1032	899	1031	2.1	2.0	6.37	57.62
	5	7.35	6.00	1326	21321	13897	427	292	888	1024	874	1020	2.1	2.0	7.50	66.35
3379721	1	26.02	18.94	1301	22238	20474	1118	1032	978	1021	966	1025	2.1	2.0	5.07	33.57
	2	18.94	13.35	1329	27478	22972	1197	1009	968	1032	969	1037	2.1	2.0	4.37	42.91
	3	13.35	9.69	1328	25204	19970	875	704	943	1038	924	1040	2.1	2.0	5.37	48.87
	4	9.69	7.36	1327	25048	17182	676	479	908	1036	901	1035	2.1	2.0	6.37	54.99
	5	7.36	6.00	1326	21599	13790	433	290	882	1028	875	1023	2.1	2.0	7.50	63.63
3379723	1	25.93	18.84	1302	22251	20455	1120	1033	979	1023	967	1027	2.1	2.0	5.07	33.69
	2	18.84	13.28	1329	27407	22849	1192	1002	969	1034	970	1038	2.1	2.0	4.37	43.12
	3	13.28	9.64	1329	25181	19896	873	700	943	1039	924	1041	2.1	2.0	5.37	49.11
	4	9.64	7.34	1327	24851	16993	667	471	908	1037	901	1036	2.1	2.0	6.37	55.15
	5	7.34	6.00	1326	21439	13625	428	286	882	1030	874	1025	2.1	2.0	7.50	63.69

Table A-2: 7 pass mill logs on 01/04/2004

SLABID	PASSNO	ENTRYGAUGECOLD	EXITGAUGEMAINCOLD	ENTRYWIDTHCOLD	ROLLFORCEMAX	ROLLFORCEMIDDLE	ROLLTORQUEMAX	ROLLTORQUEMIDDLE	ENTRYTEMPMIN	ENTRYTEMPMIDDLE	EXITTEMPMIN	EXITTEMPMIDDLE	THREADINSPEED	THREADOUTSPEED	ROLLSPEED	ROLLTIME
		mm	mm	mm	kN	kN	kNm	kNm	°C	°C	°C	°C	m/s	m/s	m/s	s
3379684	1	26.08	19.00	1301	22631	20673	1137	1042	972	1016	960	1020	2.1	2.0	4.80	35.58
	2	19.00	13.39	1329	27942	23467	1218	1032	962	1027	964	1033	2.1	2.0	5.00	40.80
	3	13.39	9.80	1329	24846	19971	856	697	942	1038	922	1044	2.1	2.0	8.00	39.26
	4	9.80	7.19	1328	27455	18708	781	549	907	1044	903	1050	2.1	2.0	10.00	43.61
	5	7.19	5.61	1325	24462	14963	524	338	891	1047	869	1047	2.1	2.0	10.00	53.05
	6	5.61	4.62	1320	24111	12425	389	219	842	1040	828	1035	2.1	2.0	10.00	62.53
	7	4.62	4.00	1317	22311	10272	266	140	813	1025	791	1016	2.1	2.0	10.00	80.16
3379690	1	26.19	19.10	1299	20235	18859	1021	954	1011	1044	997	1043	2.1	2.0	4.50	25.35
	2	19.10	13.46	1327	25221	21997	1109	973	999	1046	997	1049	2.1	2.0	4.00	31.09
	3	13.46	9.77	1327	24092	19201	844	682	958	1052	937	1053	2.1	2.0	5.40	33.68
	4	9.77	7.69	1325	21604	14888	556	395	921	1050	910	1046	2.1	2.0	6.80	35.99
	5	7.69	6.40	1322	19136	12084	376	249	891	1042	874	1036	2.1	2.0	8.20	37.64
	6	6.40	5.55	1320	18167	10229	278	169	850	1030	831	1023	2.1	2.0	9.60	38.80
	7	5.55	5.00	1318	16454	8514	195	112	825	1017	808	1009	2.1	2.0	10.00	50.34
3379695	1	26.22	19.14	1301	21024	19535	1060	987	998	1035	984	1037	2.1	2.0	4.50	28.99
	2	19.14	13.49	1329	26168	22311	1149	987	986	1042	985	1045	2.1	2.0	4.00	36.50
	3	13.49	9.79	1328	24645	19545	862	694	951	1046	931	1048	2.1	2.0	5.40	39.23
	4	9.79	7.72	1327	21896	15069	561	399	917	1044	907	1041	2.1	2.0	6.80	41.62
	5	7.72	6.43	1325	19223	12285	377	253	888	1036	873	1031	2.1	2.0	8.20	43.27
	6	6.43	5.58	1322	18241	10413	280	172	847	1025	829	1019	2.1	2.0	9.60	44.39
	7	5.58	5.00	1321	16610	8940	202	120	831	1013	810	1005	2.1	2.0	10.00	56.47
3379705	1	25.95	18.86	1302	20408	18984	1031	961	1011	1043	997	1042	2.1	2.0	4.50	24.95
	2	18.86	13.29	1330	25268	21829	1104	960	998	1049	996	1051	2.1	2.0	4.00	30.57
	3	13.29	9.65	1329	24152	19247	840	679	958	1051	937	1052	2.1	2.0	5.40	33.15
	4	9.65	7.62	1327	21448	14822	544	388	920	1047	909	1044	2.1	2.0	6.80	35.37
	5	7.62	6.37	1325	18992	11994	368	244	890	1040	873	1035	2.1	2.0	8.20	36.93
	6	6.37	5.53	1322	17989	10158	272	166	849	1028	830	1021	2.1	2.0	9.60	38.02
	7	5.53	5.00	1321	15972	8437	187	109	824	1015	808	1007	2.1	2.0	10.00	49.42

Table A-3: 7pass mill logs on 01/04/2004 continued

SLABID	PASSNO	ENTRYGAUGECOLD	EXITGAUGEMAINCOLD	ENTRYWIDTHCOLD	ROLLFORCEMAX	ROLLFORCEMIDDLE	ROLLTORQUEMAX	ROLLTORQUEMIDDLE	ENTRYTEMPMIN	ENTRYTEMPMIDDLE	EXITTEMPMIN	EXITTEMPMIDDLE	THREADINSPEED	THREADOUTSPEED	ROLLSPEED	ROLLTIME
		mm	mm	mm	kN	kN	kNm	kNm	℃	℃	℃	℃	m/s	m/s	m/s	s
3379707	1	25.73	18.65	1303	23161	20986	1162	1057	967	1013	956	1017	2.1	2.0	4.50	37.06
	2	18.65	13.15	1330	28301	23466	1221	1021	957	1023	959	1027	2.1	2.0	4.00	48.64
	3	13.15	9.67	1330	24711	19983	836	686	939	1027	919	1029	2.1	2.0	5.40	51.20
	4	9.67	7.67	1329	22307	15584	559	403	903	1026	893	1024	2.1	2.0	6.80	53.52
	5	7.67	6.41	1327	19398	12839	376	260	888	1019	871	1015	2.1	2.0	8.20	55.10
	6	6.41	5.56	1326	18463	10975	282	180	851	1009	832	1003	2.1	2.0	9.60	56.11
	7	5.56	5.00	1324	16432	9200	196	120	828	997	807	990	2.1	2.0	10.00	69.00
3379731	1	26.04	18.95	1302	22435	20586	1129	1039	976	1019	964	1023	2.1	2.0	4.80	34.30
	2	18.95	13.35	1329	27688	23272	1207	1023	966	1030	967	1036	2.1	2.0	5.00	39.19
	3	13.35	9.77	1329	24774	19862	853	693	943	1040	923	1046	2.1	2.0	8.00	37.88
	4	9.77	7.17	1328	27408	18630	779	546	908	1045	904	1051	2.1	2.0	10.00	42.10
	5	7.17	5.60	1325	24432	14844	522	334	882	1049	869	1049	2.1	2.0	10.00	51.08
	6	5.60	4.61	1321	24027	12346	386	218	845	1041	829	1036	2.1	2.0	10.00	60.06
	7	4.61	4.00	1317	22802	10193	270	139	809	1026	791	1017	2.1	2.0	10.00	77.23
3379793	1	26.11	19.03	1302	22232	20401	1118	1029	978	1021	966	1024	2.1	2.0	4.80	34.19
	2	19.03	13.41	1330	27538	23152	1202	1019	968	1032	969	1038	2.1	2.0	5.00	39.03
	3	13.41	9.82	1330	24718	19739	853	691	944	1042	924	1048	2.1	2.0	8.00	37.74
	4	9.82	7.20	1329	27322	18476	778	543	909	1048	905	1054	2.1	2.0	10.00	41.96
	5	7.20	5.62	1326	24436	14823	524	335	883	1050	870	1050	2.1	2.0	10.00	50.92
	6	5.62	4.62	1321	24031	12272	388	217	846	1043	829	1038	2.1	2.0	10.00	59.90
	7	4.62	4.00	1318	23346	10270	279	141	806	1028	792	1019	2.1	2.0	10.00	77.16
3379794	1	26.14	19.06	1303	22314	20489	1122	1034	977	1020	965	1023	2.1	2.0	4.80	34.19
	2	19.06	13.43	1331	27648	23268	1208	1025	967	1031	968	1037	2.1	2.0	5.00	39.02
	3	13.43	9.83	1331	24776	19833	855	694	943	1041	924	1047	2.1	2.0	8.00	37.74
	4	9.83	7.21	1330	27370	18560	780	546	909	1047	904	1053	2.1	2.0	10.00	41.95
	5	7.21	5.62	1327	24590	14962	530	340	883	1050	870	1049	2.1	2.0	10.00	50.96
	6	5.62	4.62	1322	24182	12388	392	220	846	1042	829	1037	2.1	2.0	10.00	60.02
	7	4.62	4.00	1319	23036	10213	273	140	807	1027	792	1018	2.1	2.0	10.00	77.25

Table A-4: Mill logs used for Finite Element Model, first two passes

Reference	Pass	Location	Time	Entry Temp	Exit Temp	Entry Gauge	Exit Gauge	Roll force	Rollforce Difference	Roll torque	Speed roll
		m	s	°C	°C	mm	mm	kN	kN	kNm	m/s
A1	1	1.84	0.7	715.5	940.2	23.4	16.7	22290.9	44.5	1199.7	2.170
A2	1	8.24	3.5	957.4	966.0	23.4	16.8	23022.2	-59.1	1096.6	2.202
A3	1	11.63	4.9	967.0	966.0	23.4	16.9	22547.1	-182.9	1043.2	2.185
A4	1	19.30	7.4	964.0	959.5	23.5	17.0	22517.0	-131.9	1099.4	3.901
A5	1	27.24	9.3	964.0	964.4	23.6	17.2	22532.9	-128.0	1028.5	4.006
A6	1	36.65	11.5	959.6	962.0	23.7	17.2	23405.5	-25.0	1101.6	3.987
A7	1	44.11	13.3	960.0	965.0	23.6	17.1	23076.2	-58.7	963.9	3.451
A8	1	53.24	16.0	957.0	960.0	23.6	17.2	23319.6	17.4	1076.8	3.084
A9	1	61.92	18.7	954.0	949.0	23.7	17.2	23772.1	57.0	1086.9	3.089
A10	1	70.43	21.3	945.0	944.0	23.8	17.3	24182.6	32.9	1103.7	3.086
A11	1	78.95	23.7	944.0	947.0	23.7	17.2	23745.4	-13.6	1089.6	3.096
A12	1	87.50	26.3	935.0	941.9	23.6	17.2	24301.8	-19.3	1089.8	3.091
A13	1	96.06	29.5	925.7	960.0	23.6	17.2	25473.5	1.8	1140.3	1.576
A14	1	97.38	30.5	924.0	960.0	23.4	17.1	17161.9	-29.3	1118.3	1.149
A14	2	4.04	1.7	926.7	830.2	17.2	12.7	27984.2	8.0	1239.8	2.196
A13	2	4.04	1.7	926.7	830.2	17.2	12.7	27984.2	8.0	1239.8	2.196
A12	2	12.90	5.5	939.7	917.9	17.2	12.5	25700.6	-216.6	1225.3	2.223
A11	2	23.85	8.4	947.3	938.3	17.2	12.5	25434.7	-193.2	1081.5	3.999
A10	2	36.65	11.5	958.0	949.0	17.2	12.5	25052.3	-203.8	1035.1	3.998
A9	2	47.74	14.1	961.0	952.0	17.1	12.5	24765.3	-200.1	951.7	4.010
A8	2	59.68	16.8	967.0	958.0	17.1	12.5	24158.4	-241.4	987.7	3.996
A7	2	70.77	19.5	971.0	961.0	17.2	12.6	24119.5	-194.8	990.8	3.991
A6	2	84.42	22.7	974.0	964.0	17.2	12.5	23463.1	-207.0	971.3	3.998
A5	2	95.51	25.3	977.0	964.0	17.2	12.6	23219.1	-209.4	970.2	3.992
A4	2	106.60	27.8	977.0	964.0	16.9	12.6	22599.5	-244.9	900.8	3.997
A3	2	117.57	30.8	977.0	963.6	17.0	12.5	21970.2	-271.6	669.3	2.522
A2	2	121.51	32.6	974.0	955.7	16.8	12.6	21631.1	-217.3	841.5	1.996
A1	2	133.69	38.7	954.0	948.0	17.0	12.6	22397.3	-185.3	783.7	1.000

Table A-5: Mill logs used for Finite Element Model, passes three to five.

Reference	Pass	Location	Time	Entry Temp	Exit Temp	Entry Gauge	Exit Gauge	Roll force	Rollforce Difference	Roll torque	Speed roll
		m	s	℃	℃	mm	mm	kN	kN	kNm	m/s
A1	3	3.93	1.7	934.2	923.0	12.6	9.5	25195.8	-169.3	922.9	2.194
A2	3	16.20	6.8	940.0	936.0	12.6	9.3	23551.4	-241.6	928.7	2.848
A3	3	21.37	8.1	947.3	949.1	12.5	9.3	23308.6	-285.3	906.7	4.209
A4	3	36.27	10.6	961.7	971.0	12.5	9.2	22416.1	-308.3	890.9	6.736
A5	3	52.31	12.8	967.0	977.0	12.6	9.3	22138.7	-258.2	751.4	6.994
A6	3	67.24	14.8	971.0	977.0	12.5	9.3	22138.7	-281.0	733.9	7.007
A7	3	83.65	17.0	971.0	977.0	12.5	9.2	22138.7	-239.8	753.8	7.004
A8	3	100.07	19.2	970.6	973.0	12.5	9.3	22315.3	-195.1	796.8	6.991
A9	3	114.99	21.2	965.0	970.0	12.5	9.3	22315.3	-183.9	789.5	6.993
A10	3	131.40	23.4	961.0	964.0	12.5	9.3	22513.9	-155.6	782.6	6.988
A11	3	148.75	25.9	955.0	957.0	12.5	9.3	22513.9	-123.9	718.7	5.548
A12	3	162.73	29.0	944.4	938.0	12.5	9.3	23021.6	-16.0	673.5	3.142
A13	3	179.48	36.5	901.0	889.1	12.9	9.4	26704.8	-338.6	912.4	1.999
A14	3	181.61	37.8	893.3	902.0	12.9	9.4	27230.5	-319.7	773.3	1.071
A14	4	3.80	1.8	878.1	776.5	9.4	7.4	25687.2	-219.9	724.7	2.196
A13	4	3.80	1.8	878.1	776.5	9.4	7.4	25687.2	-219.9	724.7	2.196
A12	4	20.83	8.0	910.2	891.1	9.3	7.2	22680.2	-314.4	713.0	4.382
A11	4	42.27	11.3	947.8	936.0	9.2	7.3	18656.3	-295.4	629.8	7.709
A10	4	61.62	13.4	961.0	951.0	9.2	7.3	17382.1	-211.9	617.4	9.785
A9	4	84.63	15.6	967.0	960.9	9.3	7.4	17150.3	-167.6	438.2	9.993
A8	4	101.47	17.2	970.0	963.9	9.2	7.3	16863.4	-153.6	435.1	10.000
A7	4	122.51	19.2	973.0	968.0	9.3	7.3	16863.4	-114.9	434.3	9.990
A6	4	145.66	21.4	976.0	971.0	9.3	7.3	16642.7	-135.1	434.3	10.008
A5	4	162.40	23.0	976.0	971.0	9.2	7.4	16438.8	-129.1	337.8	9.271
A4	4	185.71	25.7	973.0	966.4	9.2	7.4	16410.9	-158.2	311.7	7.108
A3	4	201.01	28.1	962.0	951.6	9.2	7.4	16587.5	-106.9	312.5	5.234
A2	4	209.59	30.0	943.7	936.4	9.3	7.4	17004.5	25.0	369.4	3.750
A1	4	229.98	39.1	894.2	892.0	9.6	7.5	23065.8	-181.1	485.8	1.024
A1	5	3.24	1.3	847.4	815.4	7.4	6.2	22365.7	-474.4	537.4	2.189
A2	5	23.72	8.0	883.2	903.3	7.4	6.1	19634.7	-367.2	558.7	4.979
A3	5	31.83	9.6	881.0	917.4	7.5	6.1	17428.8	-379.9	398.6	5.001
A4	5	51.63	13.4	887.7	939.7	7.3	6.1	14171.1	-218.6	318.9	4.999
A5	5	75.59	18.0	937.7	951.0	7.3	6.1	13232.5	-85.9	316.5	5.000
A6	5	97.47	22.2	894.8	955.0	7.3	6.1	12768.9	-66.9	279.7	4.996
A7	5	121.68	26.6	914.0	958.0	7.3	6.2	12592.4	-15.0	384.3	6.054
A8	5	145.88	29.9	956.5	961.0	7.3	6.2	12640.2	32.7	283.1	7.489
A9	5	169.32	32.9	962.0	961.0	7.3	6.2	12780.0	64.4	271.6	7.502
A10	5	191.20	35.7	962.0	955.0	7.3	6.1	12978.6	120.1	286.9	7.498
A11	5	216.20	38.9	955.0	948.0	7.3	6.2	12978.6	108.4	269.5	7.499
A12	5	239.67	41.9	938.4	922.3	7.3	6.1	12978.6	69.4	98.6	6.999
A13	5	261.63	46.4	895.8	865.7	7.3	6.2	14718.7	194.9	175.4	2.458
A14	5	264.33	47.7	888.0	854.6	7.3	6.2	15723.4	203.1	276.6	1.999

Table A-6: 5 pass mill log schedule on 26/11/2002

SLABID	PASSNO	ENTRYGAUGEAVG	EXITGAUGEAVG	WIDTHAVG	ROLLFORCEMAX	ROLLFORCEAVG	ROLLFORCEMIN	ROLLSPEEDMIN	ENTRYTEMPMIN	ENTRYTEMPAVG	ENTRYTEMPMAX	EXITTEMPMIN	EXITTEMPAVG	THREADINSPEED	THREADOUTSPEED	ROLLSPEEDAVG	ROLLSPEEDMAX
		mm	mm	mm	kN	kN	kN	m/s	°C	°C	°C	°C	°C	m/s	m/s	m/s	m/s
3366310	1	25.48	18.43	1566	26497	24562	21588	1.12	988	1014	1039	981	1002	1.68	1.15	2.69	3.07
	2	18.40	13.09	1586	28674	25867	7328	0.86	979	1014	1030	969	1008	2.03	1.09	3.66	4.52
	3	13.04	9.71	1587	29431	24987	24225	1.99	963	1008	1022	956	1012	2.09	1.00	4.63	5.53
	4	9.67	7.68	1586	27007	18050	5706	0.70	940	1005	1021	910	994	2.01	1.00	5.46	6.52
	5	7.62	6.46	1538	22134	13393	13089	0.78	892	985	1008	814	977	1.19	2.00	4.86	6.52
3366504	1	25.42	18.45	1613	29114	25443	22117	0.97	962	992	1028	964	994	1.81	1.00	3.48	4.53
	2	18.42	13.03	1617	30644	26424	24062	2.00	956	1009	1033	951	1004	1.88	1.37	4.10	4.54
	3	12.98	9.70	1618	29743	25507	24313	1.99	948	1009	1031	945	1011	1.79	1.01	5.03	5.52
	4	9.64	7.38	1618	29866	20765	19965	1.04	926	1007	1028	901	1002	1.80	1.05	5.93	6.56
	5	7.31	6.05	1564	26719	15759	15164	0.80	889	994	1018	809	986	1.38	1.99	5.64	6.51

APPENDIX B

Step 3: Calculate grain size (D_I) after the first pass. Equation B-2 adapted from Equation 3-20 on page 51

Calculated with $D_0 = 35\mu m$

$$D_i = A'\varepsilon_i^{a^{-0.75}} D_{i-1}^{0.5} Z_i^{D^{-0.1}}$$

Equation B-2

Where: D_i = recrystallized grain size after i^{th} pass

Z_i^D = Dynamic Recovery, Z parameter in i^{th} pass (352 $kJ.mol^{-1}$ for AISI304 stainless steel)

ε_i^a = accumulated strain in the i^{th} pass (note in first pass = ε_i) (i^{th} pass of Table 4-1)

A' = constant (value is $71.4\,s^{0.1}\mu m^{0.5}$ for AISI304 stainless steel)

Table B-3: Grain size after each pass

Pass Number	M1	M2	M3	M4	M5	M6	M7	M8	M9
1	25	25	25	24	24	24	24	23	22
2	17	17	17	17	17	16	16	16	14
3	15	15	15	14	14	14	13	13	12
4	16	16	16	16	16	16	16	15	14
5	18	18	17	17	17	17	16	16	16

Step 4: Calculate the first pass time to 50% recrystallization ($t_I^{0.5}$). Equation B-3 adapted from Equation 4-1on page 90

$$t_i^{0.5} = 6\times10^{-16}\varepsilon_i^{a^{-2}} D_{i-1}^{2} Z_i^{-0.375} \exp\left[\frac{478000}{RT_i}\right]$$

Equation B-3

Where: $t_i^{0.5}$ = interpass temperature in the i^{th} pass (K)

T_i = interpass temperature in the i^{th} pass (K) (i^{th} pass Table 4-4)

Table B-4: Time to 50% recrystallization

Pass Number	M1	M2	M3	M4	M5	M6	M7	M8	M9
1	24	25	25	26	27	28	30	32	29
2	9	9	10	10	10	10	11	11	7
3	4	4	4	4	4	4	4	4	3
4	6	6	6	6	5	5	5	5	4
5	70	69	70	70	70	69	69	68	56

Step 5: Calculate the fraction recrystallized (X_i) for the first pass. Equation B-4 adapted from Equation 2-8 on page 18

$$X_i = 1 - \exp\left[(-\ln 2)\left(\frac{t_i}{t_i^{0.5}}\right)^k\right]$$

Equation B-4

Where: X_i = fraction recrystallized in i^{th} pass (Table 4-1)

t_i = interpass time in i^{th} pass (s) (Table 4-1)

k = Avrami Constant (1.1)

Table B-5: Fraction recrystallized

Pass Number	M1	M2	M3	M4	M5	M6	M7	M8	M9
1	0.73	0.72	0.71	0.70	0.69	0.67	0.64	0.62	0.65
2	0.97	0.97	0.97	0.97	0.96	0.96	0.95	0.95	0.99
3	1.00	1.00	1.00	1.00	1.00	1.00	1.00	1.00	1.00
4	1.00	1.00	1.00	1.00	1.00	1.00	1.00	1.00	1.00

Step 6: Calculate accumulated strain (ε_a) for second pass. Equation B-5 adapted from Equation 3-17 on page 49

$$\varepsilon_i^a = \varepsilon_i + (1 - X_{i-1})\varepsilon_{i-1}^a$$

Equation B-5

Where: ε_i = strain per pass for i^{th} pass (Table 4-2)

Table B-6: Effective strain

Pass Number	M1	M2	M3	M4	M5	M6	M7	M8	M9
1	0.32	0.32	0.32	0.32	0.32	0.32	0.32	0.33	0.33
2	0.39	0.40	0.40	0.40	0.41	0.42	0.43	0.44	0.43
3	0.31	0.31	0.31	0.32	0.32	0.32	0.32	0.32	0.31
4	0.23	0.23	0.23	0.23	0.23	0.24	0.24	0.24	0.24
5	0.17	0.17	0.17	0.17	0.17	0.18	0.18	0.18	0.18

Step 7: repeat step 3, 4 and 5 in order for second pass

Step 8: repeat step 6 and then 3, 4, 5 in order for third pass

Step 9: repeat step 8 for fourth pass

Step 10: repeat step 6, 3 and 4 in order for fifth pass

This routine could be adapted for a 7 pass by excluding step 10

Step 10: repeat step 8 for fifth pass

Step 11: repeat step 8 for sixth pass

Step 12: repeat step 6, 3 and 4 in order for fifth pass